UNIVERSITÄT PADERBORN
Die Universität der Informationsgesellschaft

FAKULTÄT FÜR
ELEKTROTECHNIK,
INFORMATIK UND
MATHEMATIK

DSP based CD and PMD Equalization Techniques in PDM-QPSK and PDM-16-QAM Receivers

Von der Fakultät für Elektrotechnik, Informatik und Mathematik
der Universität Paderborn

zur Erlangung des akademischen Grades

Doktor der Ingenieurwissenschaften (Dr.-Ing.)

genehmigte Dissertation

von

M.Sc. Muhammad Fawad Panhwar

Erster Gutachter:	Prof. Dr.-Ing. Reinhold Noé
Zweiter Gutachter:	Prof. Dr. Peter Schreier

Tag der mündlichen Prüfung: 10.05.2016

Paderborn 2016

Diss. EIM-E/322

UNIVERSITÄT PADERBORN
Die Universität der Informationsgesellschaft

FAKULTÄT FÜR
ELEKTROTECHNIK,
INFORMATIK UND
MATHEMATIK

Abstract of the Dissertation:

DSP based CD and PMD Equalization Techniques in PDM-QPSK and PDM-16-QAM Receivers

by Mr. Muhammad Fawad Panhwar

Digital coherent fiberoptic transmission employing polarization-division multiplexing (PDM) along with the quadrature amplitude modulation (QAM) techniques, QPSK (quadrature phase shift keying) and 16-QAM, enhances spectral efficiency of optical networks. In this respect, polarization diversity coherent receiver gives a representation of the optical field in the electrical domain. This facilitates efficient digital signal processing (DSP) based compensation of fiberoptic transmission impairments. The signal quality is significantly impaired in long-haul transmission fiber links at a high symbol rate because of chromatic dispersion (CD) and polarization mode dispersion (PMD). A two-stage equalization approach is needed for efficient compensation of these channel impairments in the digital domain. In the first stage, CD compensation and estimation is required for uncompensated links with large amount of CD. Furthermore, as second stage, multiple-input multiple-output (MIMO) equalization is required for PMD and residual CD compensation.

This Ph.D. work aims at extensive investigation, development and optimization of DSP based equalization techniques for the compensation of CD and PMD. Robust DSP tools have been proposed based on the simulation results and performance analysis of 112 Gb/s PDM-QPSK and 224 Gb/s PDM-16-QAM systems. In this perspective, this Ph.D. dissertation contributes the following work:

- Efficient DSP based CD equalization has been investigated and optimized.
- DSP based CD compensation methods have been extended to be adaptive as per the requirements of modern dynamic channel switching concept.
- Improved MIMO equalizers have been proposed and investigated for the compensation of PMD and residual CD.

UNIVERSITÄT PADERBORN
Die Universität der Informationsgesellschaft

FAKULTÄT FÜR
ELEKTROTECHNIK,
INFORMATIK UND
MATHEMATIK

Zusammenfassung der Dissertation:

DSP based CD and PMD Equalization Techniques in PDM-QPSK and PDM-16-QAM Receivers

des Herrn Muhammad Fawad Panhwar

Digitale kohärente faseroptische Transmission mit Polarisationsmultiplex (polarization division multiplex, PDM) im Zusammenspiel mit Quadraturmodulation (quadrature amplitude modulation, QAM), QPSK (quadrature phase shift keying, Quadratur-Phasenmodulation) und 16-QAM steigert die spektrale Effektivität von optischen Netzwerken. In dieser Hinsicht gibt ein kohärenter Empfänger mit Polarisationsdiversität eine Darstellung des optischen Feldes in den elektrischen Bereich. Das vereinfacht effektiv die auf digitaler Signalverarbeitung (digital signal processing, DSP) basierende Kompensation von faseroptischen Beeinträchtigungen. Die Signalqualität ist bei Langstrecken und hoher Symbolrate beachtlich verschlechtert aufgrund von chromatischer Dispersion (chromatic dispersion, CD) und Polarisationsdispersion (polarization mode dispersion, PMD). Ein zweistufiger Ansatz zum Ausgleich ist erforderlich für eine effektive Kompensation dieser Störungen durch den Übertragungskanal im digitalen Bereich. In der ersten Stufe erfolgt die Kompensation der CD und deren Abschätzung für unkompensierte Kanäle mit viel CD. Dann, in der zweiten Stufe, wird mit einem Filter mit mehreren Ein- und Ausgängen (multiple-input multiple-output, MIMO) die PMD und die restliche CD kompensiert.

Diese Dissertation zielt ab auf die umfangreiche Untersuchung, Entwicklung und Optimierung von DSP-basierten Techniken zur Kompensation von CD und PMD. Robuste DSP-Werkzeuge wurden vorgeschlagen, welche auf Simulationsegebnisse und Verhaltensanalysen bei 112 Gb/s PDM-QPSK und 224 Gb/s PDM-16-QAM basieren. In dieser Hinsicht trägt diese Dissertation die folgenden Arbeiten bei:

- Effiziente DSP-basierte CD-Entzerrung wurde untersucht und optimiert.
- DSP-basierte CD-Kompensationsverfahren wurden erweitert, um adaptiv zu sein gemäß den Anforderungen der modernen dynamischen Kanalumschaltung.
- Verbesserte MIMO-Entzerrer zur Kompensation von PMD und der verbleibenden CD wurden vorgeschlagen und erforscht.

Declaration

I hereby declare that I am the sole author of this doctoral dissertation. This work has not been presented to any other university for the award of an academic degree. I also declare that contributions by other authors which are used or have led to the ideas behind this dissertation are properly referenced in written form.

Muhammad Fawad Panhwar Paderborn, 10.05.2016

Acknowledgements

I am indeed grateful to Prof. Dr.-Ing. Reinhold Noé for providing me an opportunity to work at his Chair for Optical Communication and High-Frequency Engineering (ONT). I am extremely thankful for his supervision and guidance in my doctoral work. Also, I would like to thank all the other members and support staff of the chair for their help and support. I am also grateful to Prof. Dr. Peter Schreier for reviewing my doctoral dissertation.

Besides, I would like to thank Prof. Dr.-Ing. Ulrich Rückert from CITEC, Bielefeld University and his former scientific staff member Dipl.-Ing. Christian Wördehoff for their support and co-operation under the DFG project. I am also grateful to Prof. Dr.-Ing. Werner Rosenkranz (Christian-Albrechts-University of Kiel) and Dr.-Ing. Annika Dochhan (ADVA Optical Networking) for supervising my M.Sc. thesis and therefore providing me an initial motivation for carrying out a Ph.D. in optical communication.

In the end, I am thankful to my family and friends for their support. I would like to thank my parents Mr. and Mrs. Prof. M. M. Panhwar for their constant support and motivation. Also, many thanks to Mahwish, Ziad and Farshad for their support. Last but not the least, many thanks to my wife Sona for her support and understanding and to my beautiful little lucky charm Farisha.

Table of Contents

Chapter 1

Introduction

This chapter basically serves as a general introduction to this Ph.D. thesis. Section 1.1 elaborates the significance of the topic which is under consideration in this dissertation. The aims and objectives of this Ph.D. work are explained and enlisted in section 1.2. Besides, the section 1.3 provides an outline about the structure of this dissertation.

1.1 Significance of the Topic in Optical Communications

The concept of data transmission over optical fibers was proposed in the late 1960s [1]. However, this idea suffered from an early setback because of the high transmission losses in the optical fiber [2]. Therefore, the coherent receivers were introduced to improve the receiver sensitivity [3]. Later, the erbium-doped fiber amplifiers (EDFAs) also emerged as an alternative. So, the interest shifted to direct-detection systems that employed in-line amplifiers [4]. However, in the 1990s the demand for high data-rates over long distances increased. Because of the advantages over electrical transmission, optical fibers were preferred and largely deployed in the core networks. The 2000s therefore witnessed a revival of interest in the coherent optical communications [5-9]. In addition to the increased receiver sensitivity, the coherent receivers enable the recovery of full optical field in the electrical domain, as opposed to the direct-detection receivers. So, the fiber link impairments can be efficiently mitigated in the digital domain. Furthermore, the digital coherent transmission provides both, i.e. phase and polarization diversity. Meanwhile, full-field detection technique was also introduced as a low-cost alternative specially targeted for metropolitan area networks (MANs) [10]. But, the amount of interest and research on full-field detection has been very limited.

The demand for high data-rate is ever increasing with the invention of new means of communications. Just to have an idea, Figure 1.1 shows the trend of this ever increasing demand for high data-rates. The five year statistics obtained from the German Commercial Internet Exchange (CIX-DE), Frankfurt [11] show that every year the throughput requirements increase substantially. The throughput required at this communication node reached up to a recently measured peak of 3.43 Tb/s. Furthermore, according to Cisco the global mobile data traffic grew by 81 percent in 2013. The global mobile data traffic reached 1.5 Exabyte per month at the end of 2013 [12]. Thus, the long-haul fiberoptic backbone networks have to handle this massive increase in the global data traffic.

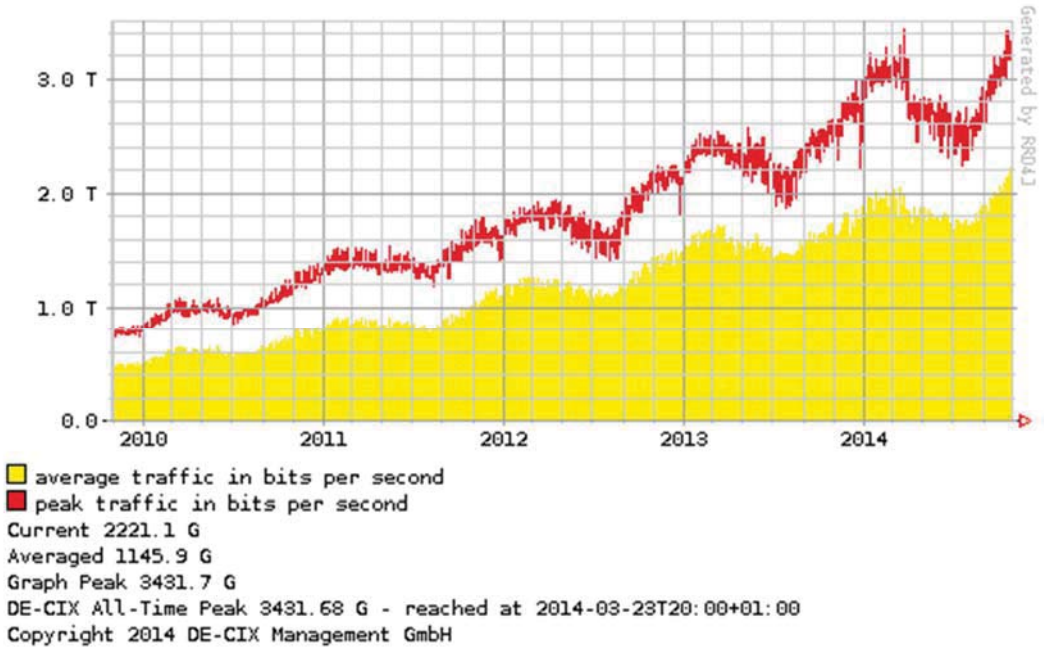

Figure 1.1: Five year data traffic statistics obtained at the CIX-DE, Frankfurt.

In addition to the ever increasing demand for high data-rates, the amount of deployed optical fiber is also becoming large. However, the high-rate transmission over long-haul fiber leads to a massive impairment and distortion of the received signals. In this perspective, various digital signal processing (DSP) based equalization algorithms for the compensation of optical fiber impairments have been investigated [5-9, 13-16]. Spectrally efficient modulation techniques, such as quadrature phase shift keying (QPSK) and higher-order quadrature amplitude modulation (QAM), have been

investigated in recent years to enable multiple bits per symbol transmission [13-19]. Because of the massively increasing demand of aggregate data-rates, numerous multiplexing techniques such as polarization-division multiplexing (PDM) [20], wavelength division multiplexing (WDM) [21], orthogonal frequency division multiplexing (OFDM) [22] and space division multiplexing (SDM) [23] have been proposed, investigated and developed for fiberoptic networks.

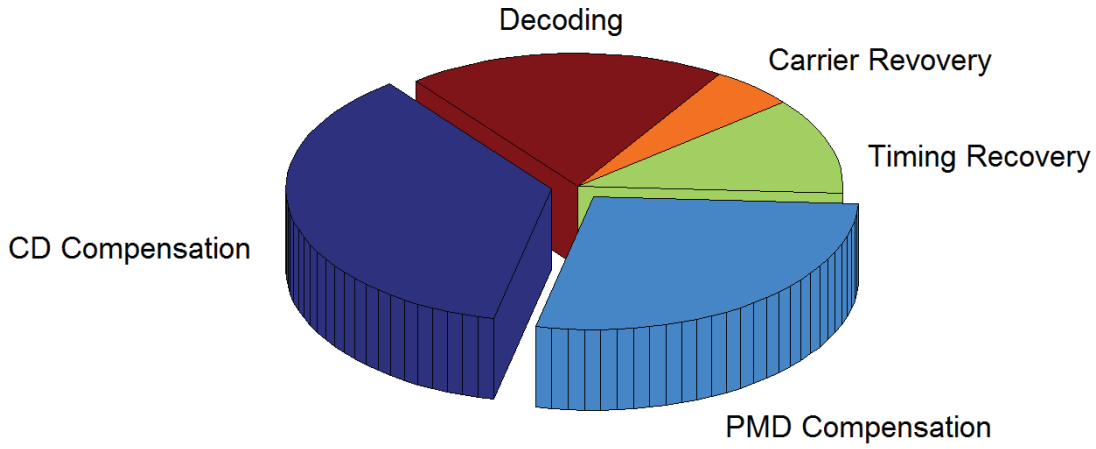

Figure 1.2: Percentage energy consumption of various subsystems within the DSP unit at the receiver.

Overall, the enormous demand for high data-rate over long-haul fiber requires development of high performance, low-complexity and efficient DSP based equalization algorithms. In this regard, chromatic dispersion (CD) and polarization mode dispersion (PMD) are the two major sources of distortion that worsen the quality of the received signal. Both of these linear fiber impairments, i.e. CD and PMD, increase with increasing data-rate or fiber length. Moreover, the equalization algorithms of these two fiber impairments greatly increase the overall DSP based receiver complexity. Henceforth, leading to huge resource and energy consumption in the field-programmable gate array (FPGA) based prototypes or application-specific integrated circuit (ASIC) implementations. Figure 1.2 shows the estimated percentage energy consumption of various subsystems within the DSP unit at the 100 G coherent receiver [24] employing PDM-QPSK scheme over 2400 km fiberoptic link. It can be seen that CD and PMD equalization subsystems consume bulk of the energy inside the

DSP unit i.e. 64 %. Whereas, the remaining DSP subsystems (timing recovery, carrier recovery and decoding) together consume only 36 % of the energy. So, although there existed DSP based techniques for CD and PMD compensation. However, this fact really provided immense motivation to further investigate, optimize and work on the theme of low-complexity and efficient DSP based CD and PMD equalization techniques under my doctoral work.

1.2 Objectives of the Ph.D. Work

This Ph.D. work aims at the investigation, development and optimization of efficient DSP based equalization techniques for the compensation of CD and PMD. In general, a two stage approach is needed to efficiently compensate these channel impairments in the DSPU. The main aims and objectives of this Ph.D. work are enlisted as follows:

- The first objective of this work is to investigate and design an efficient method for compensating CD in the DSP. In this perspective, a CD compensation technique with low computational effort and high robustness over large fiber links is desired.

- Secondly, the DSP based CD compensation methods are required to be extended as per the requirements of modern dynamic channel switching concept. Thus, efficient blind CD estimation is required with high search resolution at low computational complexity.

- Thirdly, the MIMO equalizers are to be investigated and optimized for the compensation of PMD and residual CD. In this respect, a MIMO equalization technique with fast convergence speed and low computational complexity is needed.

The validity and feasibility of the developed robust DSP tools has to be based on the simulation results and performance analysis of 112 Gb/s PDM-QPSK and 224 Gb/s PDM-16-QAM fiberoptic systems. Besides, the above objectives have to be treated by keeping in view the overall system optimization in terms of performance and computational complexity.

Furthermore, the investigated and developed DSP techniques for CD and PMD equalization under this work are part of the Deutsche Forschungsgemeinschaft (DFG) research projects NO 293/9-1, RU 447/13-1. The DFG project titled “Synchrone 16-QAM-Datenübertragung mit Polarisationsmultiplex und digitalem Empfänge zur Dispersionskompensation, Polarisationsregelung und vorwärtsgekoppelter Trägerrückgewinnung”, aims at developing efficient DSP tools for the synchronous 16-QAM receiver [25]. The project has been jointly investigated by the Optical Communication and High-Frequency Engineering group, University of Paderborn headed by Prof. Dr.-Ing. Reinhold Noé and Cognitronics and Sensor Systems group, Bielefeld University headed by Prof. Dr.-Ing. Ulrich Rückert.

1.3 Outline of the Ph.D. Thesis

This doctoral dissertation has been divided into six chapters. These chapters are followed by bibliography and appendix sections that are included at the end of this dissertation. After this first general introductory chapter, the second chapter gives a brief introduction to the fundamentals of digital coherent transmission systems. It also describes CD, PMD and the simulation setup details. The third chapter deals with the DSP based compensation of CD. Different aspects related to the digital CD compensation are considered and analyzed in this chapter. In the fourth chapter, the CD equalization work is extended to include adaptive blind CD compensation feature. Chapter five presents the work related to algorithms for digital MIMO equalization of PMD and residual CD.

Therefore, the second, third and fourth chapters of this dissertation represent the main investigations pertaining to the theme of this work. Finally, the sixth chapter summarizes this work and presents the future prospects.

Chapter 2

Fundamentals of Digital Coherent Transmission

This chapter gives a brief introduction to the fundamentals of digital coherent transmission systems. Digital coherent transmission technique is described in section 2.1. Section 2.2 mentions chromatic dispersion, which is a major source of inter-symbol interference (ISI) in optical communication. Polarization mode dispersion, the other main source of ISI, is described in section 2.3. Section 2.4 introduces to the simulation setup and its parameters considered throughout this dissertation.

2.1 Digital Coherent Transmission

The advent of the modern digital coherent systems has significantly simplified the compensation of linear fiber transmission impairments, such as CD and PMD. Digital coherent receivers greatly improve the receiver sensitivity as compared to the direct-detection receivers [5-9]. Furthermore, polarization-division multiplexing is possible in the coherent polarization-diversity receivers. In this perspective, linewidth-tolerant phase tracking schemes make it possible to use not only QPSK but also the higher-order modulation formats such as 16-QAM [26-31]. Thus, the digital coherent transmission significantly enhances the overall spectral efficiency of fiberoptic communication systems.

Figure 2.1 depicts a typical diagram of the digital coherent transmission system, along with the DSP based subsystems at the receiver. At the transmitter (TX), pseudo-random binary sequence (PRBS) pattern based signals drive the two I and Q modulators at a particular rate for the X and Y polarizations, respectively. These signals modulate the carrier signal fed by the transmitter laser. The laser signals are

split for X and Y polarization modulators using a polarization beam splitter (PBS). Then the modulated signals for the two polarizations are fed to the fiber channel using a polarization beam combiner (PBC).

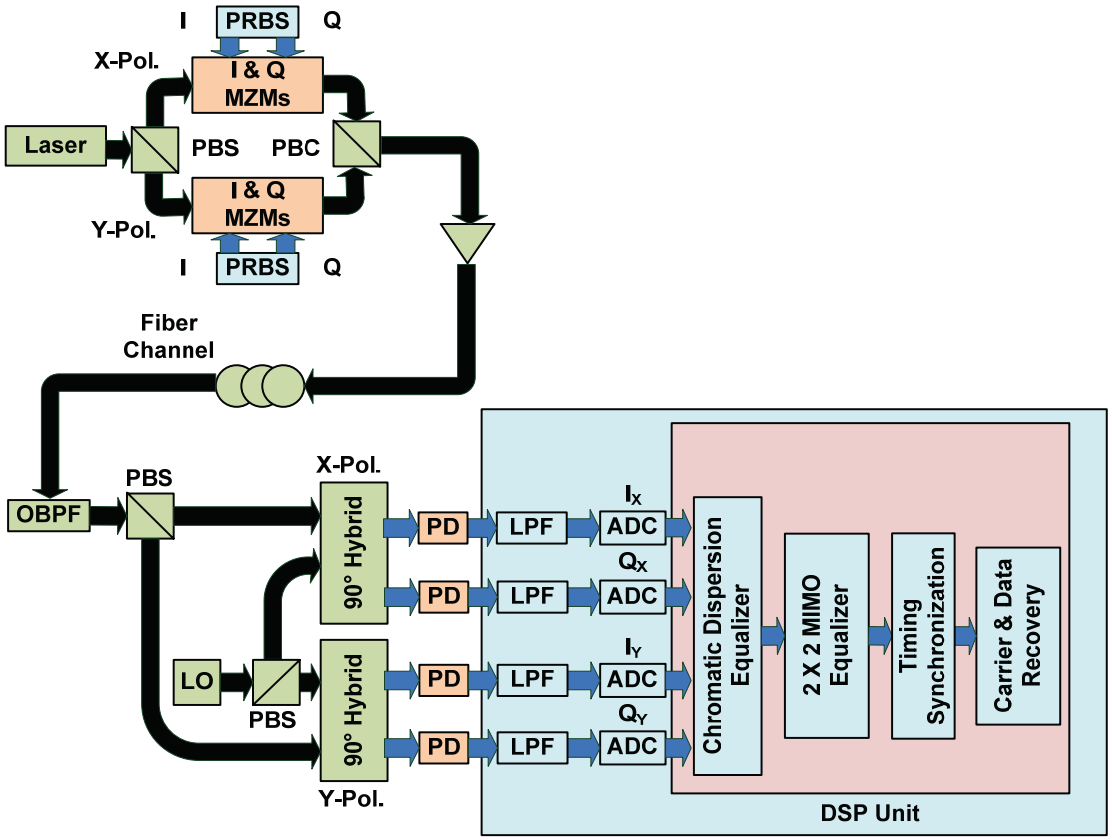

Figure 2.1: Digital coherent transmission system along with the receiver-side DSP unit.

An optical bandpass filter (OBPF) limits the optical bandwidth at the receiver (RX). The received signals are split using PBS into two optical 90 degree hybrid modules for the X and Y polarizations, respectively. The local oscillator (LO) signal is also fed to 90 degree hybrid modules. The received signals enter the DSP unit after photo-detection (PD), electrical low-pass filtering (LPF) and analog-to-digital conversion (ADC). The electrical LPF limits the electrical bandwidth. A two-stage equalization approach is adapted to equalize CD and PMD in the DSP unit (DSPU). The first stage consists of two CD equalizers for the X and Y polarizations separately. Furthermore, the second stage contains a MIMO equalizer for the mitigation of PMD and residual CD. The equalized signal is then synchronized and processed for carrier phase

estimation. Finally, the received data is recovered. This data could now possibly be used for bit error rate (BER) calculation in order to determine the performance of digital coherent receivers.

As depicted in Figure 2.1, a digital coherent transmission system requires additional optical components in comparison to the direct-detection scheme [4]. The optical 90 degree hybrid, local oscillator and extra photo-detectors increase the overall budget of the system. On the contrary, this additional budget enhances the possibility to efficiently mitigate channel distortions and use advanced modulation schemes such as 16-QAM [12-16]. Furthermore, it enables the realization of modern 100 Gb/s and beyond transmission systems.

2.2 Chromatic Dispersion

Chromatic dispersion is a source of signal distortion in fiberoptic transmission systems. It occurs due to the different group velocities of the wavelengths within the optical fiber [20, 32-36]. The material dispersion and waveguide dispersion result in the net dispersion of the optical fiber. The material dispersion is caused by the frequency dependence of the refractive index. The waveguide dispersion occurs due to the wavelength dependence of the signal power distribution between the core and cladding. The fiber chromatic dispersion causes pulse broadening, which results in ISI and therefore the 1st Nyquist criterion is not satisfied. It deteriorates the fiberoptic system performance, particularly over long fiber links at very high data rates. Chromatic dispersion in optical fibers can be positive (if the group delay increases with wavelength) or negative (if the group delay decreases with wavelength). This sign convention is with respect to the dispersion parameter D. A positive dispersion is termed as ‘anomalous dispersion’ and a negative dispersion is termed as ‘normal dispersion’. In most cases, anomalous dispersion occurs in optical fibers. Chromatic dispersion that occurs in dispersion compensating fibers is an example of normal dispersion.

The broadening effect of the transmitted pulses due to chromatic dispersion is shown in Figure 2.2. The pulses before transmission over the optical fiber are clearly distinguishable as shown in Figure 2.2 (left). However, after transmission over the

optical fiber the pulses are broadened in time domain due to chromatic dispersion as shown in Figure 2.2 (right). Consequently, there is an unwanted superimposition of pulses with the neighbouring pulses that results in ISI.

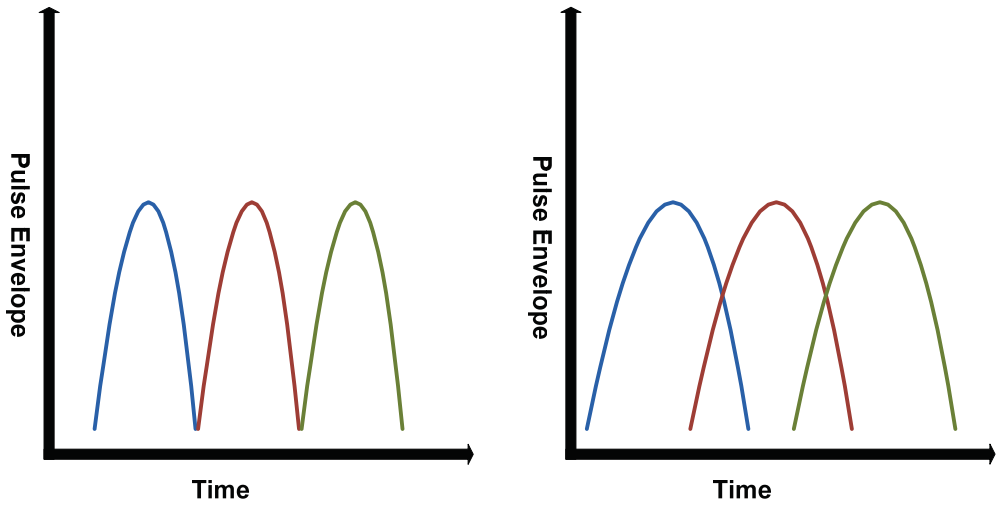

Figure 2.2: Pulse broadening effect caused by the chromatic dispersion in time domain.

The fiber chromatic dispersion effect could be represented and understood better in the frequency domain. Hence, the frequency domain transfer function $H(\omega)$ of the optical fiber can be represented as,

$$H(\omega) = e^{-(\alpha(\omega)+ j\beta(\omega))L} . \qquad (2.1)$$

In (2.1), $\alpha(\omega)$ represents the fiber loss (attenuation), $\beta(\omega)$ is the mode-propagation constant and L is the length of fiber. In order to model the chromatic dispersion effect in the transfer function, the fiber loss $\alpha(\omega)$ is assumed to be neglected. So, the simplified transfer function is given by,

$$H(\omega) = e^{-j\beta(\omega)L} , \qquad (2.2)$$

where $\beta(\omega)$ in (2.2) can be expanded using Taylor series around the center frequency ω_0 as,

$$\beta(\omega) = \beta_0 + \frac{\partial\beta}{\partial\omega}(\omega-\omega_0) + \frac{1}{2}\frac{\partial^2\beta}{\partial\omega^2}(\omega-\omega_0)^2 + \dots . \qquad (2.3)$$

In (2.3), β_0 in the first term corresponds to the phase delay per unit length, $\beta_1 = \frac{\partial \beta}{\partial \omega}$ in the second term represents the group delay per unit length and $\beta_2 = \frac{\partial^2 \beta}{\partial \omega^2}$ corresponds to the group velocity dispersion (GVD), which in fact is the main limiting impairment. Therefore, it is important to consider only the β_2 term in representing the fiber transfer function with chromatic dispersion.

The transfer function (2.2) can now be modified according to (2.3) as,

$$H(\omega) = e^{-j\frac{1}{2}\beta_2 L\omega^2} = e^{j\frac{DL\lambda^2}{4\pi c}\omega^2}. \tag{2.4}$$

In (2.4), λ is the carrier wavelength, c is the speed of light and the dispersion parameter D is defined as,

$$D = -\frac{2\pi c}{\lambda^2}\frac{\partial^2 \beta}{\partial \omega^2} = -\frac{2\pi c \beta_2}{\lambda^2}. \tag{2.5}$$

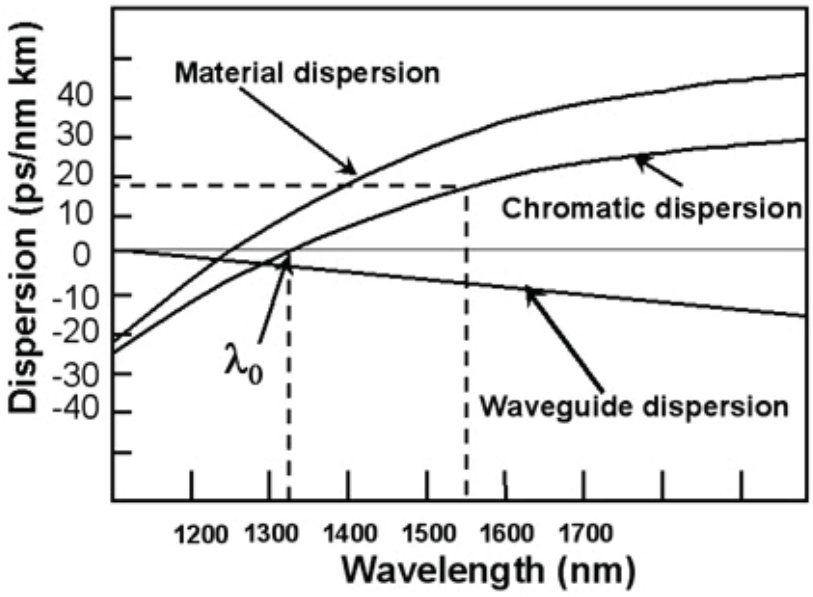

Figure 2.3: Wavelength dependence of the chromatic dispersion parameter in single-mode fibers [32].

The dependence of the chromatic dispersion parameter on wavelength in single-mode fibers is shown in Figure 2.3. The marked 1550 nm wavelength in Figure 2.3 is in fact

the common transmission wavelength in most optical transmission systems. The dispersion parameter is approximately 16 ps/nm/km at around transmission wavelength of 1550 nm. Besides, Figure 2.3 shows that the single-mode fibers have zero dispersion parameter at 1310 nm wavelength.

In digital coherent transmission systems, CD can be efficiently compensated by using digital equalizers [8-9]. These digital equalizers will be presented with details in chapters 3 and 4 of this dissertation.

2.3 Polarization Mode Dispersion

Polarization Mode Dispersion results from the optical birefringence in the fiber [20, 34-37]. Ideal optical fiber cores have a perfectly circular cross-section and the two orthogonal fundamental modes propagate at the same speed. However, the real fibers have imperfections and circular asymmetries that result in different propagation speeds (i.e. phase and group velocities) between the two orthogonal polarizations. Thus, polarization mode dispersion of a birefringent fiber relates to the difference in propagation time between the fast and slow axes over a fiber distance. 2π phase retardation occurs between the two orthogonal components over the fiber distance termed as 'beat length'. PMD degrades the fiberoptic system performance, particularly over long fiber links at very high data rates like CD.

The PMD in the optical fiber causes pulses to be received with a random delay as shown in Figure 2.4. As a consequence, the optical pulses statistically spread and overlap that results in ISI.

The instantaneous time difference ΔT between the fast (donated as X) and slow (denoted as Y) polarization axes is defined as,

$$\Delta T = \left|\beta_{1X} - \beta_{1Y}\right| = L\Delta\beta_1 . \tag{2.6}$$

Here, $\Delta\beta_1$ represents the difference between propagation constants β_{1X} and β_{1Y} of the two orthogonal axes. Both the axes have different refractive indices.

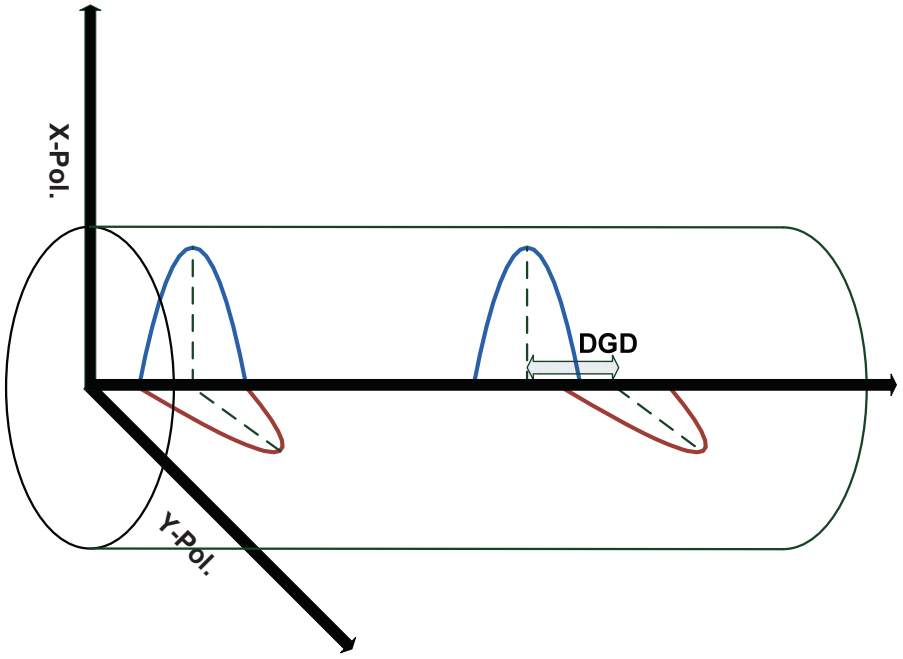

Figure 2.4: DGD effect caused by the polarization mode dispersion effect in time domain.

The axis with larger refractive index is referred to as a slow axis and the one with smaller refractive index as fast axis. However, PMD is a random birefringence phenomenon in the fiber so the delay must be described in terms of the statistical parameter [34]. In this respect, the mean square value $\left\langle (\Delta T)^2 \right\rangle = \sigma_T^2$ is given by,

$$\sigma_T^2 = 2\Delta\beta_1{}^2 l_c{}^2 \left[e^{-L/l_c} + \frac{L}{l_c} - 1 \right], \tag{2.7}$$

where l_c denotes the correlation length. It is defined as the fiber length over which the two orthogonal polarization components remain correlated. In general, a fiber link is modelled to be composed of many sections of this correlation length. For the assumption $L >> l_c$, which holds good for L>1 km, the root mean square (RMS) value of ΔT approximates to

$$\sigma_T \approx \Delta\beta_1 \sqrt{2 l_c L} \equiv D_p \sqrt{L}, \tag{2.8}$$

where D_P is the PMD parameter. The PMD parameter is measured in ps/√km. In practical systems, the typical value of PMD parameter lies in the range of 0.1 ps/√km to 1 ps/√km.

The PMD in optical fibers is often defined in terms of mean differential group delay (DGD) value. The mean DGD value increases with the square root of fiber length and follows a 'Maxwellian distribution'. In digital coherent transmission systems, PMD can be efficiently compensated by using digital MIMO equalizers [8-9]. These digital equalizers will be presented in detail in chapter 5 of this dissertation.

2.4 Simulation Setup

The investigated and developed DSP techniques under this work have been supported by simulation results, alongside the related text and mathematical models. This section introduces the simulation setup and its parameters that are considered throughout this dissertation. In this perspective, 112 Gb/s PDM-QPSK and 224 Gb/s PDM-16-QAM fiberoptic systems have been simulated and analyzed using widely considered optical fiber simulation software VPI TransmissionMaker™ to evaluate the performance of this research work [38]. It is used along with its co-simulation feature to develop user defined modules in MATLAB™ and Python™ [38-40]. At the transmitter, 2^{15}-1 PRBS pattern based signals drive the two I and Q modulators at a rate of 28 Gbaud. Then the generated optical data signals are polarization-multiplexed onto the standard single-mode fiber (SSMF) channel.

The CD coefficient of the fiber channel is 16 ps/nm/km. For modelling PMD in the fiber, many sections within the fiber length are used to emulate a Maxwellian distribution of DGD values [38]. Hence, a mean DGD value can be inserted in the fiber simulation module to generate statistically varying different instantaneous PMD scenarios. An optical Gaussian 2nd-order 36 GHz bandpass filter limits the optical bandwidth at the receiver and a 5th-order 19 GHz electrical LPF (Bessel filter) is used after photo-detection.

At the receiver, the data is sampled at a sampling rate of 56 GS/s with 5-bit and 7-bit ADCs for PDM-QPSK and PDM-16-QAM, respectively. The ADC resolutions are set

according to [29] for PDM-QPSK and PDM-16-QAM, respectively. The ADC sampling rate of twice the baud rate is employed in general. All the same, in some sections of this dissertation reduced oversampling rates have been used, these sampling rates will be specified accordingly.

Further processing of the sampled digital data takes place in the DSPU. The DSPU comprises of CD equalizer, MIMO equalizer for PMD and residual CD compensation, timing synchronizer, carrier and data recovery. The VPI TransmissionMaker™ incorporates a co-simulation feature that enables interfacing with MATLAB™ and Python™. Thus, there is flexibility of developing and investigating user defined DSP subsystems in VPI TransmissionMaker™. The co-simulation feature has been extensively utilized in this Ph.D. work to simulate and verify the developed DSP subsystems and their algorithms.

In this work, simulations have been carried out based on the Monte Carlo method [41-42]. So a large number of bits are simulated in order have a reliable estimate of the system characteristics. In this respect, the BER value is an important system performance parameter. The Monte Carlo method based simulations can be used to estimate BER as,

$$N_b = \frac{N_e}{\langle BER \rangle}, \tag{2.9}$$

where N_b is the number of bits used in the simulation, N_e refers to the number of bit errors in the recovered data and $\langle BER \rangle$ represents the expected BER for the simulation model. In fiberoptic systems, BER value of 10^{-3} is, in general, considered to be an acceptable value. Further reduction in the BER is possible by employing the available state-of-the-art forward error correction (FEC) techniques [43-45]. In order to obtain system BER value of 10^{-3} even 100 bit errors would give quite a reliable BER estimate. This corresponds to the simulation 10^5 bits. However, even more reliable BER value would be obtained if 1000 bit errors are to be considered. In this case, 10^6 bits are required to be simulated. In this work, the system BER value is estimated based on the simulation of at least 10^6 bits.

Chapter 3

DSP based Chromatic Dispersion Equalization

This chapter describes the work related to CD compensation in the digital domain. Section 3.1 introduces and explains the DSP based CD compensation. Overlap-save method based filtering is presented in section 3.2. Frequency domain based efficient CD equalization is described in section 3.3. Furthermore, the use of the proposed FDE at reduced sampling rates is described in section 3.4. Finally, section 3.5 discusses the work, presented in this chapter, in terms of complexity and performance.

3.1 Digital Chromatic Dispersion Equalization

Optical chromatic dispersion compensation based on fiber Bragg gratings (FBGs) [46] and dispersion compensating fibers (DCFs) [47] has been demonstrated previously. However, the bulky size and high cost makes these optical CD equalization techniques less attractive. Furthermore, optical CD compensation techniques lack the capability to adapt to dynamic channel switching. Alternatively, this fiber transmission impairment can be mitigated in electronic domain using digital coherent receivers. Thus, the digital chromatic dispersion compensation can be performed with finite impulse response (FIR) equalizers [48-49] in the time domain (TD) or else with frequency domain equalizers [50-59]. Besides, infinite impulse response (IIR) filters can also be employed to compensate CD in the DSPU [60]. However, these filters require feedback for the computation of output signals. Therefore, IIR filters are almost impossible to implement at high processing speed in the DSPU [61].

The information of the fiber channel impulse response is used to implement TD-FIR equalizer. Therefore, the discrete-time impulse response *h(k)* of the TD-FIR filter can be modelled by performing the inverse Fourier transform on the reciprocal of (2.4) as

$$h(k) = \sqrt{\frac{jcT_S^{\,2}}{DL\lambda^2}} e^{-j\frac{\pi cT_S^{\,2}}{DL\lambda^2}k^2}, \tag{3.1}$$

where, k denotes the discrete-time index $k \in \{0,1,...,N_{TDE}-1\}$, N_{TDE} represents the number of taps in the TD-FIR equalizer and T_S denotes the symbol duration. The TD-FIR equalizer output signals are given by the discrete time linear convolution of the impulse response (3.1) with the incoming signals,

$$e_{F,X}(k) = e_X(k) \otimes h(k) \tag{3.2}$$

and

$$e_{F,Y}(k) = e_Y(k) \otimes h(k) \tag{3.3}$$

for the X and Y polarization, respectively. Where, $\otimes$ is used to denote the convolution operation. The signals in both polarizations undergo the same type of distortion due to CD present in the fiber link. Therefore, it should be noted that the same equalizer impulse response is used for both polarizations. The required number of equalizer taps for the impulse response in (3.1) is given by

$$N_{TDE} = \left\lceil 0.032B^2 \right\rceil, \tag{3.4}$$

per 1000 ps/nm of chromatic dispersion for transmission in the 1550 nm window, at B Gbaud and two samples per symbol [49]. Consequently, 101 equalizer taps would be required to compensate 4000 ps/nm of fiber CD (i.e. 250 km) for a 28 Gbaud system.

Figure 3.1 shows the digital TD-FIR equalizer structure based on a delay tap scheme. In the DSPU, two such structures are required to compensate CD separately for the X and Y polarizations, respectively. The half symbol duration ($T_S/2$) delays characterize this structure as a fractionally spaced equalizer (FSE). Note that the FSEs with half symbol duration delays can more efficiently mitigate channel ISI compared to the symbol spaced equalizers [62-69].

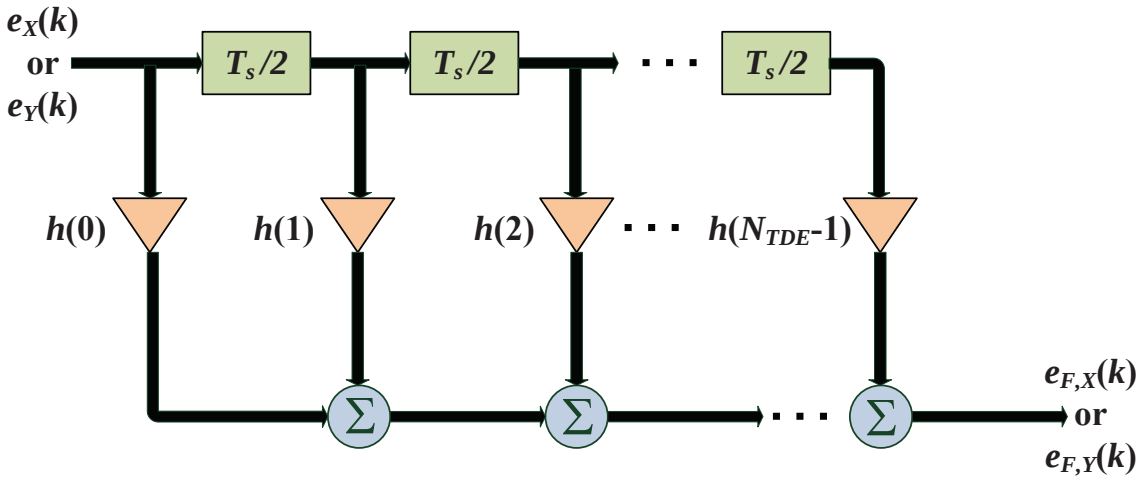

Figure 3.1: Digital TD-FIR equalizer structure based on a delay tap scheme for digital CD compensation.

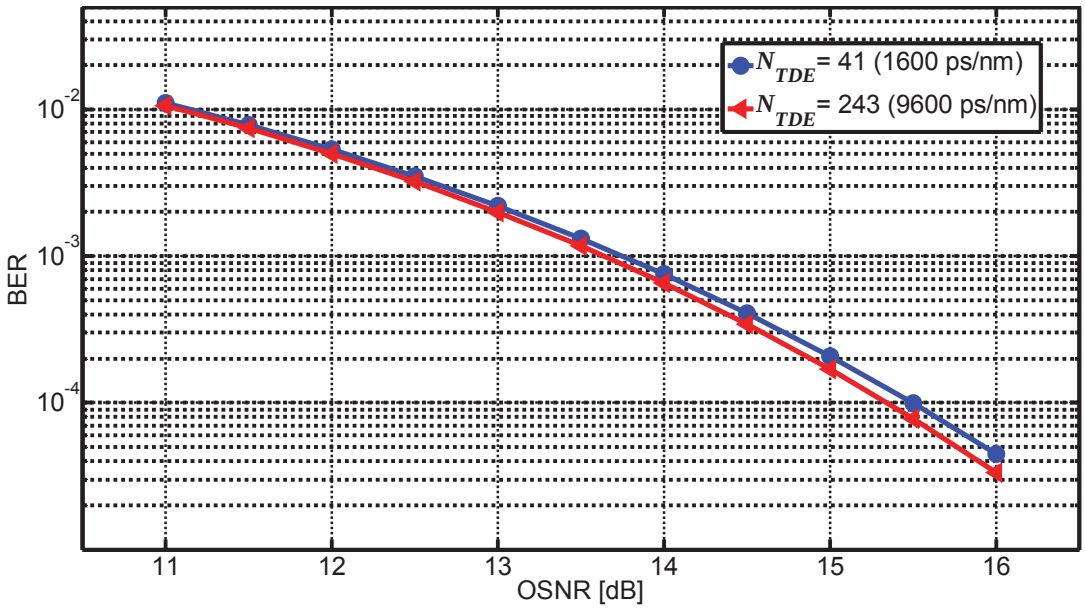

Figure 3.2: CD compensation using impulse response based digital TD-FIR equalizer.

Figure 3.2 shows the BER performance of the TD-FIR equalization as an example. In this respect, 41 and 243 taps are employed compensate the fiber CD of 1600 ps/nm and 9600 ps/nm, respectively. The simulated BER is shown against the required optical signal-to-noise ratio (OSNR). The curves for two different amounts of fiber CD closely match each other, without much penalty. Thus, any amount of fiber CD can be

compensated without performance degradation, if sufficient number of equalizer taps are employed (according to the relationship in (3.4)).

The TD-FIR equalizers do not require feedback signals for their implementation. However, the use of TD-FIR equalizers is not beneficial for large number of taps (or large fiber distances) because of their large complexity [52, 62-63]. This complexity mainly results from the computational effort required for discrete time linear convolution. Therefore, it would be difficult to implement TD-FIR with a large number of taps in the FPGA based prototypes or in ASICs due to huge power consumption and high gate density. Consequently, frequency domain equalization will now be focused in the following sections for digital CD compensation.

3.2 Overlap-Save based Frequency Domain Filtering

Frequency domain equalization (FDE) is found to be an efficient solution in terms of complexity for uncompensated links with large channel memory [53-59]. In this respect, the discrete Fourier transforms (DFTs) can be efficiently computed based on fast Fourier transforms (FFTs). In FDEs, the FFTs are executed using radix-2 or radix-4 algorithms. The frequency domain filtering of incoming digital signals can be achieved by using overlap-save or overlap-add methods [62-65].

The overlap-save and overlap-add methods provide efficient frequency domain filtering of long data sequences. Filtering based on these two methods is also often referred to as ‘fast convolution’ in literature. The overlap-save and overlap-add methods employ blockwise circular convolution to accomplish discrete linear convolution. In the overlap-save method, no extra additions are required at the output since the overlaps at the edges are simply discarded. However, the overlap-add method needs addition of the overlap parts at the output [63-65]. Therefore, the overlap-save method is computationally more efficient as compared to the overlap-add method. This section describes the overlap-save method, which is considered for frequency domain CD equalization in this work. The overlap-save scheme based frequency domain filtering is illustrated in Figure 3.3.

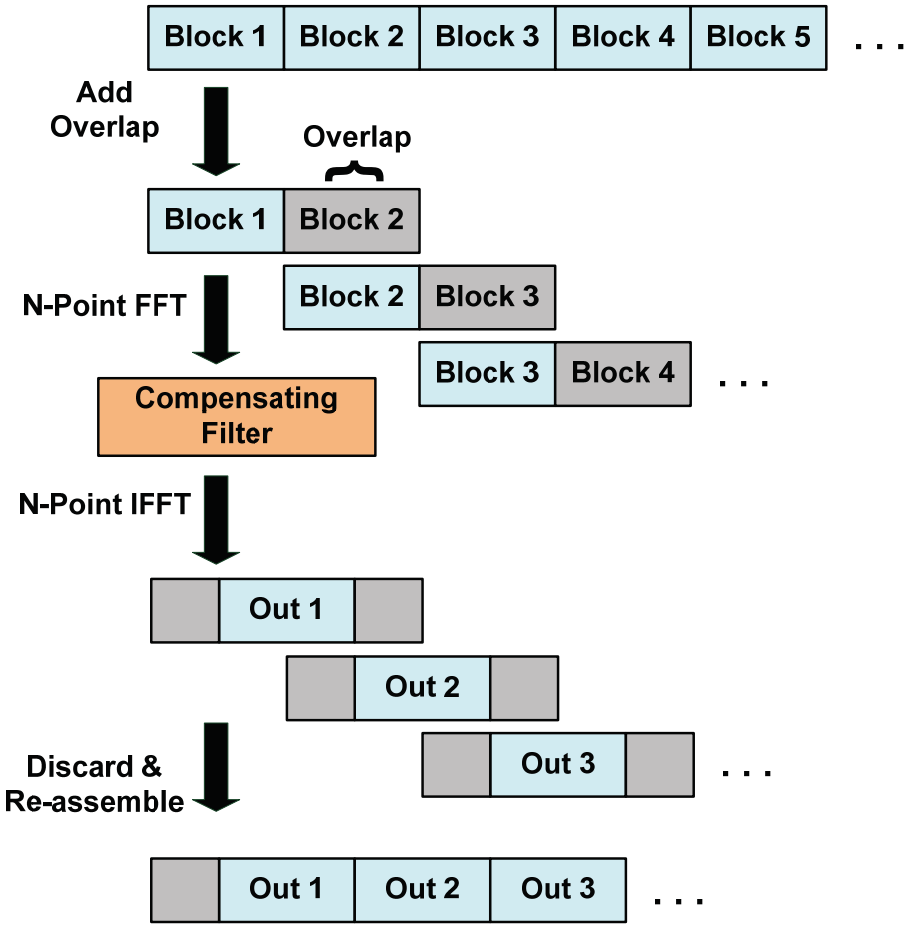

Figure 3.3: Overlap-save method for frequency domain filtering.

The overlap-save is an efficient technique to evaluate the discrete time linear convolution between a very long data sequence and a large FIR filter in the frequency domain e.g. CD equalization. In this method, the received discrete time signals are divided into several overlapping blocks. Each block is processed one by one and then reassembled.

At first, the overlap part is concatenated with each incoming block. The length of each block along with its overlap part is termed as FFT-size. The overlap part in fact comprises of data from the next block. In the next step, each block and its overlap part undergoes FFT operation. The frequency domain data is then multiplied with the compensating filter (i.e. the equalizer transfer function). Now, the filtered data is transformed back to the time domain by an inverse FFT (IFFT) operation. The overlap samples on the both sides of these time domain blocks are discarded. In the final step of overlap-save method, the equalized data blocks are reassembled at the output.

Usually, 50 % overlap is considered suitable for this method [70-71]. In the overlap-save method based FDE, the inter block interference (IBI) is removed because of the overlap parts at the block edges. So, the guard intervals (GIs) are not required [56]. Hence, overlap-save enables spectrally efficient transmission without GIs. This frequency domain filtering method will be discussed and applied for the compensation of CD in the next section.

3.3 Frequency Domain Chromatic Dispersion Equalization

Frequency domain equalization is a widely considered technique for the mitigation of CD. FDE equalizers have low computational complexity even for large fiber CD. The transfer function of the frequency domain CD equalizer can be written as the inverse of the fiber transfer function (2.4),

$$H'(\omega) = e^{j\frac{1}{2}\beta_2 L\omega^2} = e^{-j\frac{DL\lambda^2}{4\pi c}\omega^2} . \tag{3.5}$$

Now, (3.5) can be represented equivalently in the discrete-frequency domain transfer function for DSP based CD compensation as follows,

$$H'[n] = e^{-j\frac{\pi DL\lambda^2 {R_S}^2}{cN^2}n^2} . \tag{3.6}$$

In (3.6), n represents the discrete-frequency i.e. $n \in \{0,1,...,N-1\}$, R_S is the ADC sampling frequency and N represents the FFT length. The incoming signals are multiplied with the transfer function (3.6),

$$E_{F,X}[n] = E_X[n]H'[n] \tag{3.7}$$

and

$$E_{F,Y}[n] = E_Y[n]H'[n] \tag{3.8}$$

for the X and Y polarization, respectively. In (3.7) and (3.8), $E_X[n]$ and $E_Y[n]$ represent the FFT blocks of the incoming discrete time signals $e_X(k)$ and $e_Y(k)$, respectively and $E_{F,X}[n]$and $E_{F,Y}[n]$ represent the filtered signals in the X and Y

polarizations, respectively. Equations (3.7) and (3.8) are computed using the overlap-save scheme described in section 3.2.

The dispersion limited fiber distance varies inversely to the square of baud rate. So, the need for employing a CD equalizer is mainly governed by this dispersion limited fiber distance, or in other words the baud rate. As a rule of thumb, the dispersion limited fiber distance is 80 km for 10 Gbaud [48-59]. Therefore, an increase by a factor of 4 in baud rate to 40 Gbaud will reduce the dispersion limited fiber distance by a factor of 16 to 5 km fiber only.

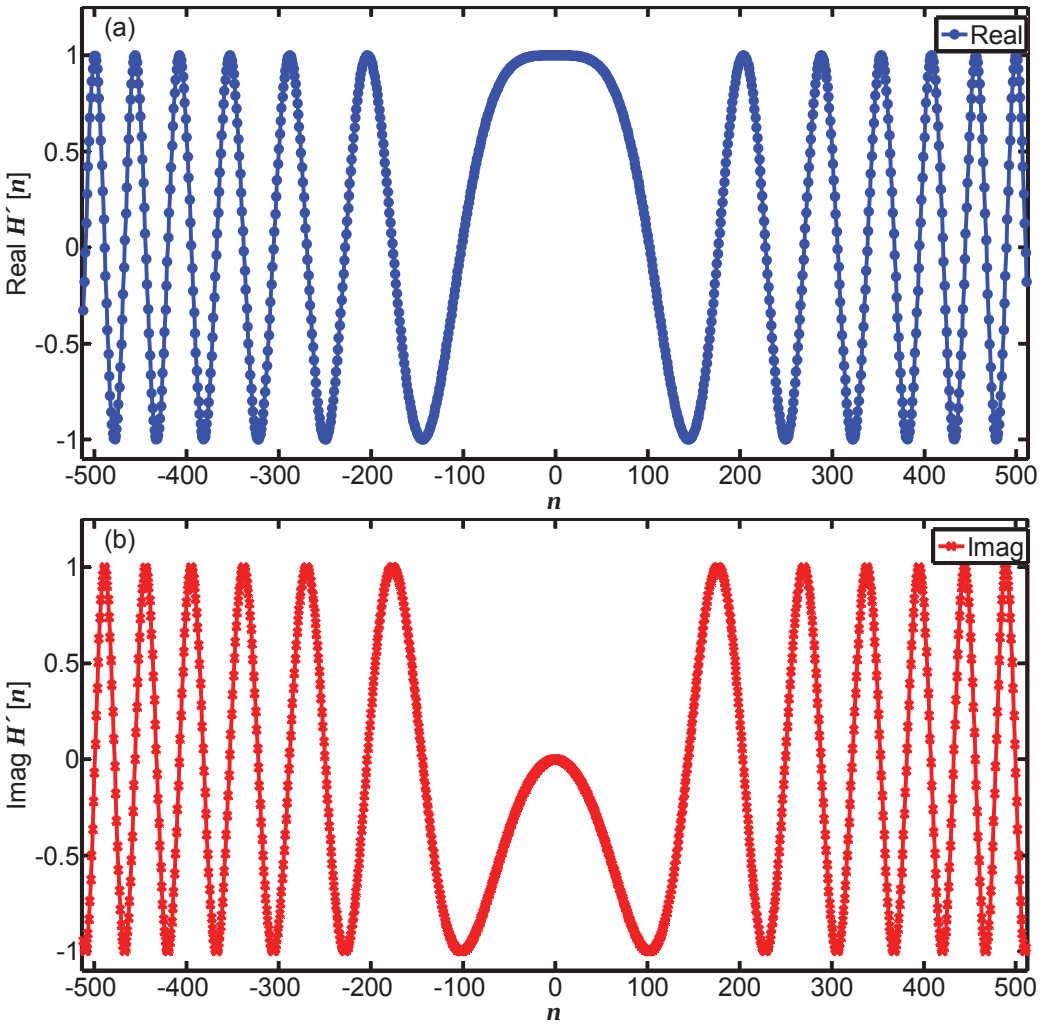

Figure 3.4: CD compensator transfer function at 2000 ps/nm computed over 1024 points (a) real part (b) imaginary part.

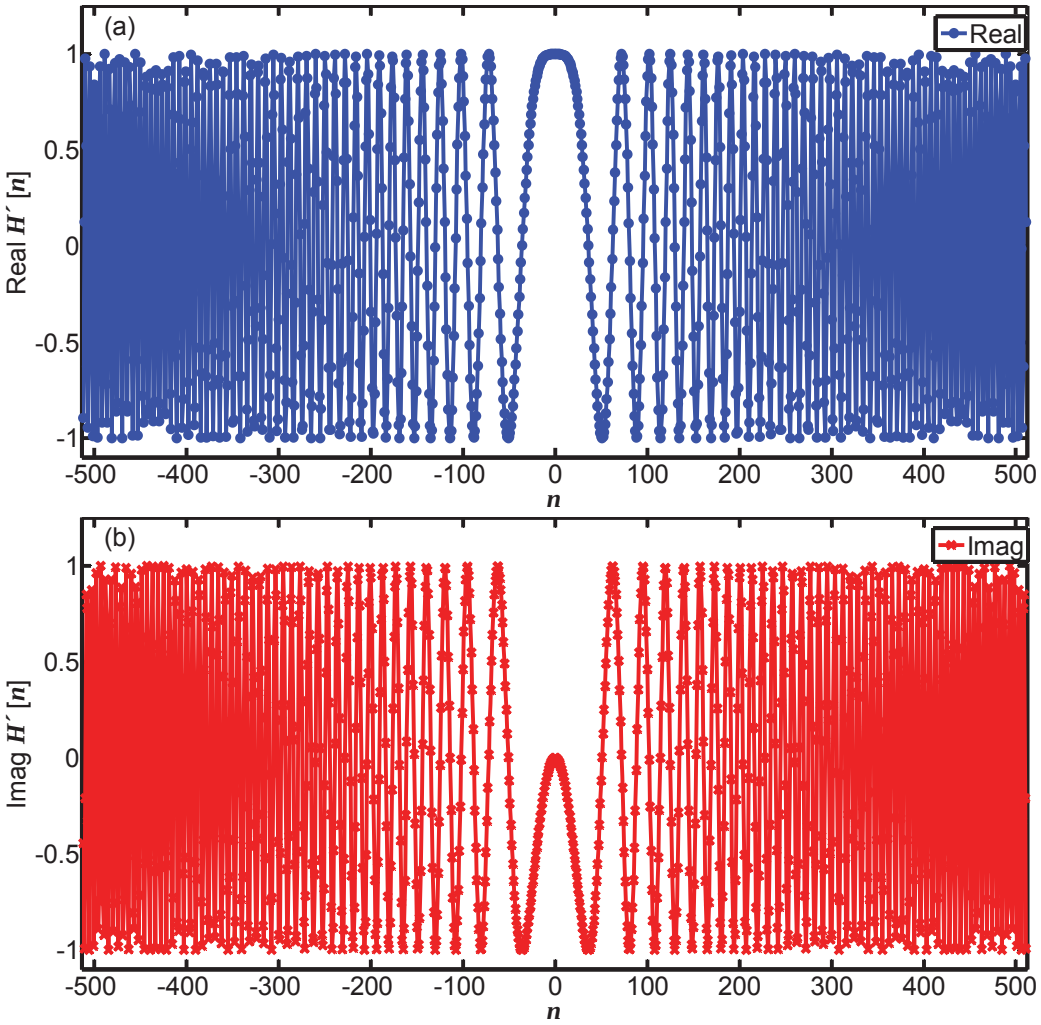

Figure 3.5: CD compensator transfer function at 16000 ps/nm computer over 1024 points (a) real part (b) imaginary part.

The simulated transfer function of the CD equalizer, in order to compensate 2000 ps/nm fiber CD, is shown in Figure 3.4. The real and imaginary parts are plotted in Figure 3.4 (a) and Figure 3.4 (b), respectively. Similarly, transfer function of the CD equalizer, in order to compensate 16000 ps/nm fiber CD, is shown in Figure 3.5. It can be noticed that the real and imaginary components of the equalizer transfer function have more frequent transitions as the fiber length increases.

The received constellations for both QPSK and 16-QAM signals are significantly distorted by CD present in the fiber, which results in ISI, as shown in Figures 3.6 (a) and 3.7 (a). In this case, the fiber link has 4000 ps/nm fiber CD. This corresponds to

fiber length of 250 km. However, the proposed FDE can compensate the ISI caused due to CD by using a sufficient number of FFT points for both PDM-QPSK and PDM-16-QAM systems. The constellation diagrams of the equalized QPSK and 16-QAM signals, using a 1024-point FFT based FDE, are shown in Figures 3.6 (b) and 3.7 (b).

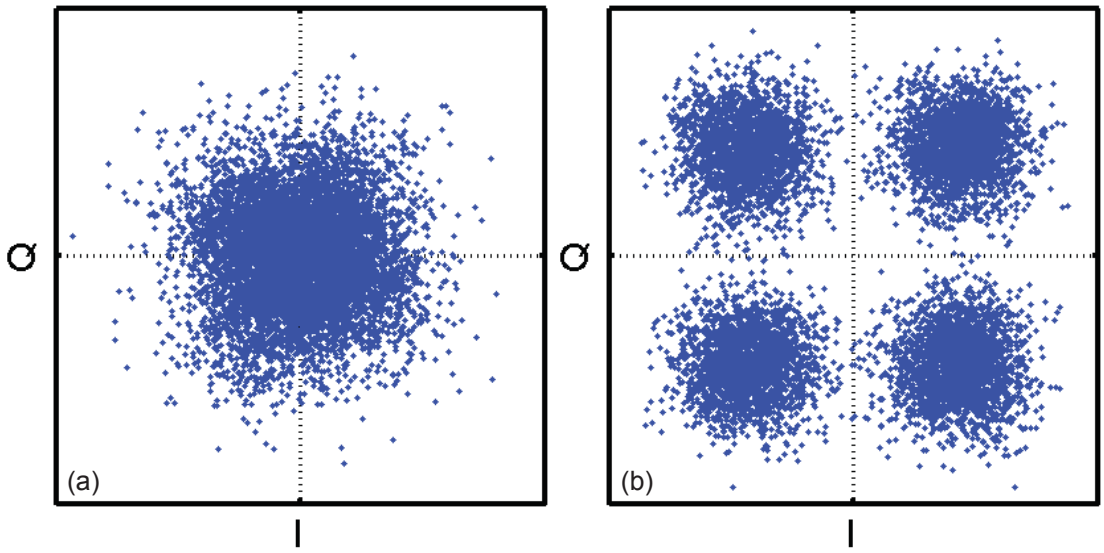

Figure 3.6: Received constellation diagram for QPSK (a) before CD equalizer (b) after CD equalizer.

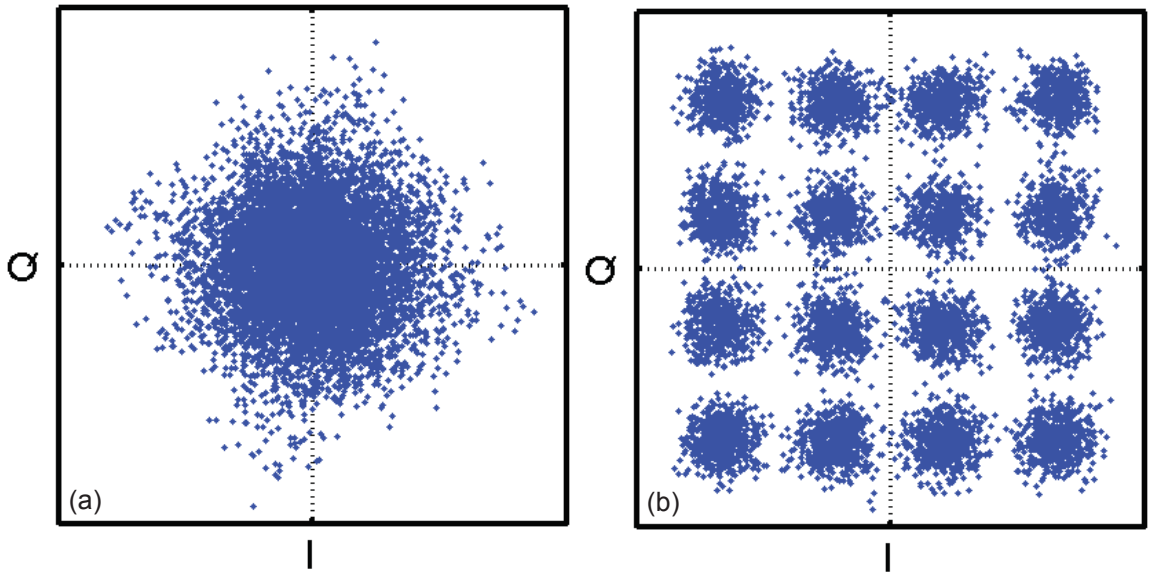

Figure 3.7: Received constellation diagram for 16-QAM (a) before CD equalizer (b) after CD equalizer.

Furthermore, in order to verify the long-haul performance, extended simulations have been conducted for different lengths of fiber (i.e. different amounts of fiber CD). Figure 3.8 shows the OSNR penalty for a BER of 10^{-3} at different transmission distances, described in terms of accumulated CD, for 256, 512 and 1024-point FFT processing in a 112 Gb/s PDM-QPSK system. It has been observed that FDE shows robust performance over large transmission distances. It is has been shown that 256, 512 and 1024-point FFT based FDEs can easily compensate up to 10000 ps/nm, 20000 ps/nm and 40000 ps/nm fiber CD, respectively, with a small OSNR penalty up to 0.7 dB or less. This corresponds to CD tolerance over fiber link distances of 625 km, 1250 km and 2500 km, respectively. With approximately 3 dB penalty, 256, 512 and 1024-point FFT based FDEs can easily compensate up to 12000 ps/nm, 24000 ps/nm and 48000 ps/nm fiber CD, respectively. This corresponds to fiber link distances of 750 km, 1500 km and 3000 km, respectively. Besides, it has been observed that when the FFT length of CD equalizer changes to the next power of 2, the CD tolerance of the equalizer also increases by two-fold.

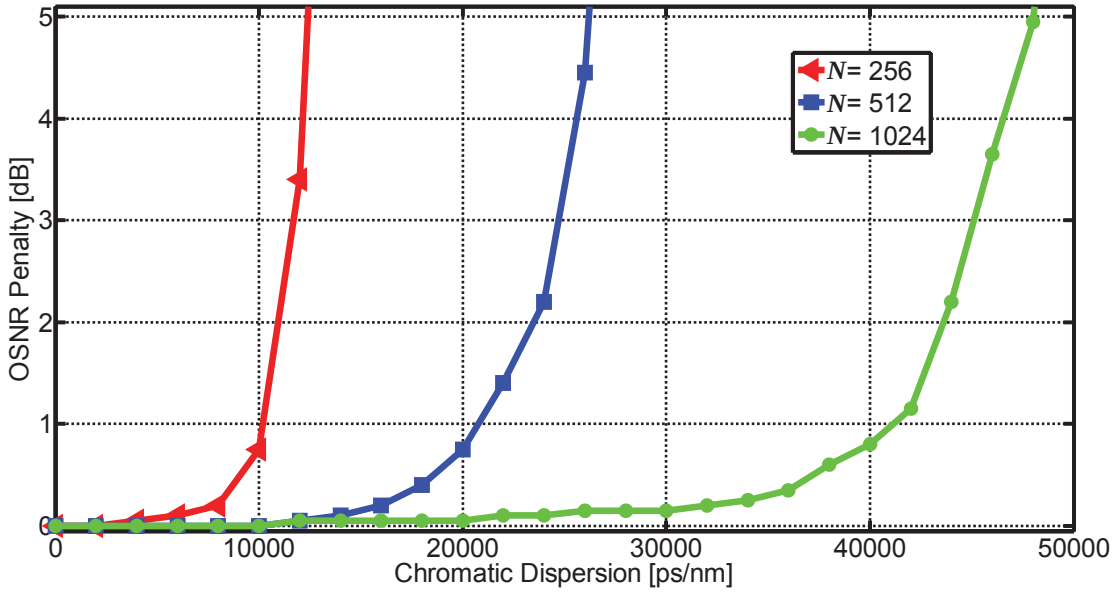

Figure 3.8: Chromatic dispersion tolerance of FDE for 112 Gb/s PDM-QPSK at different transmission distances (i.e. accumulated fiber CD).

Figure 3.9 compares the performance of FDE based CD equalization for 112 Gb/s PDM-QPSK and 224 Gb/s PDM-16-QAM systems. It can be seen that a 512-point

FFT based FDE can easily compensate up to 20000 ps/nm fiber CD for both 112 Gb/s PDM-QPSK and 224 Gb/s PDM-16-QAM systems. This corresponds to CD tolerance over fiber link distances of 1250 km with almost no or small OSNR penalty. As observed, FDE can easily be employed to 16-QAM. It is easily scalable to even higher order QAM formats.

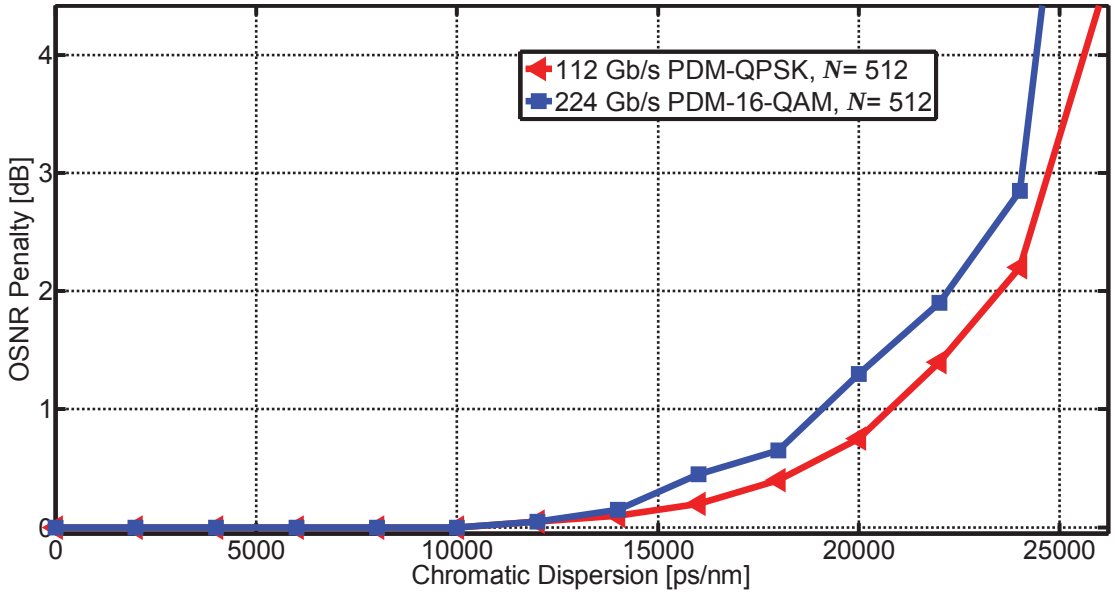

Figure 3.9: Comparison of the chromatic dispersion tolerance between 112 Gb/s PDM-QPSK and 224 Gb/s PDM-16-QAM at different transmission distances (i.e. accumulated fiber CD).

Figure 3.10 shows the FDE performance at different values of laser sum-linewidth-times-symbol-duration product ($\Delta f T_S$) for QPSK and 16-QAM signals. Viterbi and Viterbi (V&V) and QPSK partitioning (QPSKP) carrier phase estimation schemes have been employed for the QPSK and 16-QAM signals, respectively [26-31]. The fiber link has 4000 ps/nm fiber CD. This corresponds to fiber length of 250 km. FDE with 512 FFT points is employed for CD compensation. *K* represents the carrier phase estimator filter length. It has been observed that the shorter filter length i.e. *K*=9 is suitable for high values of $\Delta f T_S$. As expected, the QPSK signals are more linewidth tolerant than 16-QAM signals. Furthermore, it is evident that FDE is robust against large laser linewidths, for moderate fiber CD value of 4000 ps/nm. Laser sum-

linewidth-times-symbol-duration product up to 10^{-4} can be tolerated with small OSNR penalty.

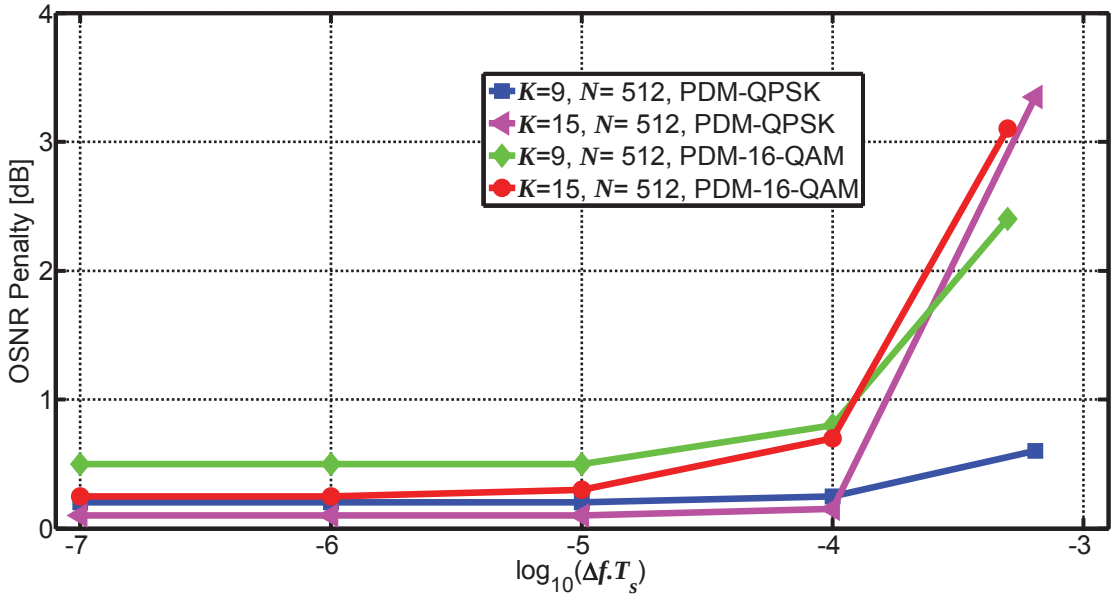

Figure 3.10: Linewidth tolerance of FDE for 112 Gb/s PDM-QPSK and 224 Gb/s PDM-16-QAM at 4000 ps/nm fiber CD.

3.4 Frequency Domain CD Equalization at Reduced Sampling Rates

Higher oversampling is usually employed to reduce the penalty that occurs in case of compensating a large amount of ISI [66-67]. On the contrary, the equalizer performance becomes dispersion limited at symbol rate sampling [68]. Therefore, frequency domain equalizers based on two samples per symbol are generally employed for ISI compensation.

Alternatively, the equalizer can be operated at reduced ADC oversampling rates (i.e. less than twice the baud rate) [69-71]. In this respect, one option is to interpolate the data at the output of ADCs to 2 samples per symbol. In this case, MATLAB™ function 'spline' is employed here that performs a cubic spline interpolation at the output of ADCs [39]. Consequently, the real and imaginary components of the incoming discrete time signals $e_X(k)$ and $e_Y(k)$, sampled at less than twice the baud rate, are interpolated to the new set of samples with data positions corresponding to 2

samples per symbol. So, the data at the output of ADCs at K number of discrete time positons, i.e. k times T_S ,

$$kT_S \in \{0, T_S, 2T_S, ..., (K-1)T_S\} \tag{3.9}$$

for an oversampling rate $R_S = 1/T_S$ (less than 2 samples per symbol) is interpolated to new discrete time positons

$$k'T_S' \in \{0, T_S', 2T_S', ..., (K'-1)T_S'\}. \tag{3.10}$$

Here, $R_S' = 1/T_S'$ corresponds to two times the symbol rate and $K' = K(R_S'/R_S)$ are the number of discrete time positons in the interpolated data.

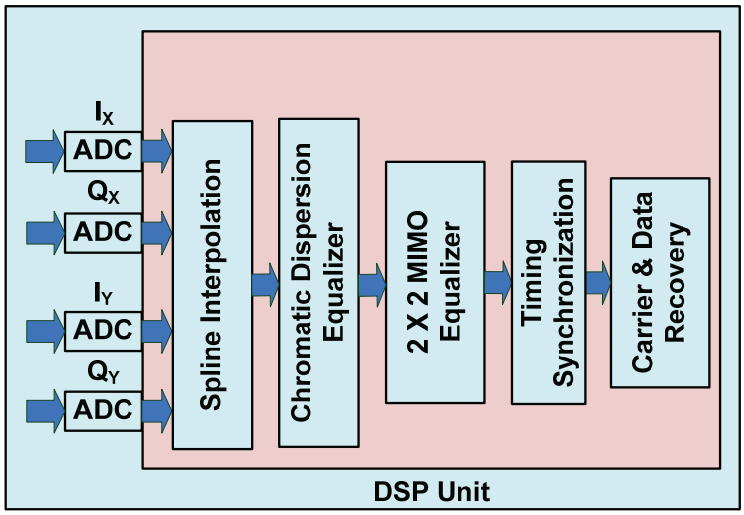

Figure 3.11: Spline interpolation applied to the ADC outputs for operating FDE at reduced ADC oversampling rates.

The spline interpolation can be employed to the ADC outputs for operating FDE at reduced oversampling rates as shown in Figure 3.11. Alternatively, the ADC outputs which are oversampled at less than 2 samples per symbol can be directly processed without any interpolation before the frequency domain equalizers. In this case, the equalizer transfer function (3.6) is modified accordingly for the new sampling rate R_s. It shall be noted that the concept of performing frequency domain equalization without interpolation strictly relates to the case of not applying interpolation at the ADC outputs, as shown in Fig. 3.11. For the 'without interpolation' case, the interpolator block in Figure 3.11 is eliminated and the filter sampling frequency changes.

However, this does not relate here to the timing recovery process and, in fact, interpolation will be needed at the timing synchronization module.

The FDE's performance against reduced oversampling rates of the ADC is shown in Figure 3.12, for QPSK and 16-QAM data at 4000 ps/nm fiber CD. A 512-point FFT based FDE is employed for CD compensation. The equalization performance is observed for both cases, without interpolation and with spline interpolation at the output of ADCs. The FDE performs marginally better with spline interpolation for QPSK and 16-QAM signals. Besides, it has been observed that the 16-QAM signals are more sensitive against reduced ADC sampling rates.

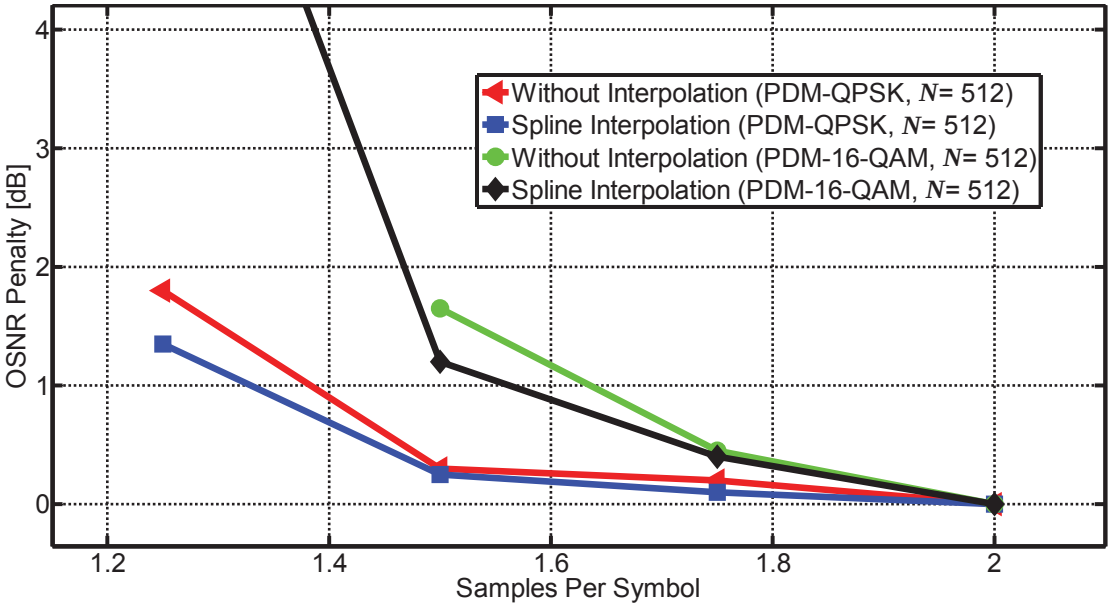

Figure 3.12: FDE performance for reduced oversampling rates of the ADC for 112 Gb/s PDM-QPSK and 224 Gb/s PDM-16-QAM systems at 4000 ps/nm fiber CD.

Furthermore, Figure 3.13 compares the performance of FDE based CD equalization at reduced ADC oversampling rate of 1.5 samples per symbol (with and without interpolation at the output of ADCs) at different fiber link lengths for 112 Gb/s PDM-QPSK. It can be observed that although there is a slight OSNR penalty in employing reduced oversampling rate, but without interpolation the robustness of the FDE is extended over larger fiber distance. Thus, without interpolation more accumulated fiber CD can be tolerated. So, this somehow is an advantage which is attained

obviously as a result of a tradeoff. Consequently, in this case, the FFT size of the frequency domain equalizer needs not to be increased to the next power of 2 (for much larger fiber distance) that leads to a reduction in the computational effort. Whereas, at 1.5 samples per symbol, with spline interpolation the ONSR penalty is just marginally less than without interpolation.

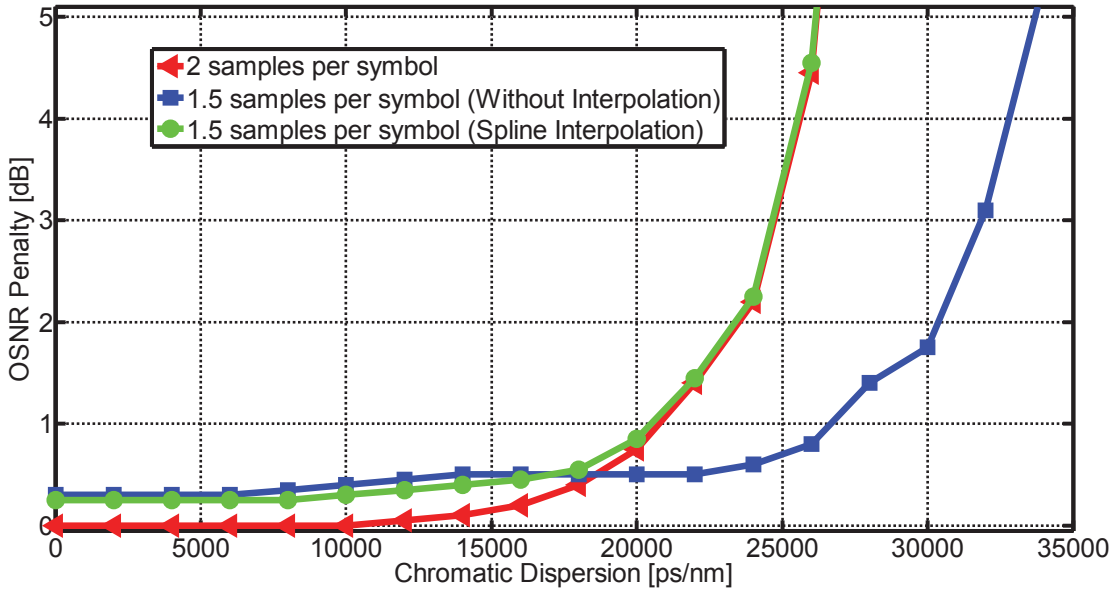

Figure 3.13: Comparison of the chromatic dispersion tolerance for reduced ADC oversampling rate (1.5 samples per symbol) at different transmission distances (i.e. accumulated fiber CD).

Since the demand for high data-rates is ever increasing, ADCs with high sampling rates are required at the input of DSPUs. However, the use of reduced oversampling rates in FDEs with low performance degradation can enable use of low-cost ADCs with low sampling rates. In this respect, 1.5 samples per symbol or even lower ADC oversampling rates can be used with small OSNR penalty. Furthermore, it also lowers the sampling rate demand for real-time sampling oscilloscopes (RTOs). These RTOs are an important tool for the performance analysis and offline digital signal processing of high capacity fiberoptic systems. However, it must be remembered that the spline interpolation requires additional computational effort in the equalization process. There is in fact a trade-off between computational effort and a marginal performance improvement. It might be preferred to sacrifice, by having a marginal OSNR penalty,

for a reduced computational effort. For this reason, investigation related to spline interpolation has been kept limited to this section only and it is not considered in the following sections of this dissertation.

3.5 Discussion on Computational Effort and Performance

The TD-FIR based CD equalizer uses discrete time convolution. In terms of computational effort a TD-FIR based CD equalizer requires,

$$C_M = {N_{TDE}}^2 \tag{3.9}$$

complex multiplications and

$$C_A = N_{TDE}(N_{TDE} - 1) \tag{3.10}$$

complex additions for processing incoming data block of length N_{TDE}. So, as an example, a 243 tap TD-FIR equalizer requires 59049 complex multiplications and 58806 complex additions for processing data of block of length 243. For only a 243 tap equalizer the computational complexity is already very high. Moreover, it can equalize only up to 10000 ps/nm fiber CD. In terms of computational effort per sample, this corresponds to 243 complex multiplications and 242 complex additions. Therefore, TD-FIR is not suitable for the compensation of large amount of fiber CD because large number of equalizer taps would be required. Consequently, the computational complexity of the CD equalizer will also increase.

In case of FDE based CD compensation, the FFT implementation employing the radix-2 algorithm requires

$$C_M = (N/2)\log_2 N \tag{3.12}$$

complex multiplications and

$$C_A = N \log_2 N \tag{3.13}$$

complex additions. Hence, the overlap-save method based FDE requires $(N/2)\log_2 N$ complex multiplications for the FFT operation at the input, N complex

multiplications to realize filtering and $(N/2)\log_2 N$ complex multiplications for the IFFT operation at the output. Overall,

$$C_M = N\log_2 N + N \tag{3.14}$$

complex multiplications are required for the processing of one data block of length N in the FDE. Furthermore, the overlap-save method based FDE requires $N\log_2 N$ complex additions for the FFT operation at the input and $N\log_2 N$ complex multiplications for the IFFT operation at the output. So,

$$C_A = 2N\log_2 N \tag{3.15}$$

complex additions are required for the processing of one data block of length N in the FDE. Therefore, as an example, a 1024 point FFT based FDE would require 11264 complex multiplications and 20480 complex additions to equalize one data block of length 1024. This 1024-point based FDE is capable of compensating 48000 ps/nm of fiber CD, as seen in section 3.3. It enables robust data transmission over 3000 km fiber link without the need of any inline dispersion compensation. In terms of number of operations per sample, this corresponds to 22 complex multiplications and 40 complex additions.

The TD-FIR equalizer has a linearly increasing complexity as the number of required taps increase [50]. On the other hand, FDEs require much lower computational effort. Hence, based on the above discussion, it is confirmed that FDE is a better option than the TD-FIR equalizer for fiber links with large CD.

Chapter 4

Adaptive Blind FD Chromatic Dispersion Equalization

This chapter extends the work related to CD compensation in the digital domain to include blind adaptation feature. Section 4.1 introduces the blind CD equalization. Adaptive search based frequency domain (FD) CD estimation technique is presented in section 4.2. Adaptive CD estimation in the presence of PMD is presented in section 4.3. The blind CD estimation performance at reduced sampling rates is presented in section 4.4. Section 4.5 discusses the work, presented in this chapter, in terms of complexity and performance. Overall, this chapter presents the work done related to blind adaptive CD compensation along with the performance analysis and simulation results.

4.1 Blind Chromatic Dispersion Equalization

In digital CD equalizers, the fiber CD has been commonly considered to be known a priori [48-49]. However, the future optical networks need to adaptively reconfigure to dynamic CD changes in the channel. So, it is essential that the CD equalizers adaptively compensate CD present in the channel. In this perspective, the fiber CD can either be estimated using pilot symbols [72-73] or estimated blindly [74-86]. The training symbols based CD estimation techniques have additional overhead and therefore there is an inherent reduction in spectral efficiency. So, the blind FD CD estimation technique is considered here. CD can be estimated as a side process since it is a quasi-static fiber transmission impairment. In this respect, it is essential that the blind CD estimation is fast enough, that is less than 5 ms, to enable fast re-routing in the optical network [83].

Blind (non-data aided) CD estimation algorithms normally require some cost function to be computed using a filter function over a range of possible CD values. Consequently, there would be undesired computational complexity or latency in the CD estimation process. FD techniques have simplified the blind CD estimation to some extent by using the Godard clock-tone (CT) algorithm [78-80]. Furthermore, FD CD estimation techniques can make use of FFTs of the incoming signals. These FFTs will be available in any case if the CD equalizer is implemented in frequency domain. In this technique, for each CD value one point of the autocorrelation function of a product spectrum is calculated, the product of received signal spectrum and applicable CD filter function. So, in terms of DSP a lot of additions, multiplications, and a large look-up table (memory resources) would still be needed.

Recently, there have been efforts for finding minimum complexity CD estimation algorithms [82-83]. In this respect, a simplified CD estimation technique based on the autocorrelation of the signal power waveform is presented in [82], but it is limited by the bandwidth of the optical bandpass filter at the RX. Also, a CD estimation technique employing an FFT-based mapping has been presented in [83] to simplify these hardware resources consuming heuristic approaches. However, there is very limited control over the adjustment of minimum and maximum fiber CD values and the resolution of these values.

Therefore, a two-step adaptive approach for blind estimation of fiber CD in the frequency domain is proposed. In this respect, it is essential that the CD estimation algorithm is computationally efficient and modulation format transparent i.e. it can be implemented for different modulation formats.

4.2 Adaptive Search based FD CD Estimation

In the DSP enabled coherent receivers, the fiber CD is estimated blindly as a side process and then fed to the FDE. Figure 4.1 shows the block diagram of a digital coherent PDM system and its DSP unit. The DSP unit also includes the blind FD CD estimator module incorporated with CD equalizer module. Depending upon the switching speed of channel, this side process updates the accumulated fiber CD information from time to time.

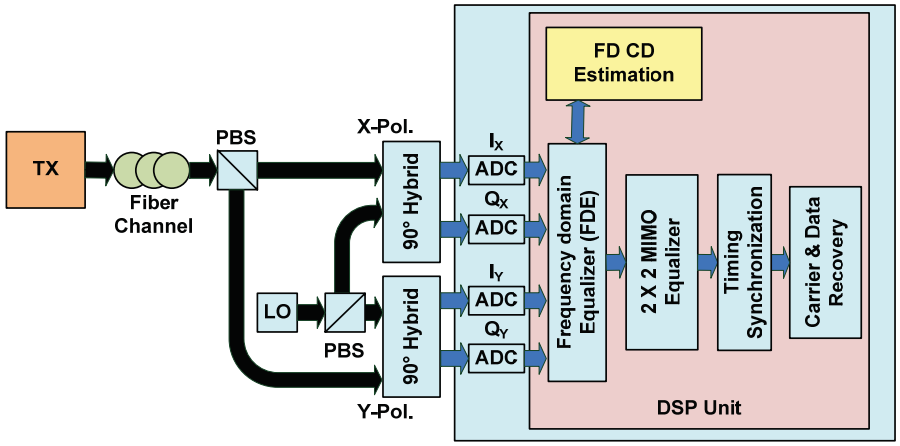

Figure 4.1: Digital coherent PDM system along with the modular depiction of the DSP unit (including the *Blind FD CD Estimator*).

The RX data blocks at the input of the FDE are converted into the frequency domain by an FFT of size N. Blind FD CD estimation takes place based on the N-point FFT data blocks. In order to determine the actual CD compensator filter function to be used for FDE, Godard's CT based estimation is applied [87]. Godard's CT component occurs at the frequency index

$$N' = \frac{NB}{R_S}, \tag{4.1}$$

where B is the symbol rate. The presence of fiber CD affects the magnitude of CT. In fact, its magnitude is found to be inversely proportional to the amount of CD present in the channel [78, 86]. For the case when there is no fiber CD present in the channel, a reliable BER is obtained at the initial signal acquisition. Therefore, CD estimation and equalization is not needed in this case. This phenomenon is utilized here, by employing the compensating filter function, to restore the clock tone component. In this chapter, it will be demonstrated with simulations that a correct choice of compensating function mitigates the accumulated CD and thus will result in a CT, even if the value of fiber CD is very large. For a two-fold oversampled signal (which is considered in this section) the digital clock tone component is detected at index $N' = N/2$. Godard's CT can be observed only with oversampling of the RX signals at the input ADCs.

The CD compensator filter function, according to (3.6), can be written as

$$H'_{CDi}[n] = e^{-j\frac{\pi\lambda^2 {R_s}^2 CD_i}{cN^2}n^2} \tag{4.2}$$

In (4.2), CD_i is the applied CD, which ideally is the negative of the fiber CD to be compensated. It may be noted that the CD compensator filter functions can be stored in a look-up table from the hardware implementation point of view. For the purpose of later estimating the necessary compensator CD an index *i* is defined by

$$CD_i = \Delta s \cdot i \tag{4.3}$$

where Δs represents the stepsize of the CD scan range. So, the estimator cost function can scan over the negative of the minimum and maximum possible fiber CD values in that scan region using (4.3).

The stepsize Δs in (4.3) must be carefully and optimally selected. A large value of Δs above 400 ps/nm would not result in an optimal execution of Godard's CT detection, thus estimating CD erroneously. On the other hand, a small value of Δs would lead to better precision of the blind CD estimator. However, a large number of the compensating filter functions i.e. (4.2) would need to be processed in the DSP, thereby driving up the number of computations. The equalized spectrum $E_F[n]$ filtered by the CD compensator (4.2) is given by

$$E_F[n] = E[n]H'_{CD_i}[n] \tag{4.4}$$

where $E[n]$ is the received signal spectrum in X or Y polarization. Here, these signal spectra correspond to FFT blocks of $e_X(k)$ and $e_Y(k)$, i.e. $E_X[n] = FFT\{e_X(k)\}$ and $E_Y[n] = FFT\{e_Y(k)\}$. These FFTs have *N* points.

So, Godard's CT-based cost function

$$J_{CT}[i] = \left| \sum_{n=0}^{N'-1} E_F^*[n]E_F[n+N'] \right| \tag{4.5}$$

is obtained by the *N*-cyclic autocorrelation of the received signal spectrum after its filtering by the CD equalizer function. It shall be noted that (4.5) contains the sum of the multiplied (filtered) spectra $E_F^*[n]E_F[n+N']$ upto $N'-1$ only. In general, one

might compute this sum upto $N-1$. However, as observed from the simulation results that will be presented in the following part of this chapter, computation of sum in (4.5) only upto $N'-1$ provides sufficient estimation. Thus, the computational effort in this case can be reduced. The shift N' in the filtered spectrum $E_F[n]$ relating to Godard's CT is computed using (4.1). * means the complex conjugate. The physical meaning is that Godard's timing recovery properties are observed at the clock tone. In theory the presence of fiber CD deteriorates the clock recovery. So, the matching filter function in (4.5) restores Godard's clock tone component. Consequently, the matching filter function indicates the compensator CD to be applied.

It is clear from (4.5) that it requires computations over the index *i* i.e. heuristic cost function computations over a range of CD compensator filter functions. Consequently, (4.5) can be altered and simplified into an expression [83] where multiplication with different filter functions is not required

$$J_{FFT}[n'] = \left| FFT\{E^*[n]E[n+N']\} \right|. \tag{4.6}$$

The FFT in (4.6) has N' points. This spectrum allows estimating the needed compensator CD as

$$CD_{FFT} = -\frac{\arg(\max_{n'} J_{FFT}[n'])c}{\lambda^2 B^2}. \tag{4.7}$$

By $\arg(\max_{n'} J_{FFT}[n'])$ that index n' is meant which corresponds to the maximum value of J_{FFT}. Initially, (4.6) is used as the FFT-based mapping over a range of CD values in steps of size

$$\Delta s_1 = \frac{c}{\lambda^2 B^2}. \tag{4.8}$$

This corresponds to CD search resolution of 159 ps/nm for the simulated 28 Gbaud system. The FFT bin n' corresponding to the maximum value of J_{FFT} is used to initially estimate CD_{FFT}. Here n' is mapped to this initial CD estimate CD_{FFT} by (4.7). This single FFT brings us in a first step close to the true CD, however, not yet with sufficient resolution.

For the second step a new region ΔCD =-400 ps/nm around CD_{FFT} is defined with scan steps of Δs_2 = 40 ps/nm. In general, Δs_2 might theoretically attain any value less than Δs_1 and greater than or equal to 1 ps/nm. However, we find that for high CD search resolutions, i.e. values of Δs_2 that are smaller than 40 ps/nm, the cost function becomes mostly insensitive to changing values of i. Hence, we set Δs_2 = 40 ps/nm for simulations considered in this chapter. An optimized index search based on the CT expression is performed using (4.5), but with a normalized threshold (NT). In order to obtain it, all the values computed by (4.5) are normalized by the maximum value detected by (4.6). The optimized and precise CD estimate is given by a search (for convenience in negative direction) through the indices

$$i = \frac{\left(CD_{FFT} - \Delta CD/2\right)}{\Delta s_2} \cdots \frac{\left(CD_{FFT} + \Delta CD/2\right)}{\Delta s_2}. \tag{4.9}$$

in conjunction with (4.3). That index i_{CT} is chosen which yields the maximum value of J_{CT} ; the corresponding CD is

$$CD_{CT} = \Delta s_2 \cdot i_{CT}\,. \tag{4.10}$$

The optimized and precise estimated CD value CD_{CT} would correspond to the index of (4.5) where the absolute value of the cost function exceeds the NT. Besides, it must also satisfy $J_{CT}[i] > J_{CT}[i \pm 1]$ as a condition to obtain a global maximum and avoid erroneous CD estimation. Figure 4.2 enumerates the steps required for blind FD CD estimation. As observed in (4.5) and (4.6), the cost functions can estimate CD for even higher order QAM modulation formats because they do not depend on the power rings associated with QAM signals. This is contrary to [74], where the CD estimator utilizes a TD cost function that works well for QPSK only and needs modifications to estimate CD for higher order QAM modulation formats.

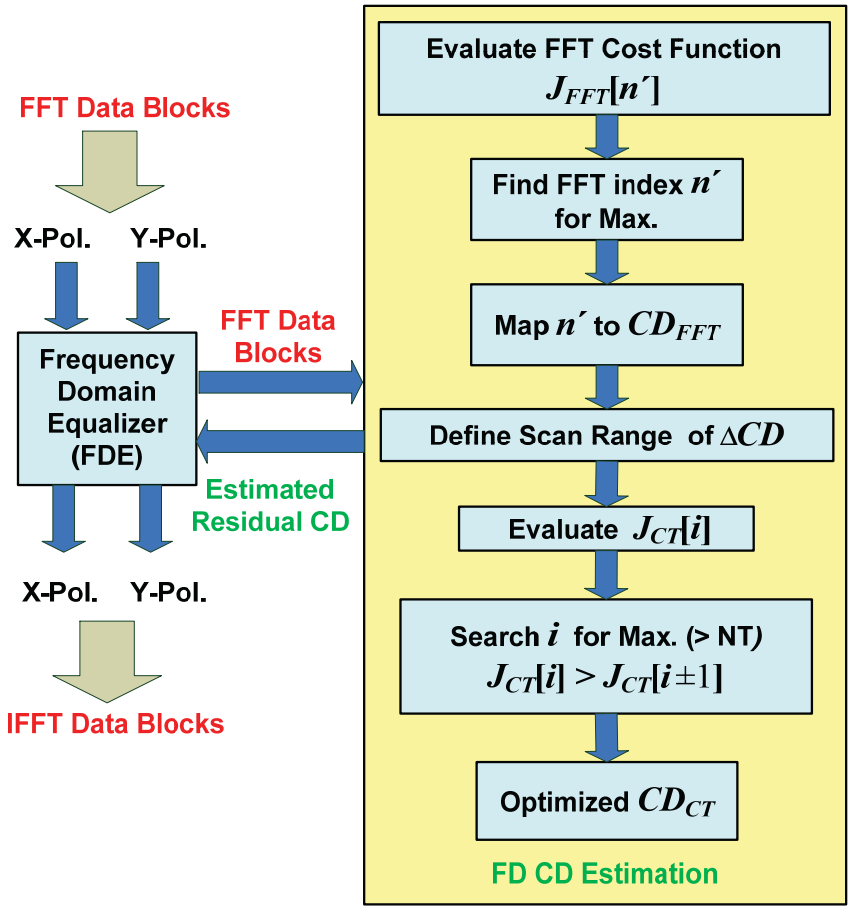

Figure 4.2: Schematic of the blind FD CD estimation algorithm incorporated with a CD equalization subsystem.

Therefore, the proposed algorithm yields two advantages. Firstly, the usage of J_{CT} as a second step search gives control over the CD search resolution, which is not provided in [83]. Because [83] adopts an approach where the stepsize Δs_1 is defined according to (4.8), so in this case the resolution can only be varied by changing B. Secondly, in this case, there is no need to search all possible J_{CT} values because of the NT based search, unlike algorithms in [77-80]. A scanning resolution of 200-1000 ps/nm has been employed in recent work [79, 81]. However, for the proposed algorithm a high resolution stepsize of 40 ps/nm is employed while achieving a significantly lower complexity.

In order to merit the performance of the CD estimator, a higher laser sum-linewidth-times-symbol-duration product ($\Delta f T_S$) of 10^{-4} is used. This is compatible with

linewidths of available distributed feedback lasers. The blind CD estimator computes over 5 FFT-blocks of the received data in order to average and reduce the effect of noise. Therefore, 2560 symbols per polarization are used for the CD estimation. Due to the overlap-and-save method the FFT size is 1024. The number of symbols used here for CD estimation is lower than in other such techniques [80-81]. 3072 and 24360 symbols have been used for CD estimation in [80] and [81], respectively.

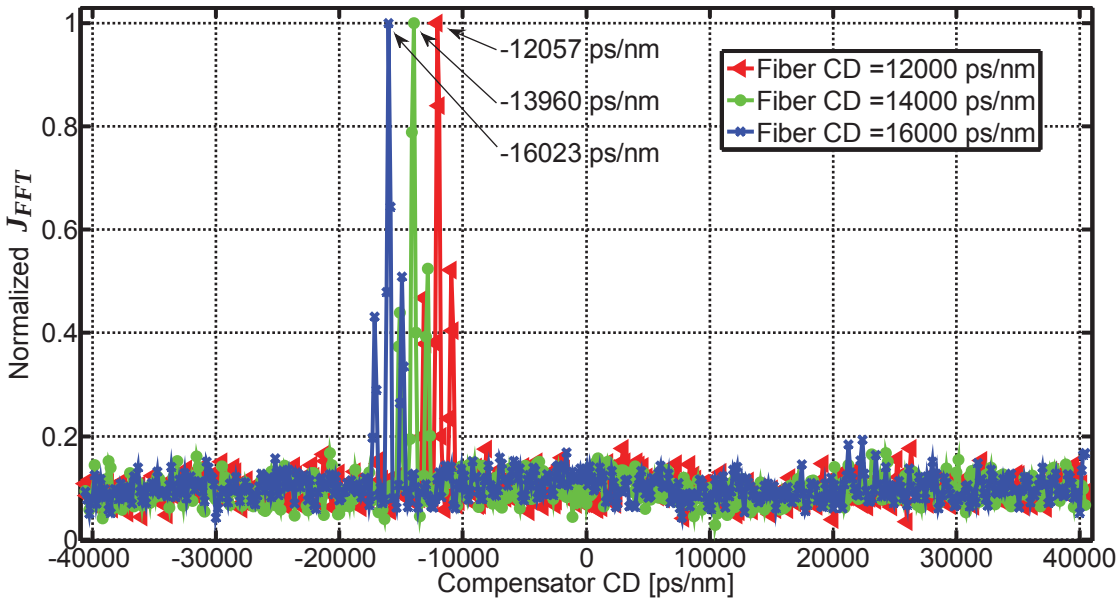

Figure 4.3: Initial search based on the FFT mapping expression around the fiber CD values of 12000 ps/nm, 14000 ps/nm and 16000 ps/nm.

The performance of the estimation technique is evaluated for different fiber CD values. The initial CD search based on the FFT mapping expression (4.6) with fiber CD values of 12000 ps/nm, 14000 ps/nm and 16000 ps/nm is shown in Figure 4.3 as an example for return-to-zero (RZ)-PDM-QPSK. There is an apparent deviation of estimated CD values in the initial search. The maxima occur at -12057 ps/nm, -13960 ps/nm and -16023 ps/nm for fiber CD of 12000 ps/nm, 14000 ps/nm and 16000 ps/nm, respectively.

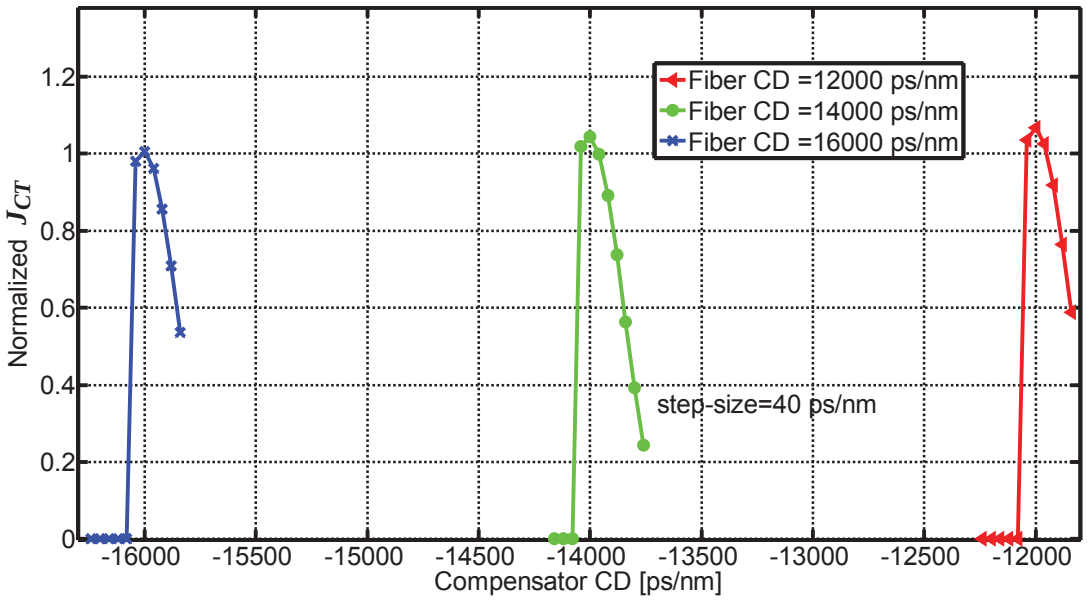

Figure 4.4: Optimized search based on the CT threshold for fiber CD values of 12000 ps/nm, 14000 ps/nm and 16000 ps/nm. Vicinity is scanned in negative direction with 40 ps/nm resolution by varying the applied compensator CD.

However, precise CD estimates are obtained after the index search using (4.5) based on the CT threshold (Figure 4.4). It scans for maxima having an NT exceeding 0.8 and satisfying the global maximum condition. Once the global maximum condition corresponding to the accurate CD estimate is obtained, the blind CD estimator stops the search process immediately.

In order to further verify the performance of this algorithm, histograms of the CD estimation error have been computed over different scenarios. So, 6000 random independent channels with different fiber CD values have been generated for each TX/RX scenario. In this respect, the values of fiber CD are randomly varied in the range of ±40000 ps/nm with a uniform distribution. An FFT size of 1024 is sufficient to estimate CD in this range. Figure 4.5(a) shows the CD estimation error histogram at different OSNR values for non-return-to-zero (NRZ)- and RZ-PDM-QPSK. Similarly, the CD estimation error histogram at different OSNR values for NRZ- and RZ-PDM-16-QAM is shown in Figure 4.5(b).

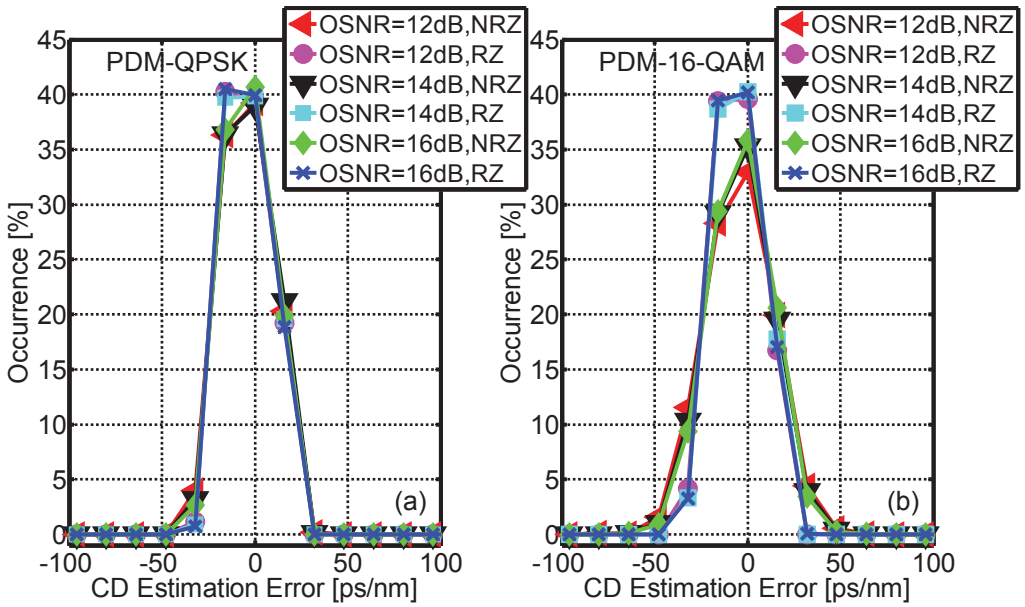

Figure 4.5: CD estimation error histogram at different OSNR values for (a) 112 Gb/s NRZ- and RZ-PDM-QPSK (b) 224 Gb/s NRZ- and RZ-PDM-16-QAM.

Figures 4.6 (a) and 4.6 (b) show the CD estimation error histogram at different values of $\Delta f T_S$ for NRZ- and RZ-PDM-QPSK and NRZ- and RZ-PDM-16-QAM. There is negligible performance degradation in the CD estimation for NRZ compared to RZ data (Figures 4.5 and 4.6). This is because RZ data has a strong clock component in the modulation spectrum. However, it is evident that the maximum CD estimation error remains confined to the region of ±50 ps/nm (Figures 4.5 and 4.6) for all the TX/RX scenarios. This CD estimation error is negligible because the second stage MIMO equalizer (presented in the next chapter) will also compensate the residual CD. Consequently, the proposed non-data aided CD estimation algorithm can efficiently and accurately work for different modulation formats and pulse shapes, even in the presence of noise.

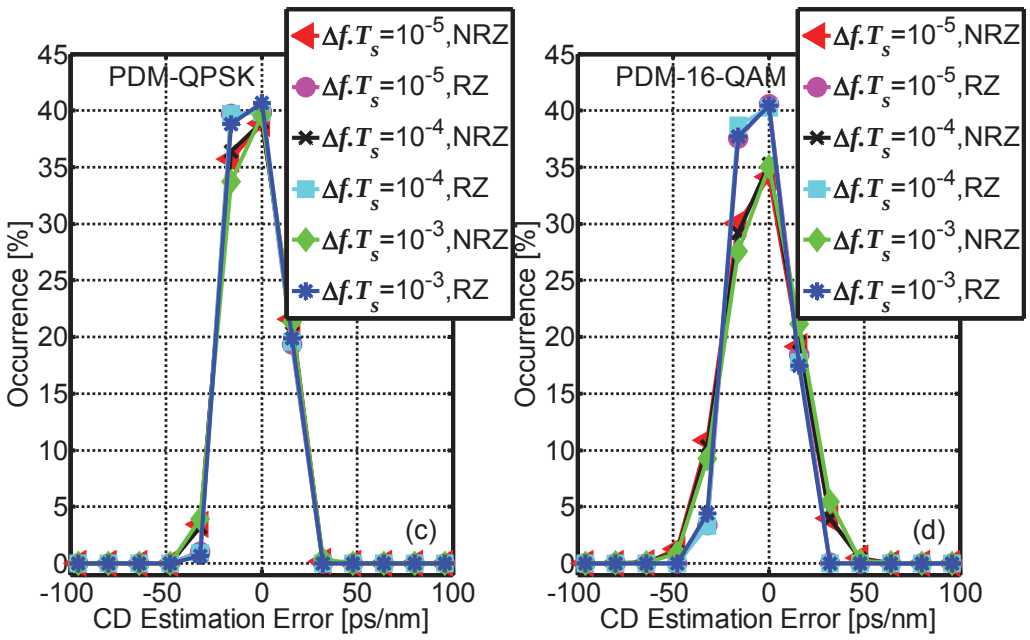

Figure 4.6: CD estimation error histogram at different values of $\Delta f T_S$ for (a) 112 Gb/s NRZ- and RZ-PDM-QPSK (b) 224 Gb/s NRZ- and RZ-PDM-16-QAM.

4.3 Blind FD CD Estimation in the Presence of PMD

This section presents the performance analysis of blind FD CD estimation in the presence of large DGD values. Using (4.5), the cost functions i.e. autocorrelations for the X and Y polarization spectra can be computed separately and then their respective contributions can be added. However, for channels with polarization distortions such as high mean DGD values, it is proposed that cost functions for the crosscorrelations of the X/Y polarization spectra must also be computed and their respective contribution can be added [85]. This refers to summations

$$\left|\sum_{n=0}^{N'-1} E_{F,X}^{*}[n]E_{F,X}[n+N']\right| + \sum_{n=0}^{N'-1} E_{F,Y}^{*}[n]E_{F,Y}[n+N'] + \sum_{n=0}^{N'-1} E_{F,X}^{*}[n]E_{F,Y}[n+N'] + \left|\sum_{n=0}^{N'-1} E_{F,Y}^{*}[n]E_{F,X}[n+N']\right|.$$

The first step FFT mapping based CD search with fiber CD value of 22000 ps/nm is shown in Figure 4.7 as an example for RZ-PDM-QPSK at mean DGD values of 25 ps, 50 ps and 75 ps, respectively. The maxima occur with an apparent deviation in the

estimated CD values. In this initial CD search, like last section, the stepsize is Δs_1 =159 ps/nm for the setup. It is can be observed that the width of the detected peak increases slightly with an increase in the mean DGD value.

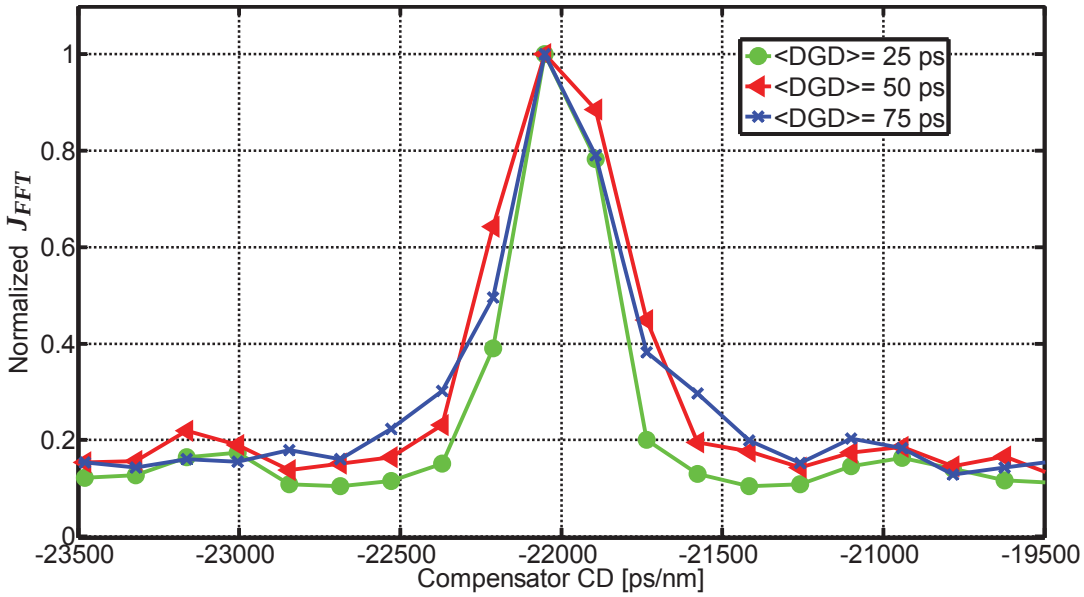

Figure 4.7: FFT mapping expression based initial search at different mean DGD values around the fiber CD value of 22000 ps/nm as an example.

Furthermore, precise and optimized CD estimates are obtained after the second step search as shown in Figure 4.8. As observed, the CD estimation algorithm shows resilience against large mean DGD values present in the fiber.

Besides, the performance of this two-step algorithm is further verified by computing histograms of CD estimation error over 6000 random independent channels with PMD for each TX/RX scenario. As previously, the fiber CD is randomly varied in the range of ±40000 ps/nm. Figure 4.9 (a) shows the CD estimation error histogram at 25 ps, 50 ps and 75 ps DGD for NRZ- and RZ-PDM-QPSK. Similarly, Figure 4.9 (b) shows the CD estimation error histogram for NRZ- and RZ-PDM-16-QAM. Therefore, this blind CD estimation algorithm is robust against high DGD values for PDM-QPSK and 16-QAM systems.

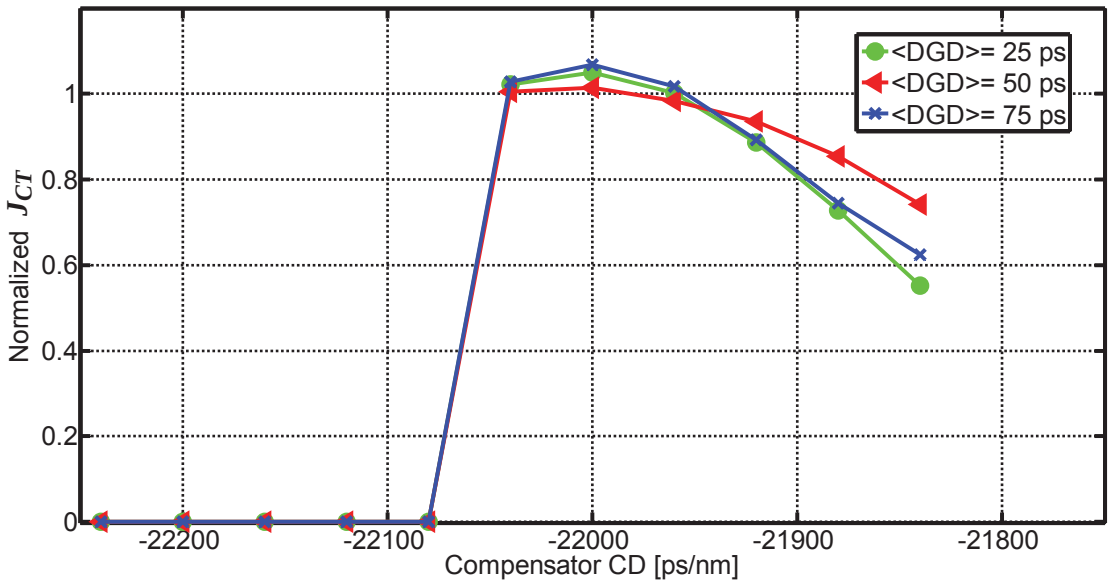

Figure 4.8: NT based optimized search at different mean DGD values around the fiber CD value of 22000 ps/nm as an example. It is scanned in negative direction with 40 ps/nm resolution by varying the applied compensator CD.

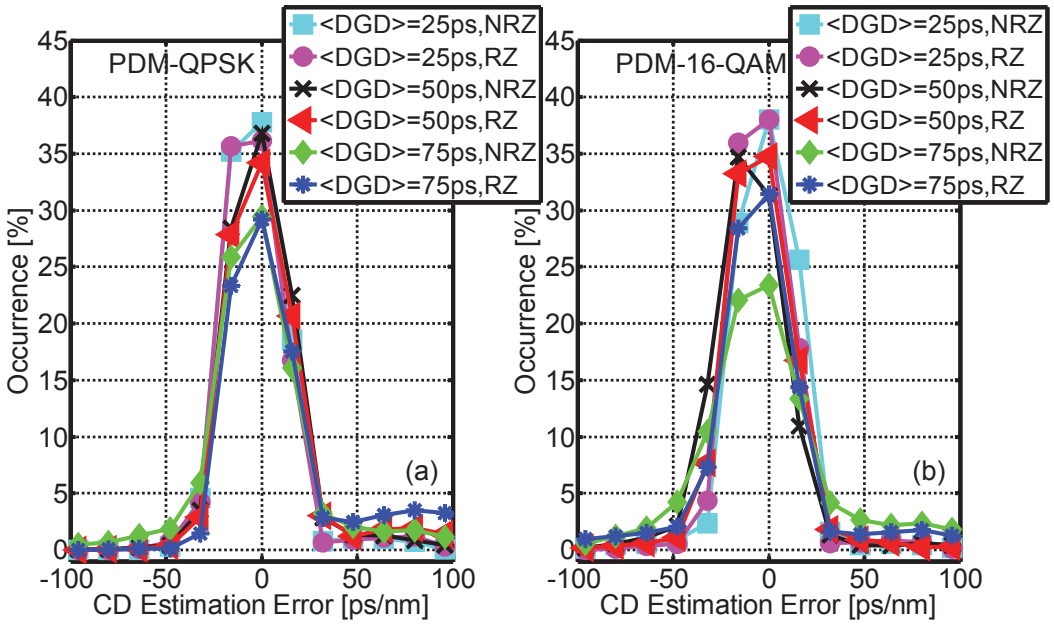

Figure 4.9: CD estimation error histogram at different mean DGD values for (a) 112 Gb/s NRZ- and RZ-PDM-QPSK (b) 224 Gb/s NRZ- and RZ-PDM-16-QAM.

4.4 Blind FD CD Estimation at Reduced Sampling Rates

In this section, the two-step blind CD estimation algorithm is generalized to be applicable to reduced ADC oversampling rates. In (4.6), N' is non-power of 2 for reduced oversampling rates yielding non-optimal FFT implementation. In such cases, $N''-N'$ zeros are padded to attain FFT blocks with next power of 2 points [86] as shown in Figure 4.10.

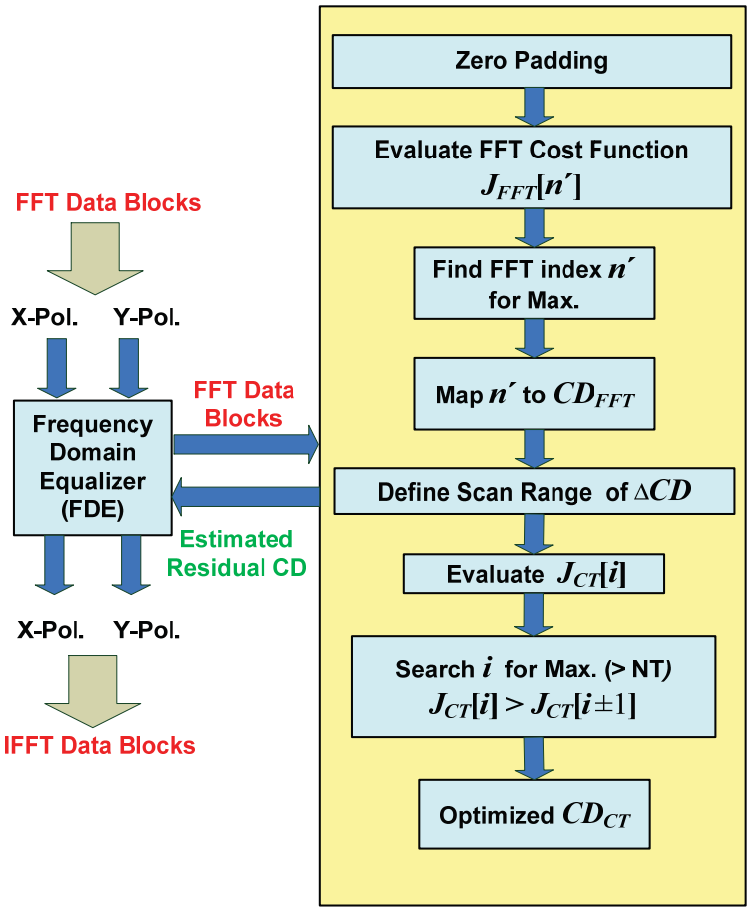

Figure 4.10: Schematic of the blind FD CD estimation algorithm for reduced ADC oversampling rates.

The fiber CD can now be estimated for reduced ADC oversampling rates using the zero padded signal blocks,

$$CD_{FFT} = -\frac{N' \arg(\max_{n'} J_{FFT}[n'])c}{N''\lambda^2 B^2} \quad . \tag{4.11}$$

Here N'' is the FFT size that refers to the next power of 2 greater than N'. That means $N'' = N'$ for the special case when N' itself is a power of 2. Initially, (4.11) is used as the FFT mapping based coarse CD search over a range of CD values. The coarse CD search resolution can be defined as

$$\Delta s_1 = \frac{N'c}{N''\lambda^2 B^2}. \tag{4.12}$$

A specific definition of coarse CD search resolution for two times oversampling has been presented in section 4.2. Whereas, equation (4.12) is a general definition of the coarse CD search resolution that is applicable to any ADC oversampling rates e.g. 159 ps/nm at $R_S = 2B$ holds as in (4.8). However, (4.12) can be employed only if the ADC oversampling rate is greater than one sample per symbol. The clock tone component cannot be detected for ADC sampling at baud rate.

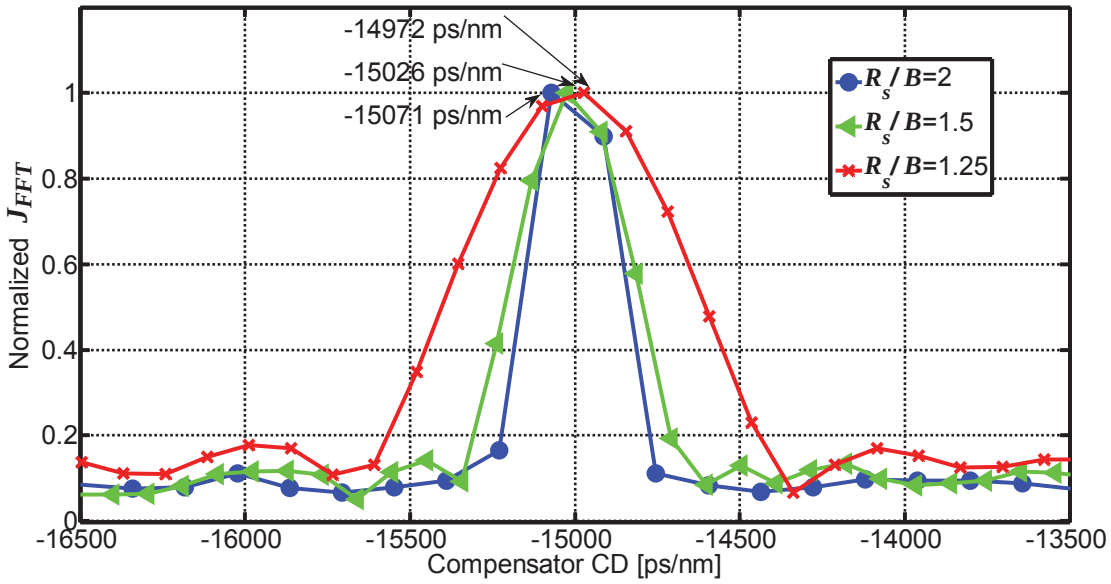

Figure 4.11: FFT mapping expression based initial search at different sampling rates around the fiber CD value of 15000 ps/nm as an example.

The first step CD search by employing (4.11) around fiber CD of 15000 ps/nm is shown in Figure 4.11 as an example for 112 Gb/s RZ-PDM-QPSK. The maxima occur

at -14972 ps/nm, -15026 ps/nm and -15071 ps/nm for 1.25, 1.5 and 2 samples per symbol, respectively with an apparent deviation in estimated CD values. It is can be observed that the width of the detected peak increases with reduction in the oversampling rate. Besides, it can also be observed that the sidelobes particularly increase at 1.25 samples per symbol. The autocorrelation function demonstrates sidelobes because of the non-optimum sample instances at low sampling rate. However, it does not lead to any estimation error because of the second step CD search. As shown in Figure 4.12, more precise CD estimates are obtained after second step optimized search.

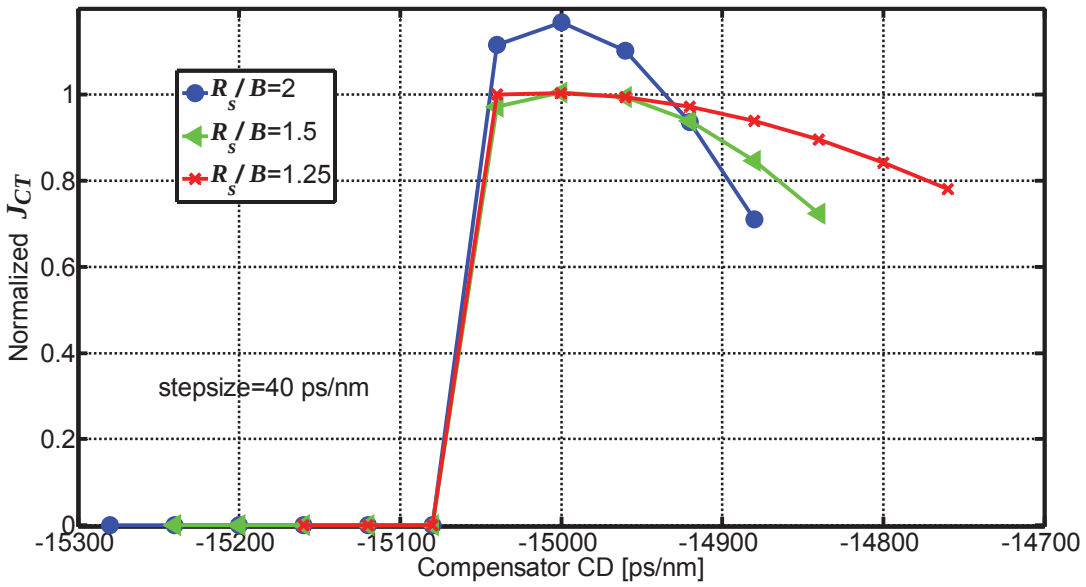

Figure 4.12: NT based optimized search at different sampling rates around the fiber CD value of 15000 ps/nm as an example. Vicinity is scanned in negative direction with 40 ps/nm resolution by varying the applied compensator CD.

Like last section, performance of the algorithm is further verified and analyzed by computing histograms of CD estimation error over 6000 random independent channels for each TX/RX scenario, at reduced ADC oversampling rates. The fiber CD is varied in the range of ±40000 ps/nm. Figure 4.13 (a) shows the CD estimation error histogram at 1.25, 1.5 and 2 samples per symbol for NRZ- and RZ-PDM-QPSK. Similarly, Figure 4.13 (b) shows the same for NRZ- and RZ-PDM-16-QAM. The algorithm is robust in all cases and the error is within ±50 ps/nm even

at reduced oversampling rates. Hence, the requirement for high sampling rate ADCs is lowered.

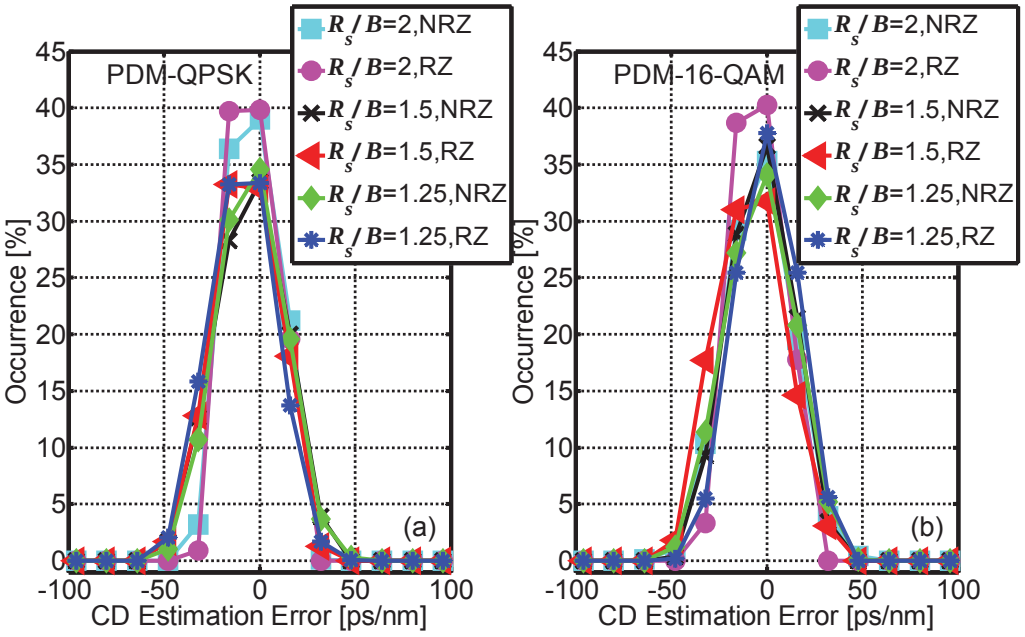

Figure 4.13: CD estimation error histogram at different sampling rates for (a) 112 Gb/s NRZ- and RZ-PDM-QPSK (b) 224 Gb/s NRZ- and RZ-PDM-16-QAM.

4.5 Discussion on Computational Effort and Performance

The proposed two-step FD CD estimation algorithm computes (4.6) only once. This is equivalent to one FFT operation of length N'. In this case, (4.6) requires

$$C_M = (N'/2)\log_2 N' \tag{4.13}$$

complex multiplications and

$$C_A = N'\log_2 N' \tag{4.14}$$

complex additions for the radix-2 algorithm. Furthermore, 11 FD filtering operations (in the worst case) are required in (4.5) at a stepsize of 40 ps/nm. This requires

$$C_M = 11N \tag{4.15}$$

complex multiplications and

$$C_A = 11(N-1) \tag{4.16}$$

complex additions. Therefore, for estimating CD in the range of ±40000 ps/nm as an example at $N = 1024$, 2304 complex multiplications and 4608 complex additions are required for computing (4.6). Moreover, 11264 complex multiplications and 11253 complex additions are required for computing (4.5). In comparison, the state-of-the-art [79-81] would require 401 filtering operations, i.e.

$$C_M = 401N \tag{4.17}$$

complex multiplications and

$$C_A = 401(N-1) \tag{4.18}$$

complex additions. to estimate CD in the range of ±40000 ps/nm, and that at a worse resolution of 200 ps/nm. So, in this case, 410624 complex multiplications and 410223 complex additions are required.

Therefore, the proposed two-step FD CD estimation algorithm is not only computationally efficient but it also enables CD estimation at much finer resolution.

Chapter 5

DSP based MIMO Equalization

This chapter presents digital MIMO equalization and its related algorithms. Section 5.1 explains the MIMO equalization technique for digital compensation of PMD and residual CD. The standard constant modulus algorithm (CMA) based MIMO equalization of QPSK signals is presented in section 5.2. Section 5.3 describes the CMA adaptation for the multi-level QAM signals. Partial update based efficient impulse response updating patterns are developed in section 5.4 for CMA-QAM based MIMO equalization. Section 5.5 presents the DD-LMS based equalization. The partial update DD-LMS based MIMO equalization is presented in section 5.6. Section 5.7 discusses the work, presented in this chapter, in terms of complexity and performance. Overall, this chapter presents the work on the development and optimization of efficient MIMO equalization schemes along with their performance analysis based on simulation results.

5.1 MIMO Equalization for PMD and Residual CD Compensation

PMD is the second main source of ISI, after CD, in the data that is received over high-speed long-haul transmission [88-93]. A two-stage equalization approach is needed for efficient compensation of these channel impairments in the digital domain. In the first stage, as seen in chapters 3 and 4, frequency domain equalization of CD with blind adaptation is a hardware-efficient solution for uncompensated links with large amount of CD. Furthermore, as the second stage, a 2x2, hence MIMO equalizer is required for residual CD and PMD compensation. It also performs the polarization demultiplexing. Unlike CD, which is a quasi-static fiber channel impairment (at least for non-dynamic/non-switching channels), the PMD changes are abrupt. Therefore, there is a

need for an adaptive MIMO structure based second stage PMD equalizer in the DSP enabled receiver. For performance analysis based on simulation results, the statistical channel model employed for the PMD effect is modelled in VPI TransmissionMaker™ [38].

Figure 5.1 depicts the 2x2 MIMO equalizer schematic. It employs four FIR filters $\mathbf{h}_{XX}$, $\mathbf{h}_{XY}$, $\mathbf{h}_{YX}$ and $\mathbf{h}_{YY}$. The impulse responses $\mathbf{h}_{XY}$ and $\mathbf{h}_{YX}$ represent the interference of two orthogonal polarizations with each other. Further details and algorithms for updating these four impulse responses of a digital MIMO equalizer are described in the following sections of this chapter.

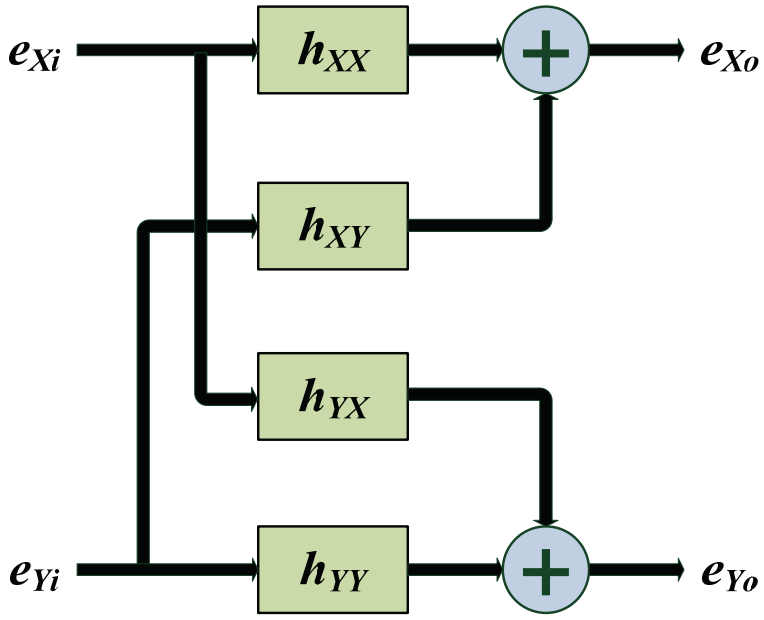

Figure 5.1: 2x2 MIMO equalizer schematic.

5.2 Standard CMA based MIMO Equalization for QPSK Signals

Standard CMA utilizes the constant modularity property of the signals. So, it treats any variations in signal amplitude as a distortion. Therefore, the algorithm tries to force the equalizer to follow a constant amplitude level and thus the equalizer converges. The CMA based equalizer adapts blindly, without the need of any training symbols. Therefore, the CMA based MIMO equalization can be applied for demultiplexing of

two orthogonal polarizations, PMD and residual CD compensation in PDM-QPSK systems [94-101].

The two outputs of the CMA based MIMO equalizer, by employing FIR filters $\mathbf{h}_{XX}$, $\mathbf{h}_{XY}$, $\mathbf{h}_{YX}$ and $\mathbf{h}_{YY}$ having length N_T, can be represented as,

$$e_{Xo}(k) = \mathbf{h}_{XX}{}^{T}\mathbf{e}_{Xi} + \mathbf{h}_{XY}{}^{T}\mathbf{e}_{Yi} \tag{5.1}$$

$$e_{Yo}(k) = \mathbf{h}_{YX}{}^{T}\mathbf{e}_{Xi} + \mathbf{h}_{YY}{}^{T}\mathbf{e}_{Yi} \tag{5.2}$$

where $\mathbf{e}_{Xi}$ and $\mathbf{e}_{Yi}$ are the equalizer input vectors of length N_T with respect to the reference sample (main sample) k for the X and Y polarizations, respectively and $e_{Xo}(k)$ and $e_{Yo}(k)$ represent the output signals at the reference sample k for the X and Y polarizations, respectively.

The standard CMA based MIMO equalizer employs a simple gradient search algorithm to minimize the cost functions [102-103],

$$\mathbf{h}_{XX}(k+1) = \mathbf{h}_{XX}(k) - \mu_g \nabla_{\mathbf{h}_{XX}}\left(J_{CMA,X}(k)\right) \tag{5.3}$$

$$\mathbf{h}_{XY}(k+1) = \mathbf{h}_{XY}(k) - \mu_g \nabla_{\mathbf{h}_{XY}}\left(J_{CMA,X}(k)\right) \tag{5.4}$$

$$\mathbf{h}_{YX}(k+1) = \mathbf{h}_{YX}(k) - \mu_g \nabla_{\mathbf{h}_{YX}}\left(J_{CMA,Y}(k)\right) \tag{5.5}$$

$$\mathbf{h}_{YY}(k+1) = \mathbf{h}_{YY}(k) - \mu_g \nabla_{\mathbf{h}_{YY}}\left(J_{CMA,Y}(k)\right) \tag{5.6}$$

where μ_g represents the MIMO equalizer update gain and $\nabla_{\mathbf{h}_{XX}}(.)$, $\nabla_{\mathbf{h}_{XY}}(.)$, $\nabla_{\mathbf{h}_{YX}}(.)$ and $\nabla_{\mathbf{h}_{YY}}(.)$ represent the gradient operators with respect to impulse responses $\mathbf{h}_{XX}$, $\mathbf{h}_{XY}$, $\mathbf{h}_{YX}$ and $\mathbf{h}_{YY}$ respectively. According to Widrow et al. [109], channel update equations can be derived by taking derivative of the cost functions with respect to impulse response vectors. This approach is adopted here to derive the update equations for MIMO equalizers that are considered and analyzed in this chapter. The cost functions of the standard CMA based MIMO equalizer are given as,

$$J_{CMA,X}(k) = \frac{1}{4}E\left\{\left(1 - \left|e_{Xo}(k)\right|^2\right)^2\right\} \tag{5.7}$$

$$J_{CMA,Y}(k) = \frac{1}{4} E\left\{\left(1 - \left|e_{Yo}(k)\right|^2\right)^2\right\} \tag{5.8}$$

for the X and Y polarizations, respectively. Here, $E\{.\}$ represents the expectation operator. Based on complex matrix calculus, the gradient operations in (5.3)-(5.6) are given as,

$$\nabla_{\mathbf{h}_{XX}}\left(J_{CMA,X}(k)\right) = -\left(1 - \left|e_{Xo}(k)\right|^2\right) e_{Xo}(k)\mathbf{e}^*_{Xi} \tag{5.9}$$

$$\nabla_{\mathbf{h}_{XY}}\left(J_{CMA,X}(k)\right) = -\left(1 - \left|e_{Xo}(k)\right|^2\right) e_{Xo}(k)\mathbf{e}^*_{Yi} \tag{5.10}$$

$$\nabla_{\mathbf{h}_{YX}}\left(J_{CMA,Y}(k)\right) = -\left(1 - \left|e_{Yo}(k)\right|^2\right) e_{Yo}(k)\mathbf{e}^*_{Xi} \tag{5.11}$$

$$\nabla_{\mathbf{h}_{YY}}\left(J_{CMA,Y}(k)\right) = -\left(1 - \left|e_{Yo}(k)\right|^2\right) e_{Yo}(k)\mathbf{e}^*_{Yi} \tag{5.12}$$

where * represents the complex conjugate operation. Henceforth, the update of four impulse responses for the CMA based MIMO equalizer can be represented as,

$$\mathbf{h}_{XX}(k+1) = \mathbf{h}_{XX}(k) + \mu_g D_X e_{Xo}(k)\mathbf{e}^*_{Xi} \tag{5.13}$$

$$\mathbf{h}_{XY}(k+1) = \mathbf{h}_{XY}(k) + \mu_g D_X e_{Xo}(k)\mathbf{e}^*_{Yi} \tag{5.14}$$

$$\mathbf{h}_{YX}(k+1) = \mathbf{h}_{YX}(k) + \mu_g D_Y e_{Yo}(k)\mathbf{e}^*_{Xi} \tag{5.15}$$

$$\mathbf{h}_{YY}(k+1) = \mathbf{h}_{YY}(k) + \mu_g D_Y e_{Yo}(k)\mathbf{e}^*_{Yi}\,. \tag{5.16}$$

The equations (5.13)-(5.16) aim at minimizing the power errors

$$D_X = 1 - \left|e_{Xo(}(k)\right|^2 \tag{5.17}$$

and

$$D_Y = 1 - \left|e_{Yo}(k)\right|^2 \tag{5.18}$$

with reference to a constant level (i.e. '1' in this case of QPSK modulation) in X and Y polarizations, respectively.

Once the taps of the MIMO equalizer have converged, the power differences (5.17)-(5.18) would tend to be zero. Figure 5.2 depicts the schematic of CMA based MIMO equalizer. As shown in this schematic, the output signals of FIR filters are used to compute the CMA based error signals. Then the impulse responses (5.13)-(5.16) are updated based on these CMA error signals, accordingly. Henceforth, the output signals of the FIR filters are subsequently fed to the carrier and data recovery block.

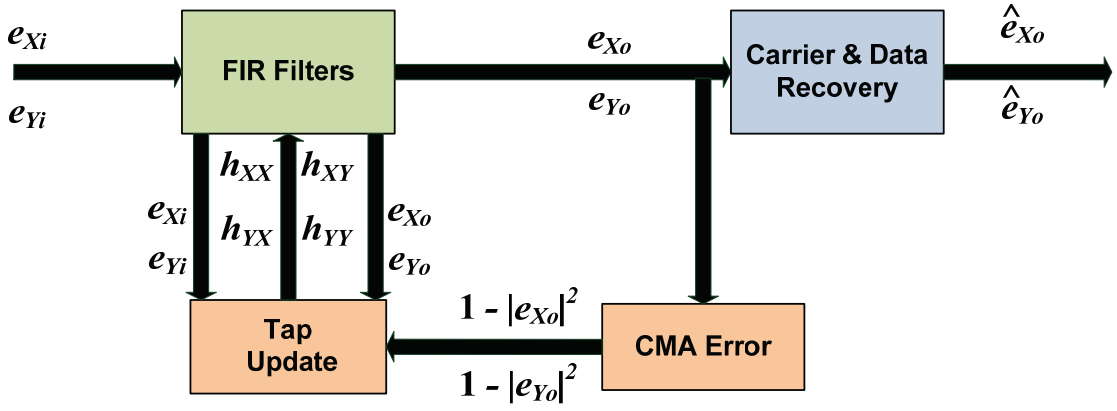

Figure 5.2: Schematic of the CMA based MIMO equalizer.

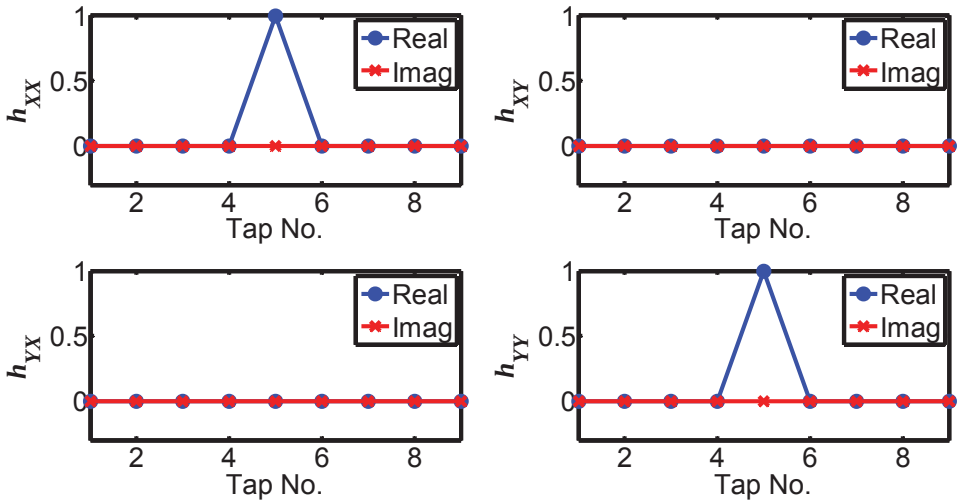

Figure 5.3: Initialized impulse responses of the standard CMA based MIMO equalizer.

The taps of the standard CMA based MIMO equalizer are initialized as shown in Figure 5.3. The impulse responses $\mathbf{h}_{XX}$ and $\mathbf{h}_{YY}$ are initialized by setting the center

taps to 1, while all other taps are set to zero. However, all the taps of impulse responses $\mathbf{h}_{XY}$ and $\mathbf{h}_{YX}$ are set to zero. After initialization of the taps, the equalizer converges using (5.13)-(5.16). Figure 5.4 shows the exemplary impulse responses of a converged 9-tap MIMO equalizer based on standard CMA for 112 Gb/s PDM-QPSK setup. It can be observed that the impulse responses $\mathbf{h}_{XX}$ and $\mathbf{h}_{YY}$ have higher power compared to $\mathbf{h}_{XY}$ and $\mathbf{h}_{YX}$.

The received constellation diagram for 112 Gb/s PDM-QPSK (without MIMO equalizer) is significantly distorted due to PMD present in the fiber, which results in ISI, as shown in Figure 5.5 (a). The ISI that is induced due to CD is removed at this stage by employing a frequency domain equalizer. The constellation diagram of the compensated QPSK data, by employing CMA based MIMO equalization, is shown in Figure 5.5 (b). The distortions are now removed by the MIMO equalizer.

After some introduction on standard CMA, the focus shall now be on efficient algorithms for MIMO equalization of even higher order QAM signals (such as 16-QAM) in the following sections of this chapter.

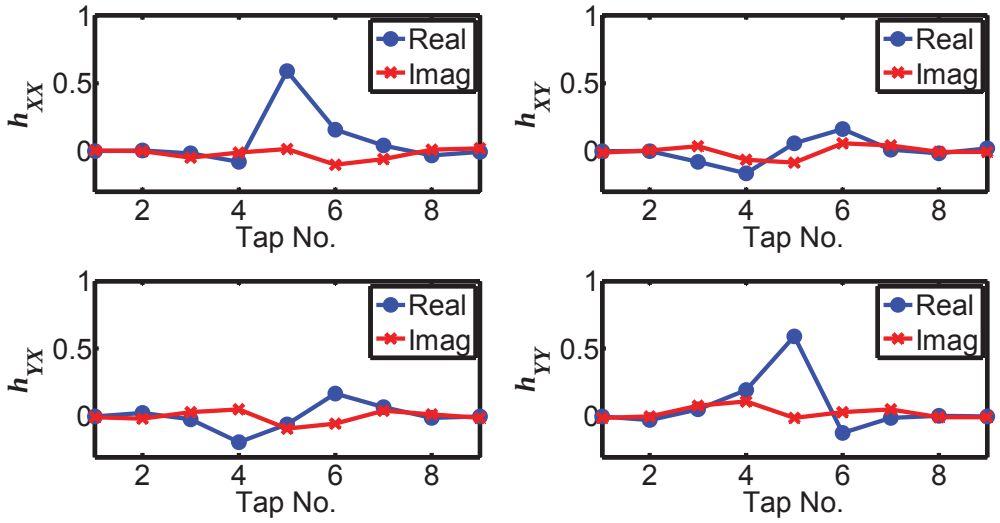

Figure 5.4: Converged impulse responses of the standard CMA based MIMO equalizer.

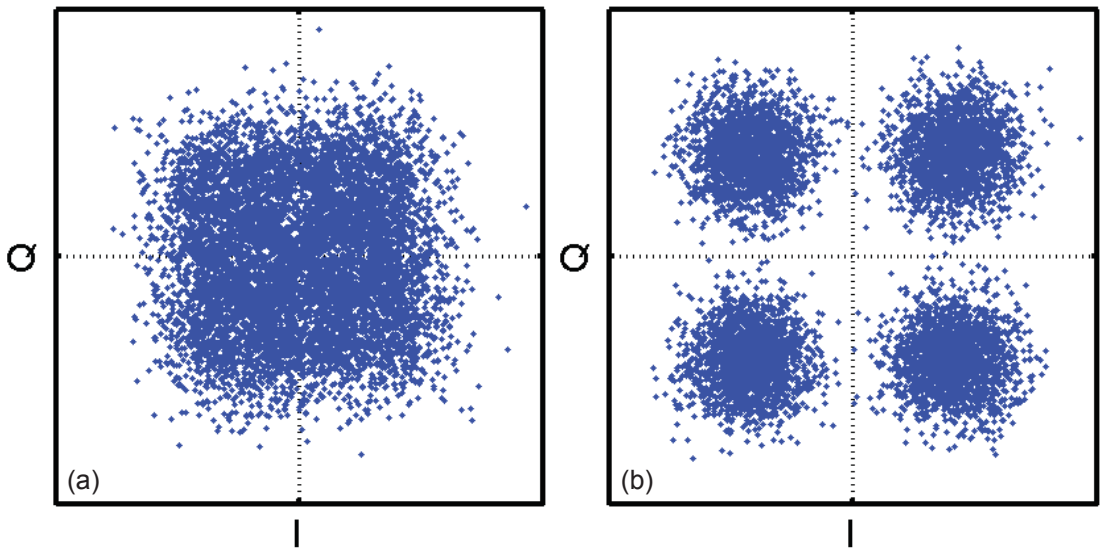

Figure 5.5: Received constellation diagram for QPSK (a) before CMA based MIMO equalizer (b) after CMA based MIMO equalizer.

5.3 CMA Adaptation for the MIMO Equalization of QAM Signals

The standard CMA based MIMO equalization, presented in section 5.2, could be applied on the PDM-16-QAM systems. However, in this case, the cost function error would never become zero, i.e. the steady-state of the MIMO equalizer would not be reached. As a consequence, a CMA-QAM based MIMO equalization is proposed as a QAM adaptation of the standard CMA based MIMO equalization technique. This is based on the earlier proposal of CMA-QAM for simple broadband polarization control [104]. The CMA-QAM equalizers are based on computing the cost function separately for the three power levels (rings) of the PDM-16-QAM signals. After initialization of the taps, the MIMO equalizer converges using same equations (5.13)-(5.16). However, in this case, the cost functions of the CMA-QAM based MIMO equalizer are represented as,

$$J_{CMA-QAM,X}(k) = \frac{1}{4}E\left\{\left(P_j - \left|e_{Xo}(k)\right|^2\right)^2\right\} \tag{5.19}$$

$$J_{CMA-QAM,Y}(k) = \frac{1}{4}E\left\{\left(P_j - \left|e_{Yo}(k)\right|^2\right)^2\right\} \tag{5.20}$$

for the X and Y polarizations, respectively. Therefore, in this case, the equations (5.13)-(5.16) would tend to minimize the power errors

$$D_X = \min(P_j - |e_{Xo}(k)|^2) \tag{5.21}$$

and

$$D_Y = \min(P_j - |e_{Yo}(k)|^2) \tag{5.22}$$

in X and Y polarizations, respectively. The term P_j represents all three possible power levels of the 16-QAM signal. These power levels can be regarded as three rings (at levels 2, 10 and 18) of the 16-QAM constellation diagram, where the index is $j \in \{1,2,3\}$. Once the algorithm has converged, all power differences would tend to be zero. Figure 5.6 shows the schematic of CMA-QAM based MIMO equalizer. In this case, the impulse responses (5.13)-(5.16) are updated based on the CMA-QAM error signals with reference to the three possible power levels of 16-QAM.

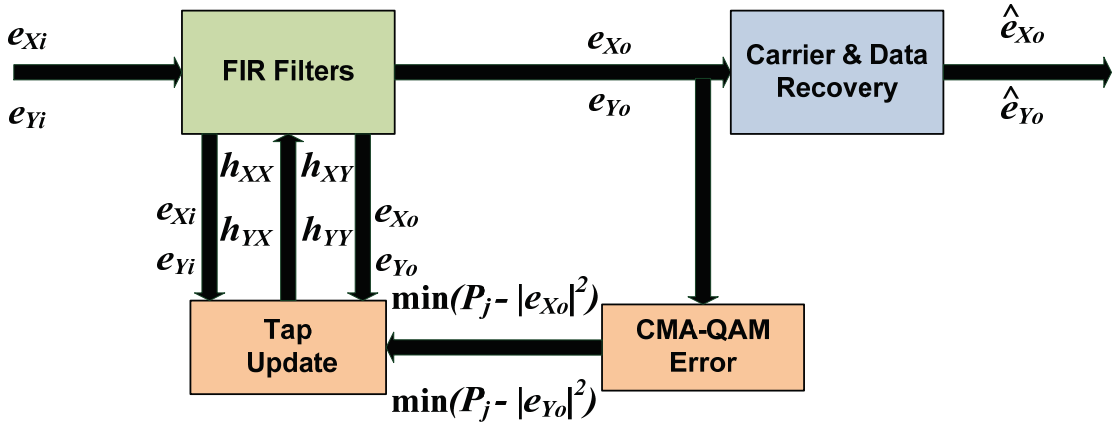

Figure 5.6: Schematic of the CMA-QAM based MIMO equalizer.

The taps of the CMA-QAM based MIMO equalizer are initialized as shown in Figure 5.7. As in section 5.2, the impulse responses $\mathbf{h}_{XX}$ and $\mathbf{h}_{YY}$ are initialized by setting the center taps to 1, while all other taps are set to zero. Figure 5.8 shows the exemplary impulse responses of a converged 9-tap MIMO equalizer based on CMA-QAM for a 224 Gb/s PDM-16-QAM setup.

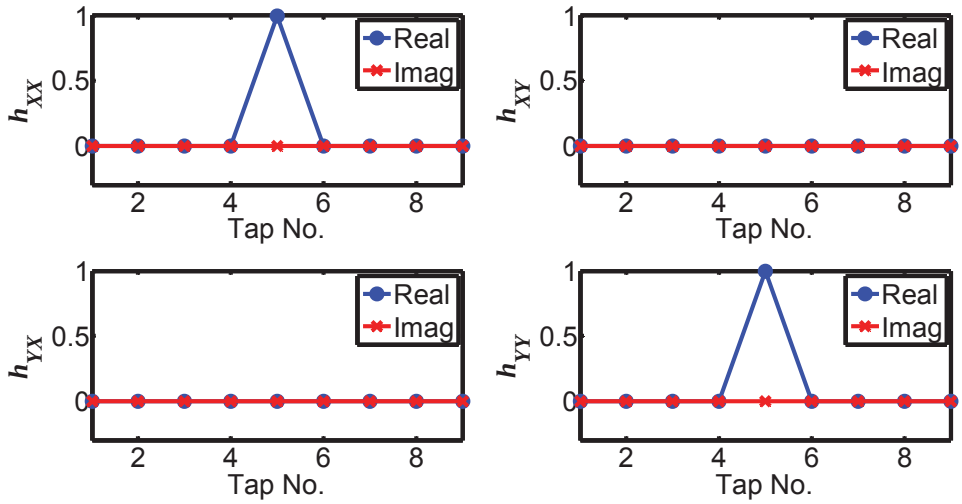

Figure 5.7: Initialized impulse responses of the CMA-QAM based MIMO equalizer.

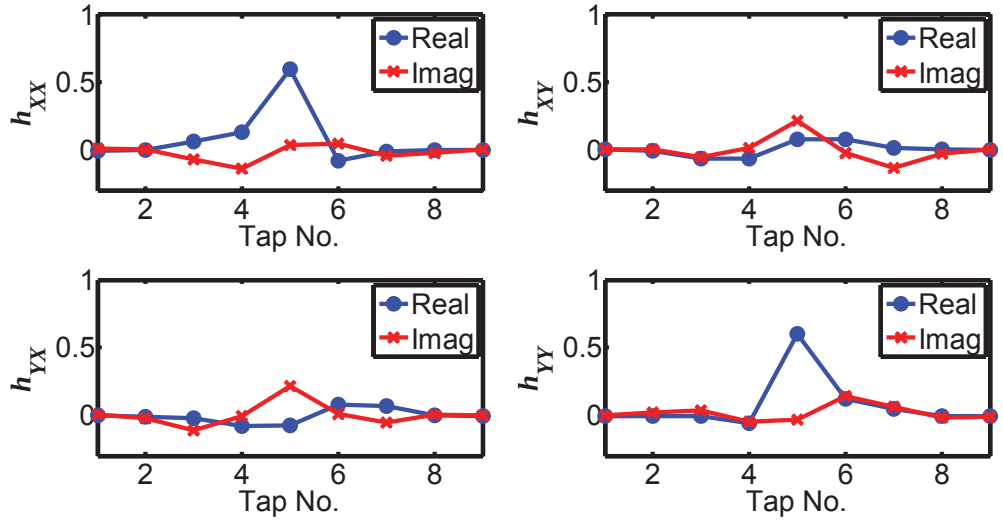

Figure 5.8: Converged impulse responses of the CMA-QAM based MIMO equalizer.

The constellation diagram for the received 224 Gb/s PDM-16-QAM data is shown in Figure 5.9 (a). It shows a lot of distortions due to PMD of the fiber. These distortion can be compensated by employing CMA-QAM based MIMO equalization as shown in Figure 5.9 (b). Note that this CMA-QAM based MIMO equalization may also be

applied easily to even higher order QAM signals. However, slightly more computations would be needed due to more number of power rings P_j.

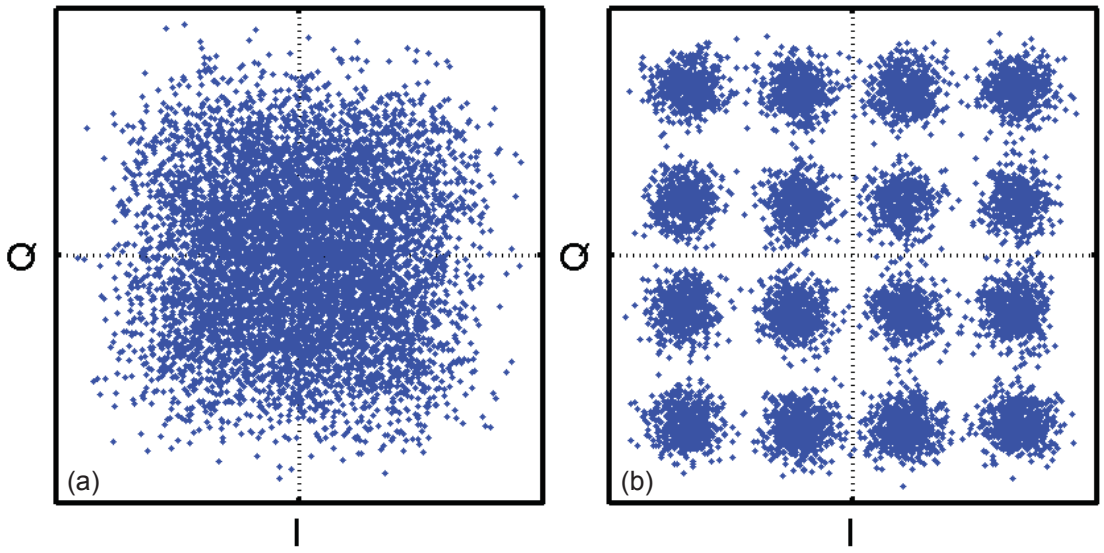

Figure 5.9: Received constellation diagram for 16-QAM (a) before CMA-QAM based MIMO equalizer (b) after CMA-QAM based MIMO equalizer.

A broader statistical basis is required for a detailed performance analysis of these MIMO equalizers, i.e. simulations over a large number of PMD scenarios must be performed. Consequently, the performance of the CMA-QAM based MIMO equalizer is further evaluated by computing histograms of the BER, for different equalizer update gains, based on 1000 PMD scenarios changing every 4096 symbols (iterations) at mean DGD value corresponding to half symbol duration i.e. <DGD>= 18 ps. In order to change the PMD scenario every 4096 symbols, two random number seeds controlling the fiber birefringence and polarization axis rotation are changed every 4096 symbols within the fiber model in VPI TransmissionMaker^{TM}. Therefore, the instantaneous DGD values change every 4096 symbols in this case. In order to obtain somewhat reasonable BER values (i.e. to avoid bad BER spikes), the BER counting starts after 1500 symbols in each scenario that changes after every 4096 symbols. For a reliable comparison, this same procedure will be considered for the performance analysis of all the algorithms considered in this chapter. Figure 5.10 shows the histograms for update gains of $5x10^{-4}$, 10^{-3}, $5x10^{-3}$ and 10^{-2}, respectively. It can be observed from these results that $5x10^{-3}$ is a suitable equalizer update gain for CMA-

QAM. Besides, 12000 ps/nm fiber CD and a laser sum-linewidth-times-symbol-duration product ($\Delta f T_S$) of 10^{-5} is considered for all simulations in this chapter.

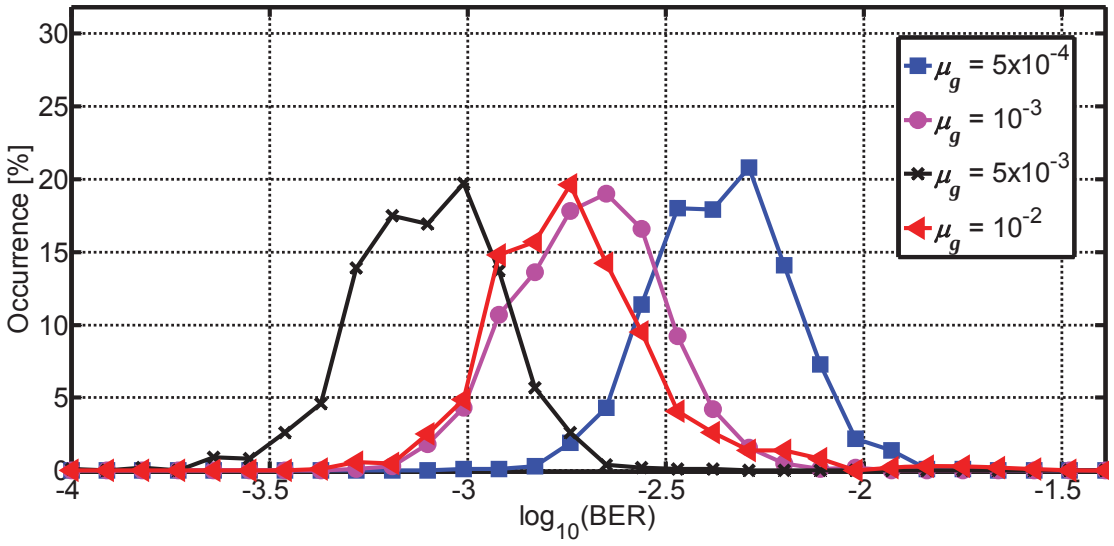

Figure 5.10: CMA-QAM based MIMO equalizer's BER performance for different update gains. Histograms are computed based on 1000 PMD scenarios changing every 4096 symbols at <DGD>= 18 ps.

Therefore, further performance analysis is done by computing histograms of the BER over 1000 PMD scenarios changing every 4096 and 8192 symbols at mean DGD values of 18 ps and 36 ps for an equalizer update gain of $5x10^{-3}$ (Figure 5.11). For the case when the PMD scenario changes every 8192 symbols, the BER counting starts after 4096 symbols. This shall really indicate the equalizer convergence improvement and consequently the BER improvement (if any) between the symbols 4097 to 8192. For a reliable comparison, this same procedure will also be considered for the performance analysis of all the algorithms considered in this chapter. It has been observed that higher BER values are observed when the PMD changes quickly, i.e. after every 4096 symbols, at large mean DGD value of 36 ps. This happens because the MIMO equalizer does not get to a proper steady state within this duration of 4096 symbols, for large instantaneous DGD values.

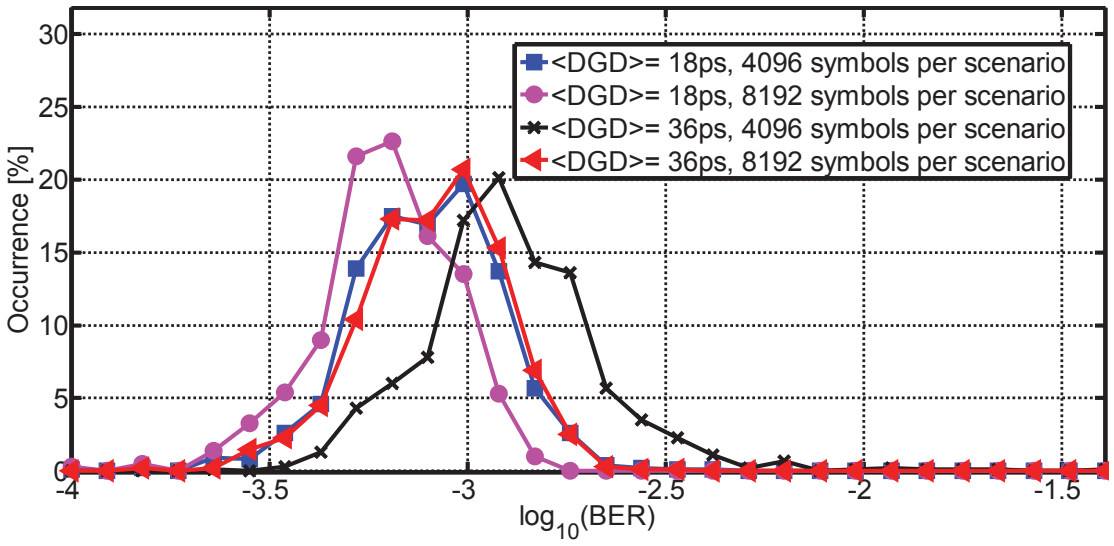

Figure 5.11: CMA-QAM based MIMO equalizer's BER performance for <DGD>= 18 ps and <DGD>= 36 ps. Histograms are computed based on 1000 PMD scenarios changing every 4096 and 8192 symbols.

5.4 PU-CMA-QAM based MIMO Equalization of QAM Signals

The partial update (PU) based adaptive filtering can reduce the complexity of MIMO equalization algorithms [105-108]. The main concept of the PU based MIMO equalization is to partially update the impulse responses of the MIMO equalizer rather than a full update. In this regard, a variety of patterns may be adapted to partially optimize each part of the impulse response. Updating a subset of the taps reduces the computational complexity. In this section, two different partial updating patterns employing CMA-QAM are presented along with their performance evaluation.

Consider a MIMO equalizer of length $N_T = PN_P$, i.e. $k \in \{0,1,..., N_T - 1\}$ is divided into P parts of length N_P. The PU-CMA-QAM algorithm updates the subsets of the impulse responses of FIR filters (5.13)-(5.16) given by the indices,

$$SS_p \in \{pN_P, pN_P + 1,..., pN_P + N_P - 1\} \tag{5.23}$$

where integer $p \in \{0,1,..., P - 1\}$ refers to the different parts or subsets of the impulse responses in this case. So, all the coefficients are not updated at a time because all

updates are not computed at that time. In this respect, PU-CMA-QAM (Pattern 1) updates the impulse responses in sequential order such that each part *P* is updated at the same frequency. Whereas, PU-CMA-QAM (Pattern 2) updates the central part $(\sim\lceil P/2\rceil-1)$ of the impulse responses *Q* times more frequently.

So, considering the case of a 9-tap MIMO equalizer, employed in this chapter, which is divided in to three subsets *P*=3 of length N_P =3. Consequently, the PU-CMA-QAM (Pattern 1) updates the three subsets consisting of impulse response indices $SS_0 \in \{0,1,2\}$, $SS_1 \in \{3,4,,5\}$ and $SS_2 \in \{6,7,8\}$ in sequential order (i.e. $SS_0, SS_1, SS_2, SS_0, SS_1, SS_2, \ldots$). In case of PU-CMA-QAM (Pattern 2), for the considered 9-tap equalizer, $Q = 5$ is found to be a suitable value. Therefore, the PU-CMA-QAM (Pattern 2) updates the central subset of the impulse responses 5 times more frequently than the other two subsets of the impulse responses (i.e. $SS_0, SS_1, SS_1, SS_1, SS_1, SS_1, SS_2, SS_0, SS_1, SS_1, SS_1, SS_1, SS_1, SS_2, \ldots$).

Figure 5.12 shows the schematic of PU-CMA-QAM based MIMO equalizer. It is clear that the PU-CMA-QAM based MIMO equalization algorithms reduce the complexity by a factor of *P*, compared to the full update CMA-QAM based MIMO equalization algorithms. It can be seen that the update block will updates only a subset of indices.

Like last section, the performance of the PU-CMA-QAM (Pattern 1) based MIMO equalizer is further evaluated by computing histograms of the BER, for different equalizer update gains, based on 1000 PMD scenarios changing every 4096 symbols at <DGD>= 18 ps. Figure 5.13 shows the BER histograms for equalizer update gains of $5\text{x}10^{-4}$, 10^{-3}, $5\text{x}10^{-3}$ and 10^{-2}, respectively. It can be observed from these results that $5\text{x}10^{-3}$ performs best amongst the considered equalizer update gain for PU-CMA-QAM. Furthermore, the performance of the PU-CMA-QAM (Pattern 1) based MIMO equalizer is now analyzed by computing histograms of the BER over 1000 PMD scenarios changing every 4096 and 8192 symbols at mean DGD values of 18 ps and 36 ps for an update gain of $5\text{x}10^{-3}$ (Figure 5.14). It can be observed from Figures 5.13 and 5.14 that there is a slight performance degradation as compared to the full update CMA-QAM based MIMO equalizer.

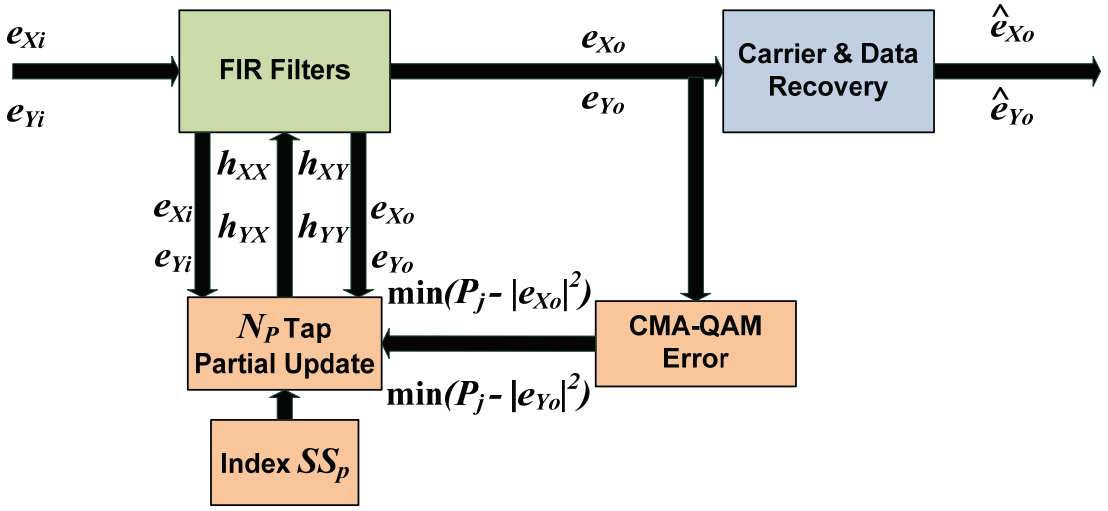

Figure 5.12: Schematic of the PU-CMA-QAM based MIMO equalizer.

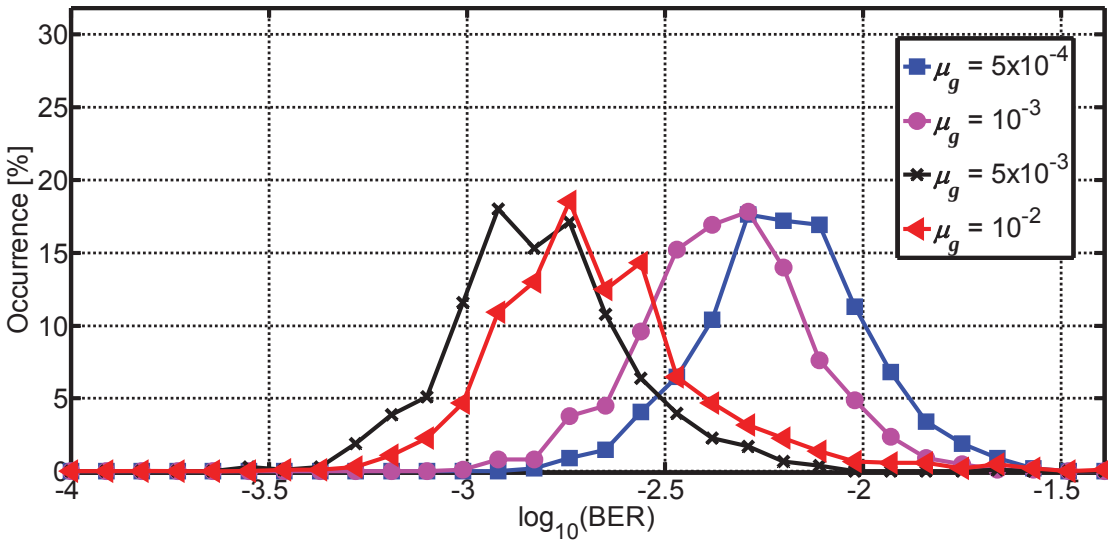

Figure 5.13: PU-CMA-QAM (Pattern 1) based MIMO equalizer's BER performance for different update gains. Histograms are computed based on 1000 PMD scenarios changing every 4096 symbols at <DGD>= 18 ps.

After PU-CMA-QAM (Pattern 1), now the performance of the PU-CMA-QAM (Pattern 2) based MIMO equalizer is evaluated by computing histograms of the BER, for equalizer update gains of $5\text{x}10^{-4}$, 10^{-3}, $5\text{x}10^{-3}$ and 10^{-2}, based on 1000 PMD scenarios changing every 4096 symbols at <DGD>= 18 ps. These BER histograms are depicted in Figure 5.15.

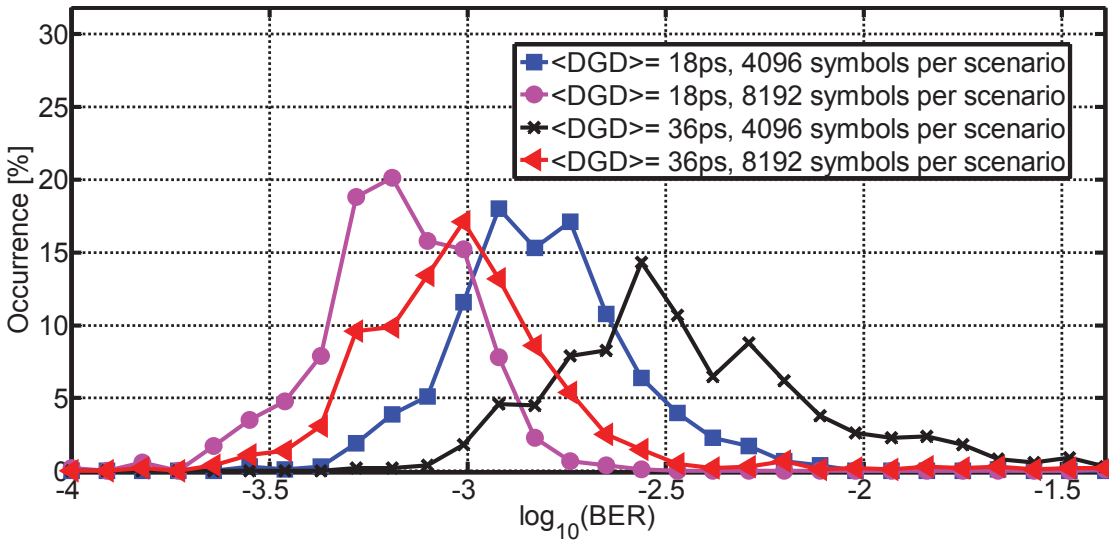

Figure 5.14: PU-CMA-QAM (Pattern 1) based MIMO equalizer's BER performance for <DGD>= 18 ps and <DGD>= 36 ps. Histograms are computed based on 1000 PMD scenarios changing every 4096 and 8192 symbols.

Furthermore, histograms of the BER are computed over 1000 PMD scenarios changing every 4096 and 8192 symbols at mean DGD values of 18 ps and 36 ps for an update gain of $5x10^{-3}$ (Figure 5.16). It can be observed that compared to PU-CMA-QAM (Pattern 1) represented with dashed lines, lower BER values are obtained for PU-CMA-QAM (Pattern 2). Besides, the performance of the PU-CMA-QAM (Pattern 2) based MIMO equalizer closely matches to that of full update CMA-QAM based MIMO equalizer.

Therefore, the PU-CMA-QAM (Pattern 2) based MIMO equalizer comes out to be an optimal equalization technique in terms of low complexity and high convergence speed compared to the one based on PU-CMA-QAM (Pattern 1). Furthermore, it has also been proved that the proposed PU based MIMO equalization algorithms are also robust against any residual CD (due to blind CD estimation).

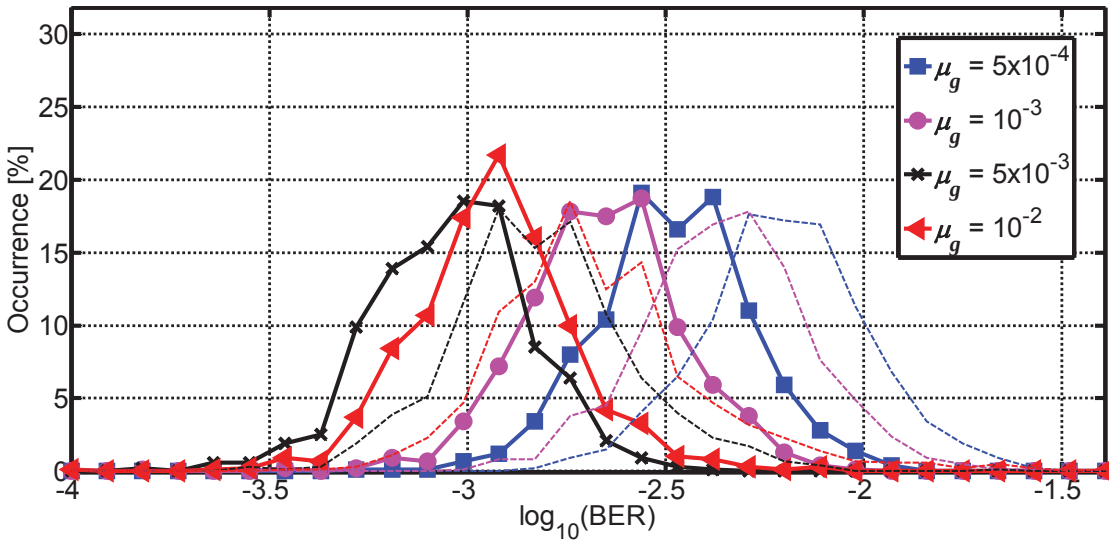

Figure 5.15: PU-CMA-QAM (Pattern 2) based MIMO equalizer's BER performance for different update gains. Histograms are computed based on 1000 PMD scenarios changing every 4096 symbols at <DGD>= 18 ps. For comparison, dashed lines depict the corresponding results with PU-CMA-QAM (Pattern 1).

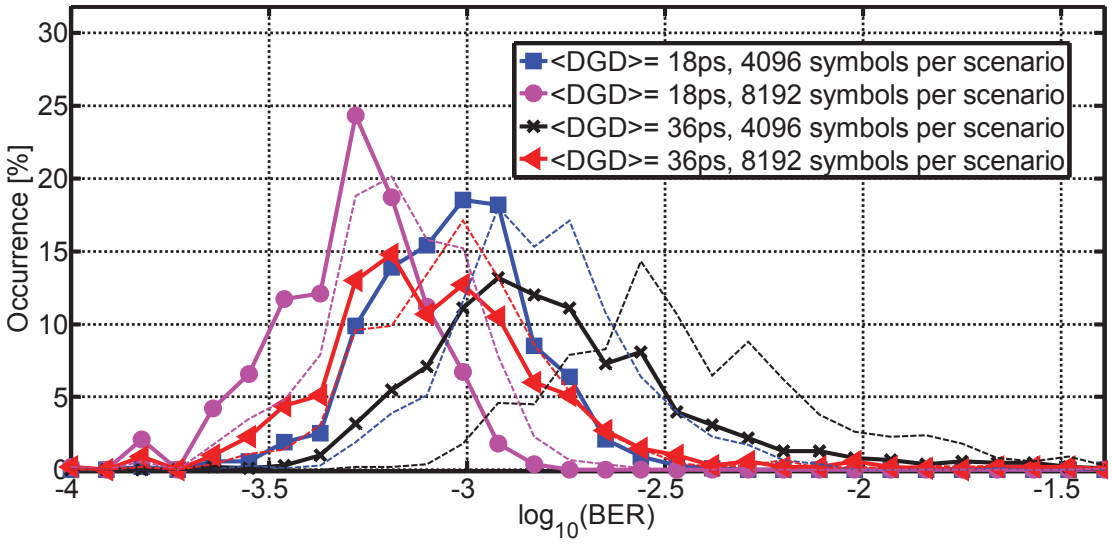

Figure 5.16: PU-CMA-QAM (Pattern 2) based MIMO equalizer's BER performance for <DGD>= 18 ps and <DGD>= 36 ps. Histograms are computed based on 1000 PMD scenarios changing every 4096 and 8192 symbols. For comparison, dashed lines depict the corresponding results with PU-CMA-QAM (Pattern 1).

5.5 DD-LMS based MIMO Equalization of QAM Signals

The decision directed least mean square (DD-LMS) algorithm based MIMO equalization employs the complex-amplitude error between symbol decisions at the output and incoming reference signal to the equalizer [109-113]. It is easily applicable to the 16-QAM signals or even further higher order QAM. The DD-LMS based equalizer adapts blindly, without the need of any training symbols. The DD-LMS based MIMO equalizer employs a simple gradient search algorithm to minimize the cost functions [109],

$$\mathbf{h}_{XX}(k+1) = \mathbf{h}_{XX}(k) - \mu_g \nabla_{\mathbf{h}_{XX}} \left(J_{DD-LMS,X}(k) \right) \tag{5.24}$$

$$\mathbf{h}_{XY}(k+1) = \mathbf{h}_{XY}(k) - \mu_g \nabla_{\mathbf{h}_{XY}} \left(J_{DD-LMS,X}(k) \right) \tag{5.25}$$

$$\mathbf{h}_{YX}(k+1) = \mathbf{h}_{YX}(k) - \mu_g \nabla_{\mathbf{h}_{YX}} \left(J_{DD-LMS,Y}(k) \right) \tag{5.26}$$

$$\mathbf{h}_{YY}(k+1) = \mathbf{h}_{YY}(k) - \mu_g \nabla_{\mathbf{h}_{YY}} \left(J_{DD-LMS,Y}(k) \right). \tag{5.27}$$

Whereas, the cost functions of the DD-LMS based MIMO equalizer can be represented as,

$$J_{DD-LMS,X}(k) = \frac{1}{2} E\left\{ \left| \hat{e}_{Xo}(k) - e_{Xo,r}(k) \right|^2 \right\} \tag{5.28}$$

$$J_{DD-LMS,Y}(k) = \frac{1}{2} E\left\{ \left| \hat{e}_{Yo}(k) - e_{Yo,r}(k) \right|^2 \right\} \tag{5.29}$$

for the X and Y polarizations, respectively. Here, $\hat{e}_{Xo}(k)$ and $\hat{e}_{Yo}(k)$ represent the symbol decisions at the reference sample (main sample) k, in X and Y polarizations, respectively. $e_{Xo,r}(k)$ and $e_{Yo,r}(k)$ represent the output signals after carrier phase estimation and back rotation for the X and Y polarizations, respectively. Based on complex matrix calculus, the gradient operations in (5.24)-(5.27) are expressed as,

$$\nabla_{\mathbf{h}_{XX}} \left(J_{DD-LMS,X}(k) \right) = -\left(\hat{e}_{Xo}(k) - e_{Xo,r}(k) \right) \mathbf{e}_{Xi}^{*} \tag{5.30}$$

$$\nabla_{\mathbf{h}_{XY}} \left(J_{DD-LMS,X}(k) \right) = -\left(\hat{e}_{Xo}(k) - e_{Xo,r}(k) \right) \mathbf{e}_{Yi}^{*} \tag{5.31}$$

$$\nabla_{\mathbf{h}_{YX}}\left(J_{DD-LMS,Y}(k)\right) = -\left(\hat{e}_{Yo}(k) - e_{Yo,r}(k)\right)\mathbf{e}_{Xi}^{*} \tag{5.32}$$

$$\nabla_{\mathbf{h}_{YY}}\left(J_{DD-LMS,Y}(k)\right) = -\left(\hat{e}_{Yo}(k) - e_{Yo,r}(k)\right)\mathbf{e}_{Yi}^{*}. \tag{5.33}$$

Here, $\mathbf{e}_{Xi}$ and $\mathbf{e}_{Yi}$ are the equalizer input vectors of length N_T with respect to reference sample *k* for the X and Y polarizations, respectively. Therefore, the four FIR filters $\mathbf{h}_{XX}$, $\mathbf{h}_{XY}$, $\mathbf{h}_{YX}$ and $\mathbf{h}_{YY}$ of the DD-LMS based MIMO equalizer can be represented as,

$$\mathbf{h}_{XX}(k+1) = \mathbf{h}_{XX}(k) + \mu_g D_X \mathbf{e}_{Xi}^{*} \tag{5.34}$$

$$\mathbf{h}_{XY}(k+1) = \mathbf{h}_{XY}(k) + \mu_g D_X \mathbf{e}_{Yi}^{*} \tag{5.35}$$

$$\mathbf{h}_{YX}(k+1) = \mathbf{h}_{YX}(k) + \mu_g D_Y \mathbf{e}_{Xi}^{*} \tag{5.36}$$

$$\mathbf{h}_{YY}(k+1) = \mathbf{h}_{YY}(k) + \mu_g D_Y \mathbf{e}_{Yi}^{*} \tag{5.37}$$

where, the update equations (5.34)-(5.37) aim at minimizing the complex error signals with respect to symbol decisions, i.e.

$$D_X = \hat{e}_{Xo}(k) - e_{Xo,r}(k) \tag{5.38}$$

and

$$D_Y = \hat{e}_{Yo}(k) - e_{Yo,r}(k) \tag{5.39}$$

in X and Y polarizations, respectively.

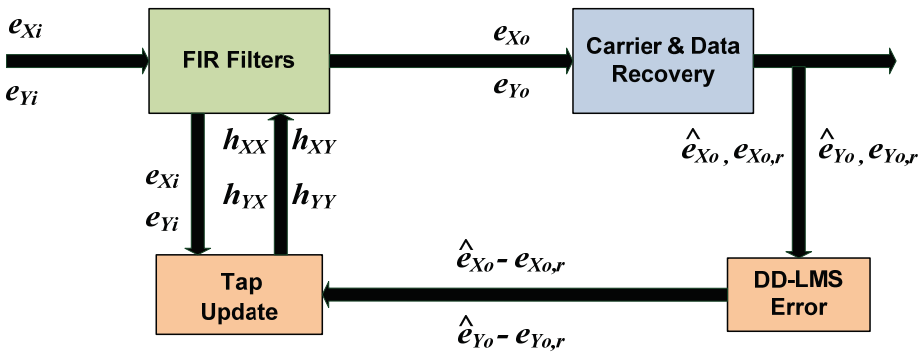

Figure 5.17: Schematic of the DD-LMS based MIMO equalizer.

One particular issue, in DD-LMS based MIMO equalizers, is the availability of symbol decisions based on feedforward carrier recovery. So, a feedback for the symbol decisions is required. Figure 5.17 depicts the schematic of DD-LMS based MIMO equalizer. As shown in this schematic, the output signals of the carrier and data recovery module are used to compute the DD-LMS based error signals. Then the impulse responses (5.34)-(5.37) are updated based on these complex error signals, accordingly.

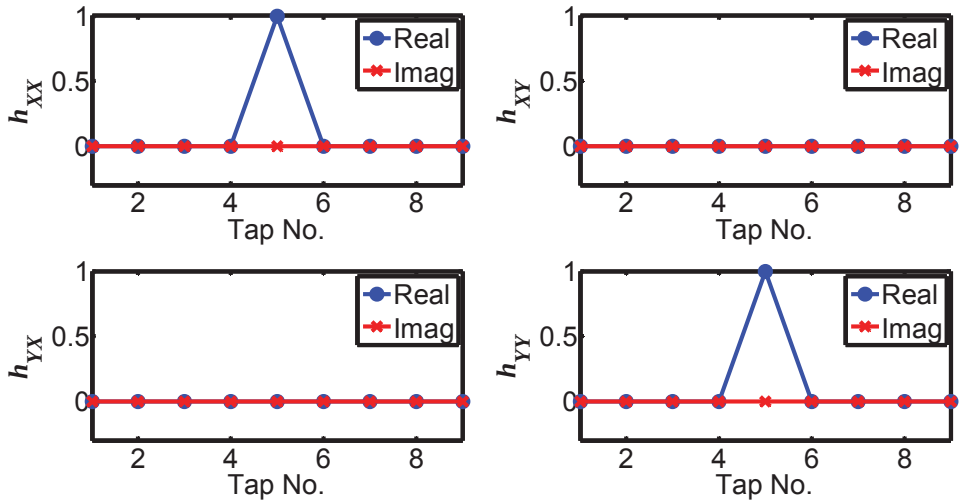

Figure 5.18: Initialized impulse responses of the DD-LMS based MIMO equalizer.

The taps of the DD-LMS based MIMO equalizer are initialized as shown in Figure 5.18. Impulse responses $\mathbf{h}_{XX}$ and $\mathbf{h}_{YY}$ are initialized by setting the center taps to 1, while all other taps are set to zero. Figure 5.19 shows the exemplary impulse responses of a converged 9-tap MIMO equalizer based on DD-LMS for a 224 Gb/s PDM-16-QAM setup.

Furthermore, the constellation diagram for the received 224 Gb/s PDM-16-QAM data is shown in Figure 5.20 (a). Whereas, Figure 5.20 (b) shows the data compensated by employing DD-LMS based MIMO equalization.

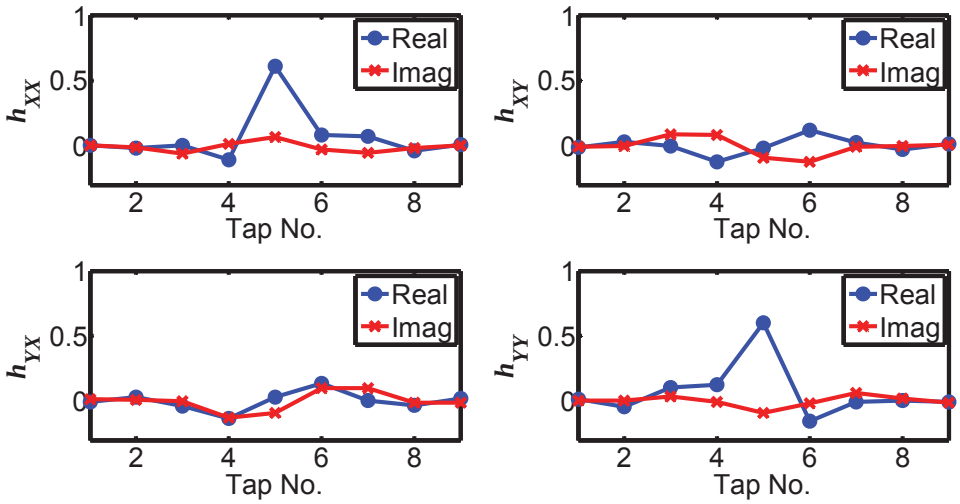

Figure 5.19: Converged impulse responses of the DD-LMS based MIMO equalizer.

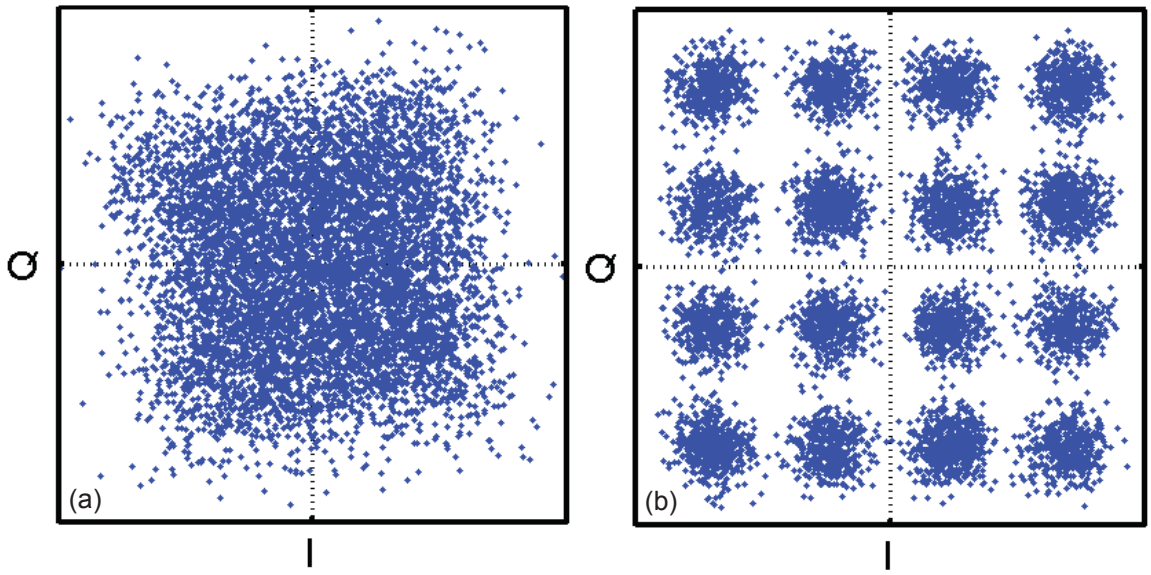

Figure 5.20: Received constellation diagram for 16-QAM (a) before DD-LMS based MIMO equalizer (b) after DD-LMS based MIMO equalizer.

DD-LMS based MIMO equalizer's performance is analyzed by computing histograms of the BER, for update gains of 5×10^{-4}, 10^{-3}, 5×10^{-3} and 10^{-2}, based on 1000 PMD scenarios changing every 4096 symbols at <DGD>= 18 ps as shown in Figure 5.21.

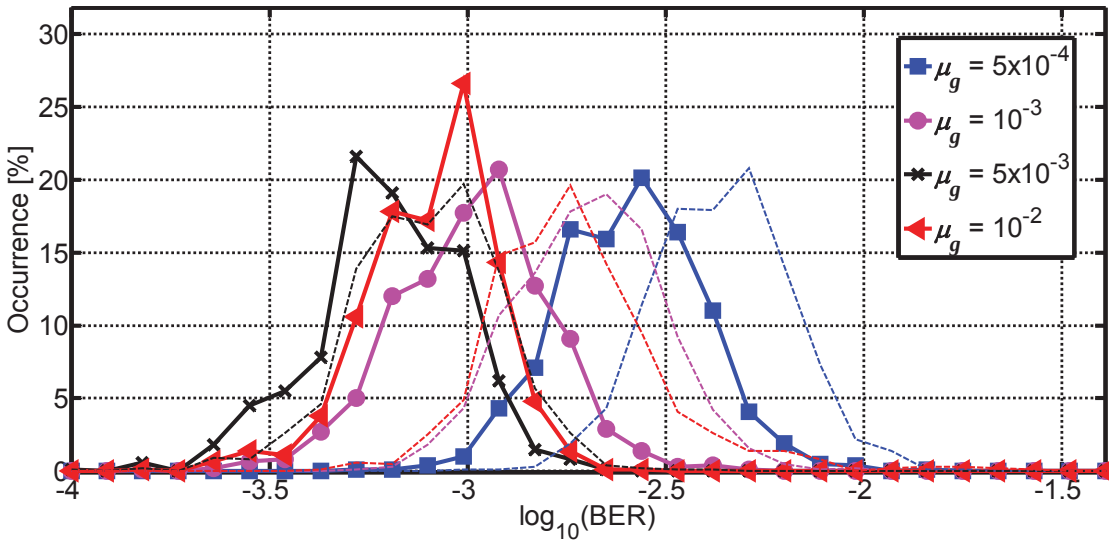

Figure 5.21: DD-LMS based MIMO equalizer's BER performance for different update gains. Histograms are computed based on 1000 PMD scenarios changing every 4096 symbols at <DGD>= 18 ps. For comparison, dashed lines depict the corresponding results with CMA-QAM.

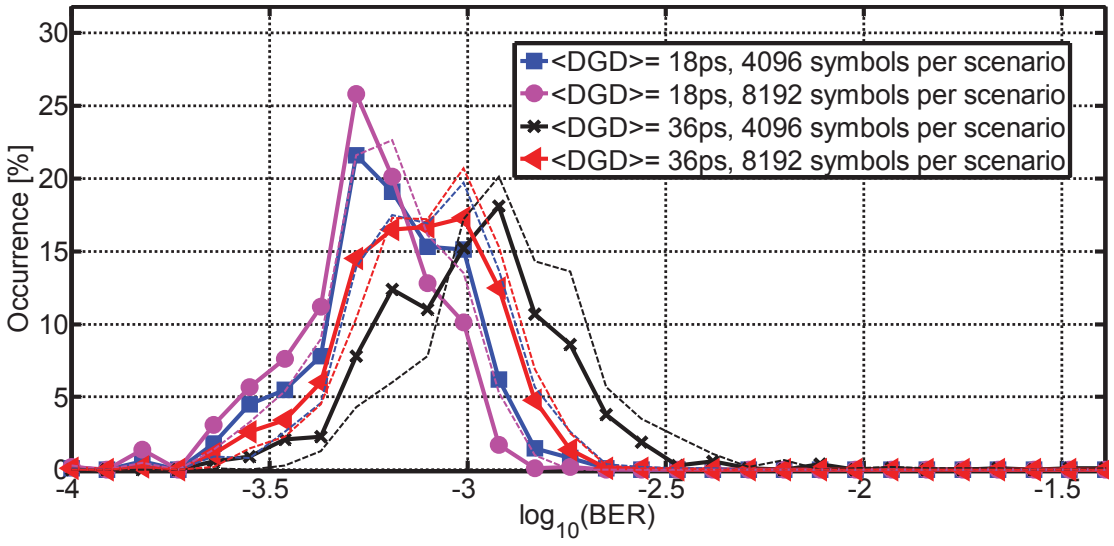

Figure 5.22: DD-LMS based MIMO equalizer's BER performance for <DGD>= 18 ps and <DGD>= 36 ps. Histograms are computed based on 1000 PMD scenarios changing every 4096 and 8192 symbols. For comparison, dashed lines depict the corresponding results with CMA-QAM.

Furthermore, histograms of the BER are computed over 1000 PMD scenarios changing every 4096 and 8192 symbols at mean DGD values of 18 ps and 36 ps for an update gain of $5x10^{-3}$ (Figure 5.22). It is observed that lower BER values are obtained for DD-LMS compared to CMA-QAM (dashed lines). Hence, it is clear from Figures 5.21 and 5.22 that DD-LMS based MIMO equalizer performs better than the CMA-QAM based MIMO equalizer.

5.6 PU-DD-LMS based MIMO Equalization of QAM Signals

As seen in section 5.4, updating a subset of the taps reduces the computational complexity of MIMO equalizer. In this section, the two effective partial updating patterns presented in section 5.4 are employed on DD-LMS for MIMO equalization. Figure 5.23 depicts the schematic of the PU-DD-LMS based MIMO equalizer.

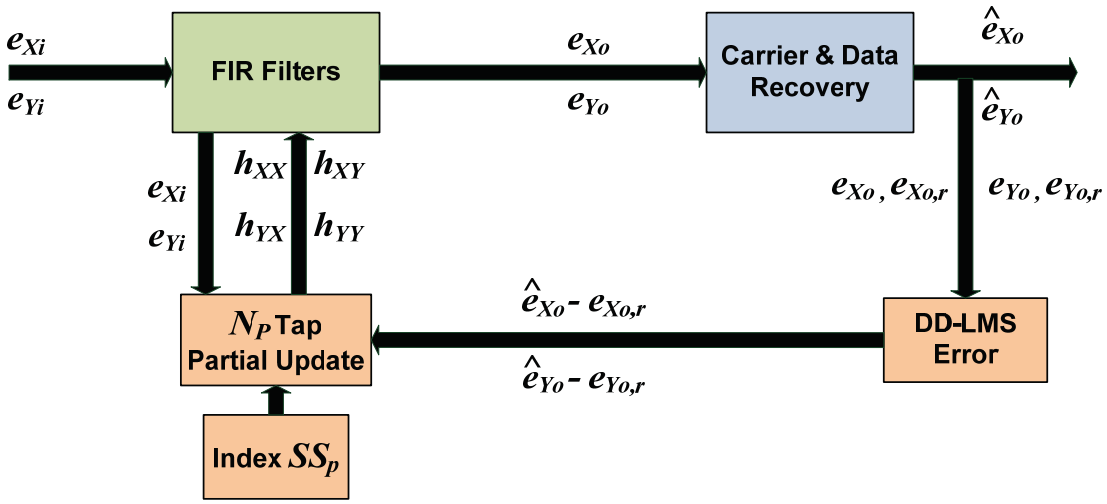

Figure 5.23: Schematic of the PU-DD-LMS algorithm based MIMO equalizer.

Like last sections, the performance of the DD-LMS (Pattern 1) based MIMO equalizer is evaluated by computing histograms of the BER, for update gains of $5x10^{-4}$, 10^{-3}, $5x10^{-3}$ and 10^{-2}, based on 1000 PMD scenarios changing every 4096 symbols at <DGD>= 18 ps (Figure 5.24). Besides, histograms of the BER are computed over 1000 PMD scenarios changing every 4096 and 8192 symbols at mean DGD values of 18 ps and 36 ps for an update gain of $5x10^{-3}$ (Figure 5.25). As observed from Figures 5.24

and 5.25, there is a slight performance degradation as compared to the full update DD-LMS based MIMO equalizer.

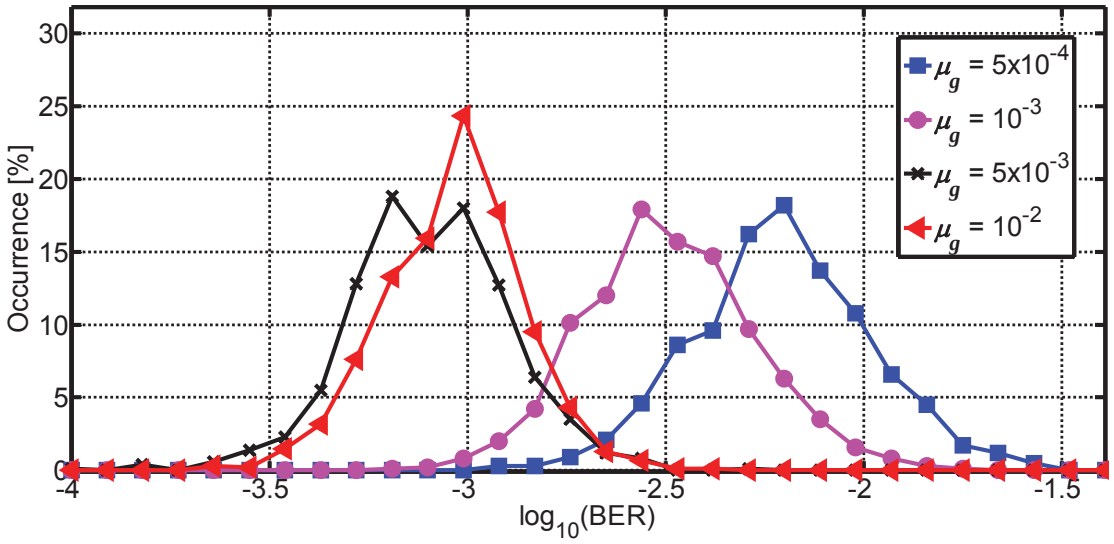

Figure 5.24: PU-DD-LMS (Pattern 1) based MIMO equalizer's BER performance for different update gains. Histograms are computed based on 1000 PMD scenarios changing every 4096 symbols at <DGD>= 18 ps.

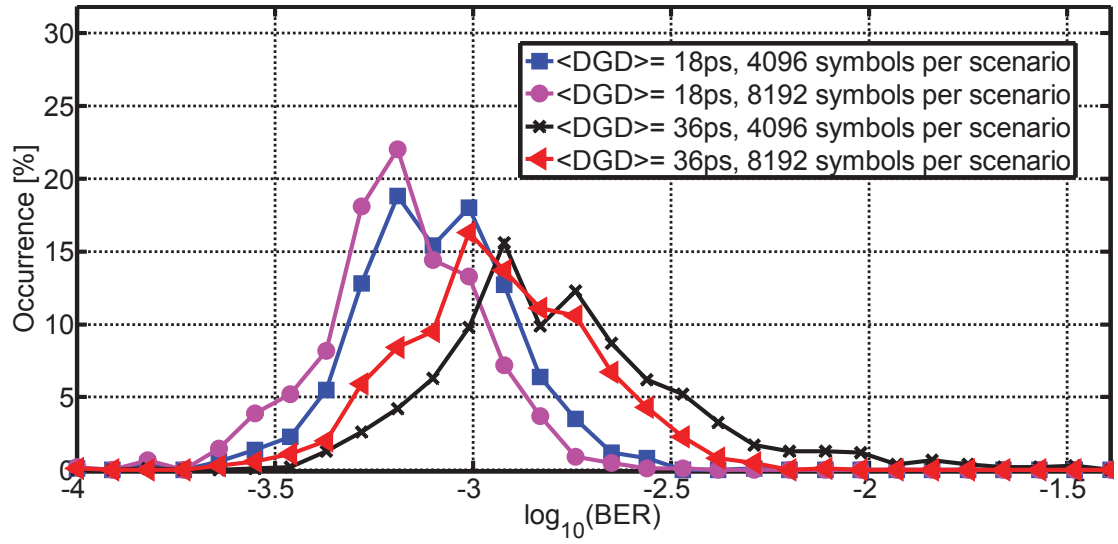

Figure 5.25: PU-DD-LMS (Pattern 1) based MIMO equalizer's BER performance for <DGD>= 18 ps and <DGD>= 36 ps. Histograms are computed based on 1000 PMD scenarios changing every 4096 and 8192 symbols.

Performance of the PU-DD-LMS (Pattern 2) based MIMO equalizer is evaluated by computing histograms of the BER, for update gains of $5x10^{-4}$, 10^{-3}, $5x10^{-3}$ and 10^{-2}, based on 1000 PMD scenarios changing every 4096 symbols at <DGD>= 18 ps (Figure 5.26). Besides, histograms of the BER are computed over 1000 PMD scenarios changing every 4096 and 8192 symbols at mean DGD values of 18 ps and 36 ps for an update gain of $5x10^{-3}$ as shown in Figure 5.27. Compared to PU-DD-LMS (Pattern 1) represented with dashed lines, lower BER values are obtained for PU-DD-LMS (Pattern 2). Furthermore, the performance of the PU-DD-LMS (Pattern 2) based MIMO equalizer closely matches to that of full update DD-LMS based MIMO equalizer.

Therefore, the PU-DD-LMS (Pattern 2) based MIMO equalizer comes out to be an optimal equalization technique in terms of low complexity and high convergence speed compared to the PU-DD-LMS (Pattern 1) and PU-CMA-QAM (Pattern 2) based MIMO equalizers.

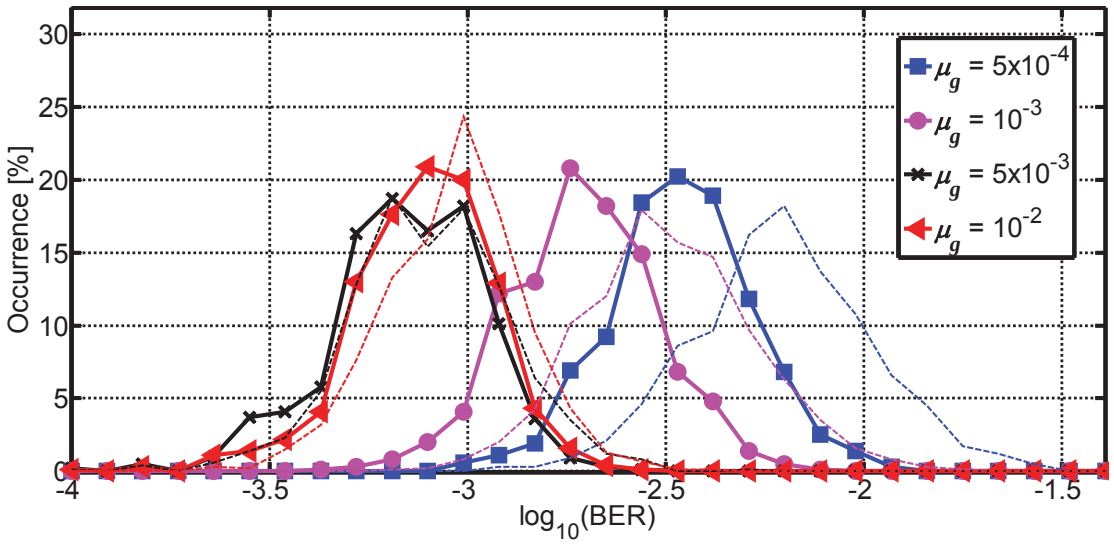

Figure 5.26: PU-DD-LMS (Pattern 2) based MIMO equalizer's BER performance for different update gains. Histograms are computed based on 1000 PMD scenarios changing every 4096 symbols at <DGD>= 18 ps. For comparison, dashed lines depict the corresponding results with PU-DD-LMS (Pattern 1).

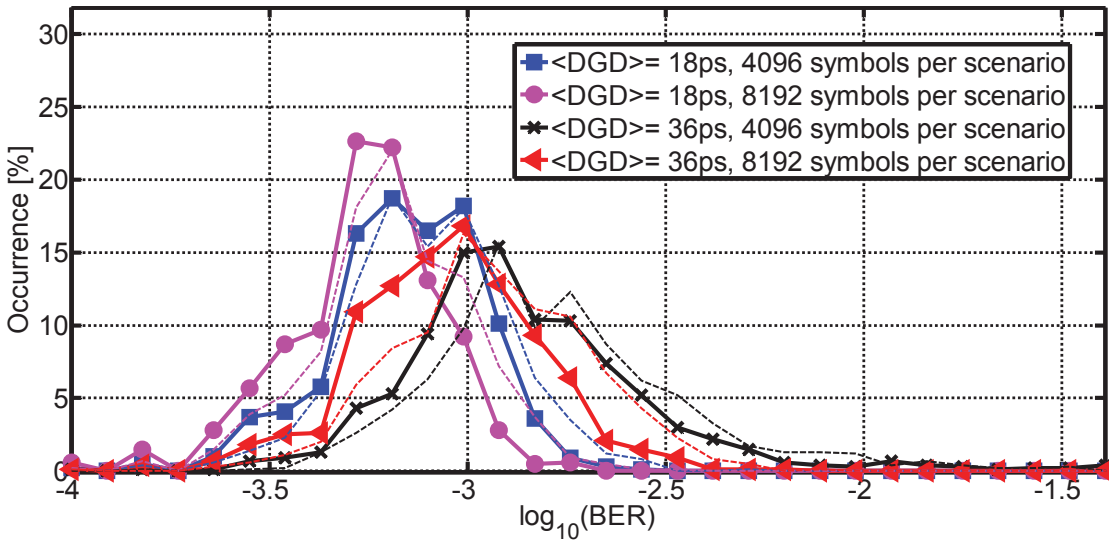

Figure 5.27: PU-DD-LMS (Pattern 2) based MIMO equalizer's BER performance for <DGD>= 18 ps and <DGD>= 36 ps. Histograms are computed based on 1000 PMD scenarios changing every 4096 and 8192 symbols. For comparison, dashed lines depict the corresponding results with PU-DD-LMS (Pattern 1).

5.7 Discussion on Computational Effort and Performance

The computational complexity of MIMO equalizers presented in sections 5.2 to 5.6 depends on 2x2 FIR filtering and the update process of the impulse responses. The four FIR filters require

$$C_M = 4{N_T}^2 \tag{5.40}$$

complex multiplications and

$$C_A = 4N_T(N_T - 1) \tag{5.41}$$

complex additions to equalize data block of length N_T . The computational complexity due to FIR filtering remains the same for all MIMO equalizers presented in sections 5.2 to 5.6. However, the overall computational complexity of these MIMO equalizers will vary due to different complexity in the update process of the impulse responses. A single update of the impulse responses (5.13) to (5.16) requires

$$C_M = 4(N_T + 1) \tag{5.42}$$

complex multiplications and

$$C_A = 4N_T \tag{5.43}$$

complex additions in standard CMA based MIMO equalizer. The CMA-QAM based MIMO equalizer also requires the same number of complex multiplications, complex additions and three additional real additions to compute power differences of the three rings for 16-QAM. However, in case of PU-CMA-QAM, a single update of the impulse responses requires

$$C_M = \frac{4(N_T+1)}{P} \tag{5.44}$$

complex multiplications and

$$C_A = \frac{4N_T}{P} \tag{5.45}$$

complex additions. So, the computational complexity of the update process is reduced by a factor of P. As an example at $N_T = 15$, 900 complex multiplications and 840 complex additions would be needed for FIR filtering in MIMO equalizers presented in sections 5.2 to 5.6. Furthermore, a single update of the impulse responses (5.13) to (5.16) would require 64 complex multiplications and 60 complex additions in CMA-QAM based MIMO equalizer. However, in case of a PU-CMA-QAM based MIMO equalizer with $P = 3$, a single update of the impulse responses would require approximately 22 complex multiplications and 20 complex additions in CMA-QAM based MIMO equalizer.

A single update of the impulse responses (5.34) to (5.37) requires

$$C_M = 4N_T \tag{5.46}$$

complex multiplications and

$$C_A = 4(N_T + 1) \tag{5.47}$$

complex additions in DD-LMS based MIMO equalizer. In case of PU-DD-LMS, a single update of the impulse responses requires

$$C_M = \frac{4N_T}{P} \tag{5.48}$$

complex multiplications and

$$C_A = \frac{4(N_T + 1)}{P} \tag{5.49}$$

complex additions. As an example at $N_T = 15$, a single update of the impulse responses (5.34)-(5.37) would require 60 complex multiplications and 64 complex additions in DD-LMS based MIMO equalizer. However, in case of a PU-DD-LMS based MIMO equalizer with $P = 3$, a single update of the impulse responses would require approximately 20 complex multiplications and 22 complex additions in CMA-QAM based MIMO equalizer.

As observed here, the computational complexity of the CMA-QAM and DD-LMS based MIMO equalizers is similar. But, the DD-LMS based MIMO equalizer has a clear advantage in terms of convergence performance. In this perspective, PU-DD-LMS (Pattern 2) based MIMO equalizer would be the most feasible option in terms of both performance and low computational complexity.

Chapter 6

Summary and Future Prospects

This last chapter concludes this dissertation with some final comments. A precise summary of the work done in this thesis is given in section 6.1. Furthermore, some future prospects based on this work are discussed in section 6.2.

6.1 Summary

The equalization techniques of two main sources of ISI in fiberoptic systems, i.e. CD and PMD, have been investigated, developed and optimized in this doctoral dissertation. Computationally-efficient CD and PMD equalization techniques have been proposed based on the obtained simulation results and performance analysis of 112 Gb/s PDM-QPSK and 224 Gb/s PDM-16-QAM systems.

In this work, FDEs have been analyzed and proposed as the most efficient solution for CD compensation in long-haul fiber links with a large amount CD. In this respect, performance analysis shows that a 1024-point FFT based FDE can easily compensate up to 48000 ps/nm of fiber CD (i.e. 3000 km fiber link). Besides, FDE performance at reduced ADC oversampling rates has also been analyzed. ADC oversampling rates as low as 1.25 samples per symbol can be employed, with small OSNR penalty.

A two-step FD blind CD estimation algorithm is presented that enables CD estimation at lower complexity than in the state-of-the-art approaches. It enables precise CD estimation with very high resolution even at lower computational complexity. The FD CD estimator can efficiently adapt to any CD search resolution, as low as 40 ps/nm is possible. Furthermore, it is shows robust performance in the presence of high DGD values. It shows a marginal CD estimation error of approximately ±50 ps/nm. This

error is negligible because a second stage MIMO equalizer can easily compensate this residual CD.

Moreover, MIMO equalization techniques have been investigated and optimized for polarization demultiplexing, PMD and residual CD compensation. The partial update based MIMO equalizers are proposed to reduce computational complexity. In this regard, the computational complexity of the update process is reduced by a factor of P. DD-LMS based MIMO equalizer performs better than the CMA-QAM based MIMO equalizer. In this respect, PU-DD-LMS (Pattern 2) based MIMO equalizer is the most feasible option in terms of both performance and low computational complexity.

Furthermore, the joint interoperability of different DSP based subsystems, i.e. CD equalizers, MIMO equalizers and the laser phase noise tolerant feedforward carrier recovery schemes, has been investigated and verified.

6.2 Future Prospects

- Blind adaptive CD and PMD equalizers consume massive computational resources. The proposed work in this dissertation enables high performance and computationally efficient CD and MIMO equalization.
- The proposed equalization schemes are based on blind adaptation according to the requirements of modern dynamic channel switching concept.
- The reduction in computational complexity enables the proposed equalizers to be implementable on FPGAs or ASICs in an efficient manner. Therefore, this would enable consumption of less number of their available hardware resources e.g. in terms of multiplications, additions or look-up tables. So, importantly the energy consumption would also be reduced.
- Both, CD and MIMO equalization techniques, have been simulated for QPSK and 16-QAM signals. They are even applicable to higher order m-QAM modulation schemes.
- The possibility of employing reduced oversampling rates decreases the requirement of high-speed ADCs.

- Use of state-of-the-art FEC schemes will further enable robust and error-free transmission.
- Presented DSP based subsystems have been simulated to achieve 112 Gb/s and 224 Gb/s for QPSK and 16QAM modulation formats, respectively. Furthermore, these DSP based subsystems are scalable to higher bit rates in the Tb/s range.

Bibliography

[1] D. Williams, K. C. Kao, “Pulse communication along glass fibers,” Proceedings of the IEEE, vol. 56, no. 2, pp. 197-198, 1968.

[2] K. C. Kao and G. A Hockham, “Dielectric-fibre surface waveguides for optical frequencies,” IEE Proceedings J Optoelectronics, vol. 133, no. 3, pp. 191-198, 1986.

[3] T. Imai, Y. Hayashi, N. Ohkawa, T. Sugie, Y. Ichihashi and T. Ito, “Field Demonstration of 2.5 Gbit/s Coherent Optical Transmission Through Installed Submarine Fiber Cables,” Electronics Letters, vol. 26, no. 17, pp. 1407-1409, 1990.

[4] R. J. Mears, L. Reekie, I. M. Jauncey and D. N. Payne, “Low-noise erbium doped fibre amplifier operating at 1.54μm,” Electronics Letters, vol. 23, no. 19, pp. 1026-1028, 1987.

[5] M. Taylor, “Coherent detection method using DSP to demodulate signal and for subsequent equalisation of propagation impairments,” Proc. ECOC’03, paper We4.P.111, September 21-25, 2003.

[6] R. Noé, “Phase noise tolerant synchronous QPSK receiver concept with digital I&Q baseband processing,” Proc. OECC/COIN’04, paper 16C2-5, July 12-16, 2004.

[7] R. Noé, “PLL-free synchronous QPSK polarization multiplex/diversity receiver concept with digital I&Q baseband processing,” IEEE Photonics Technology Letters, vol. 17, no. 4, pp. 887-889, 2005.

[8] E. Ip, A. P. Lau, D. J. Barros and J. M. Kahn, “Coherent detection in optical fiber systems,” Optics Express, vol. 16, issue 2, pp. 753-791, 2008.

[9] E. Ip and J.M. Kahn, "Digital Equalization of Chromatic Dispersion and Polarization Mode Dispersion," Journal of Lightwave Technology, vol.25, no.8, pp.2033-2043, 2007.

[10] M. F. Panhwar, "Electronic Mitigation of Transmission Impairments in Optical Communications Using Full-Field Detection," Master Thesis, Christian-Albrechts-Universität zu Kiel, Germany, 2010.

[11] Five Year Traffic Statistics at DE-CIX Frankfurt, 2014, https://www.de-cix.net/about/statistics/ [Online].

[12] Cisco Visual Networking Index: Global Mobile Data Traffic Forecast Update (2013–2018) Overview, available on February 05, 2014, http://www.cisco.com/c/en/us/solutions/collateral/service-provider/visual-networking-index-vni/white_paper_c11-520862.html [Online].

[13] H. Louchet, K. Kuzmin, and A. Richter, "Improved DSP algorithms for coherent 16-QAM transmission," Proc. ECOC'08, September 21-25, 2008.

[14] M. Nakazawa, K. Kikuchi, T. Miyazaki, "High Spectral Density Optical Communication Technologies," Springer, 2010.

[15] R. Noé, M. F. Panhwar, C. Wördehoff and D. Sandel, "Realtime Digital Signal Processing in Coherent Optical PDM-QPSK and PDM-16-QAM Transmission," Proc. EUSIPCO'2014, September 1-5, 2014.

[16] N. Kikuchi, K. Sekine, S. Sasaki, "Multilevel Signalling for High-Speed Optical Transmission," Proc. ECOC 2006, September 24-28, 2006.

[17] R. Dischler, "Experimental study of 16-, 32- and 64-QAM constellation sets in the 200-Gb/s regime on a data rate flexible system," Proc. OFC'2013, paper OTh3B2, March 17-21, 2013.

[18] Ciena Wavelogic 3, application note available on Oct. 11, 2013 at http://www.ciena.com/resources/application-notes/Enabling-a-Bigger-and-Smarter-Network-with-Cienas-WaveLogic-3-AN.html [online].

[19] R. Noé, "Essentials of Modern Optical Fiber Communication," Springer, 2010.

[20] C.R.S. Fludger, T. Duthel, D. Van den Borne, C. Schulien, E.-D. Schmidt, T. Wuth, J. Geyer, E. de Man, G.-D. Khoe and H. De Waardt, "Coherent Equalization and POLMUX-RZ-DQPSK for Robust 100-GE Transmission," Journal of Lightwave Technology, vol. 26, no. 1, pp. 64-72, 2008.

[21] N. Tran, C. Okonkwo, E. Tangdiongga, H. Jung and T. Koonen, "Cyclic-linked flexibility: An architectural approach for reconfigurable optical WDM-TDM access networks," IEEE/OSA Journal of Optical Communications and Networking, vol.5, no.6, pp. 574-583, 2013.

[22] J. Armstrong, "OFDM for Optical Communications," Journal of Lightwave Technology, vol.27, no.3, pp. 189-204, 2009.

[23] S. Randel, P. J. Winzer, M. Montoliu and R. Ryf, "Complexity analysis of adaptive frequency-domain equalization for MIMO-SDM transmission," Proc. ECOC'13, September 22-26, 2013.

[24] B. S. G. Pillai, B. Sedighi, K. Guan, N. P. Anthapadmanabhan, W. Shieh, K. J. Hinton and R. S. Tucker, "End-to-End Energy Modeling and Analysis of Long-Haul Coherent Transmission Systems," Journal of Lightwave Technology, vol. 32, no. 18, pp. 3093-3111, 2014.

[25] Abschlussbericht, 16QAM-DPT, DFG-Förderprojekt RU 447/13-1, August 2013.

[26] J. Viterbi and A. M. Viterbi, "Nonlinear Estimation of PSK-Modulated Carrier Phase with Application to Burst Digital Transmission," IEEE Transactions on Information Theory, vol. IT-29, no. 4, pp. 543-551, 1983.

[27] T. Xu; G. Jacobsen, S. Popov, J. Li, S. Sergeyev and Y. Zhang, "Analysis of carrier phase extraction methods in 112-Gbit/s NRZ-PDM-QPSK coherent transmission system," Communications and Photonics Conference (ACP) Asia, November 7-10, 2012.

[28] M. Seimetz, "Laser Linewidth Limitations for Optical Systems with High-Order Modulation Employing Feed Forward Digital Carrier Phase Estimation,"

Proc. Optical Fiber communication/National Fiber Optic Engineers Conference (OFC/NFOEC), February 24-28, 2008.

[29] T. Pfau, S. Hoffmann and R. Noé, "Hardware-Efficient Coherent Digital Receiver Concept With Feedforward Carrier Recovery for M-QAM Constellations," Journal of Lightwave Technology, vol. 27, no. 8, pp. 989-999, 2009.

[30] I. Fatadin, D. Ives and S. J. Savory, "Blind Equalization and Carrier Phase Recovery in a 16-QAM Optical Coherent System," Journal of Lightwave Technology, vol.27, no.15, pp.3042-3049, 2009.

[31] I. Fatadin, D. Ives and S.J. Savory, "Laser Linewidth Tolerance for 16-QAM Coherent Optical Systems using QPSK Partitioning," IEEE Photonics Technology Letters, vol. 22, no. 9, pp. 631-633, 2010.

[32] M. R. Wilder, "Understanding and measuring chromatic dispersion," Fiber optics [online], 2000.

[33] M. C. Jeruchim, P. Balaban, K. S. Shanmugan, "Simulation of Communication Systems: Modeling, Methodology, and Techniques," Springer, 2nd Edition, 2000.

[34] G. P. Agrawal, "Fiber-Optic Communication Systems," 3rd Edition, John Wiley & Sons, Inc., 2002.

[35] G. P. Agrawal, "Nonlinear Fiber Optics," 3rd Edition, Academic Press, 2001.

[36] R. Ramaswami & K. N. Sivarajan, "Optical Networks: A Practical Perspective," Morgan Kaufmann Publishers, Inc., 1998.

[37] A. Deragon and J. Ferry, "Measuring and Compensating for PMD in High-Speed Optical Networks," NetTest Technical Paper, 2002.

[38] VPItransmissionMaker™ Optical Systems, http://www.vpiphotonics.com/ [Online].

[39] MATLAB™ documentation, http://www.mathworks.com/ [online].

[40] Python™ documentation, http://www.python.org/ [online].

[41] M. Devetsikiotis and J. K. Townsend, “A useful and general technique for improving the efficiency of Monte Carlo simulation of digital communication systems,” Proc. GLOBECOM’1990, vol. 2, pp.1215-1221 vol. 2, 1990.

[42] K. Ben Letaief and D. A. Lee, “A quick Monte Carlo technique for simulating direct-detection optical CDMA communications systems,” Communications, Proc. ICC’1993, vol.1, pp.161-165, 1993.

[43] E. Choi, J. Lee, H. Jang, J. Jeong, H. Lee, Y. J. Oh and S. Hwang, “Modeling and verification of FEC performance for optical transmission systems using a proposed uniformly quantized symbol error probability model,” OFC/NFOEC’2003, paper MF76, March 23-28, 2003.

[44] A. Bononi, P Serena, J.-C. Antona and S. Bigo, “Implications of nonlinear interaction of signal and noise in low-OSNR transmission systems with FEC,” OFC/NFOEC’2005, paper OThW5, March 6-11, 2005.

[45] Y. Miyata, K. Kubo, K. Onohara, W. Matsumoto, H. Yoshida and T. Mizuochi, “UEP-BCH product code based hard-decision FEC for 100 Gb/s optical transport networks,” OFC/NFOEC’2012, paper JW2A.7, March 4-8, 2012.

[46] G. E. Kohnke, S.J. Spammer, M. Mlejnek, B. Agogliati, D. Caironi, L. Arcangeli, M. Belmonte, F. Garcia, and A.D. Ellis, “Fiber Bragg grating for dispersion compensation,” Proc. Optical Fiber Communication Conference (OFC), March 17-22, 2002.

[47] M. Wandel, P. Kristensen, T. Veng, Y. Qian, Q. Le, L. Gruner-Nielsen, “Dispersion compensating fibers for non-zero dispersion fibers,” Proc. Optical Fiber Communication Conference (OFC), March 17-22, 2002.

[48] S. J. Savory, G. Gavioli, R. I. Killey, and P. Bayvel, “Electronic compensation of chromatic dispersion using a digital coherent receiver,” Optics Express, vol. 15, issue 5, pp. 2120-2126, 2007.

[49] S. J. Savory, “Digital filters for coherent optical receivers,” Optics Express, vol. 16, issue 2, pp. 804-817, 2008.

[50] B. Spinnler, F. N. Hauske and M. Kuschnerov, “Adaptive Equalizer Complexity in Coherent Optical Receivers,” Proc. ECOC’08, paper We.2.E.4, September 21-25, 2008.

[51] J. Leibrich and W. Rosenkranz, “Frequency Domain Equalization with Minimum Complexity in Coherent Optical Transmission Systems,” Proc. OFC/NFOEC’10, paper OWV1, March 21-25, 2010.

[52] B. Spinnler, "Equalizer Design and Complexity for Digital Coherent Receivers, “IEEE Journal of Selected Topics in Quantum Electronics,” vol.16, no.5, pp.1180-1192, 2010.

[53] K. Ishihara, T. Kobayashi, R. Kudo, Y. Takatori, A. Sano, E. Yamada, H. Masuda and Y. Miyamoto, “Frequency-domain equalisation for optical transmission systems,” Electronics Letters, vol.44, no.14, pp.870,871, 2008.

[54] T. Xu, G. Jacobsen, S. Popov, J. Li, E. Vanin, K. Wang, A. T. Friberg and Y. Zhang, “Chromatic dispersion compensation in coherent transmission system using digital filters,” Optics Express, vol. 18, issue 15, pp. 16243-16257, 2010.

[55] R. Kudo, T. Kobayashi, K. Ishihara, Y. Takatori, A. Sano and Y. Miyamoto, “Coherent Optical Single Carrier Transmission Using Overlap Frequency Domain Equalization for Long-Haul Optical Systems,” Journal of Lightwave Technology, vol.27, no.16, pp.3721-3728, 2009.

[56] K. Ishihara, T. Kobayashi, R. Kudo, Y. Takatori, A. Sano, E. Yamada, H. Masuda, M. Matsui, M. Mizoguchi and Y. Miyamoto, “Frequency-domain equalisation without guard interval for optical transmission systems,” Electronics Letters , vol. 44, no. 25, pp. 1480-1482, 2008.

[57] T. Xu, G. Jacobsen, S. Popov, M. Forzati, J. Mårtensson, M. Mussolin, J. Li, K. Wang, Y. Zhang and A. T. Friberg, “Frequency-domain Chromatic Dispersion Equalization using Overlap-add Methods in Coherent Optical System,” Journal of Optical Communications, vol. 32, issue 2, pp. 131-135, 2011.

[58] J. Geyer, C. R. S. Fludger, T. Duthel, C. Schulien and B. Schmauss, "Efficient frequency domain chromatic dispersion compensation in a coherent Polmux QPSK-receiver," Proc. OFC/NFOEC'10, March 21-25, 2010.

[59] J. Geyer, A. Bisplinghoff, T. Duthel, C. Fludger, C. Schulien and B. Schmauss, "Optimization of the Chromatic Dispersion Equalizer of a 43Gb/s Realtime Coherent Receiver," Proc. OFC/NFOEC'10, paper OWV8, March 21-25, 2010.

[60] G. Goldfarb and G. Li, "Chromatic Dispersion Compensation Using Digital IIR Filtering With Coherent Detection," IEEE Photonics Technology Letters, IEEE , vol. 19, no. 13, pp. 969,971, 2007.

[61] R. Noé, U. Rückert, S. Hoffmann, T. Pfau and R. Peveling, "Realization of digital coherent receivers," Proc. IEEE/LEOS Annual Meeting Conference'2009, pp. 422-423, Oct. 4-8 2009.

[62] T. Xu, "DSP based Chromatic Dispersion Equalization and Carrier Phase Estimation in High Speed Coherent Optical Transmission Systems," Doctoral Dissertation, KTH Stockholm, 2012.

[63] J. G. Proakis and D. G. Manolakis, Digital Signal Processing: Principles, Algorithms and Applications, 3rd Edition, Prentice-Hall International, Inc., 1996.

[64] Glenn Zelniker and Fred J. Taylor, "Advanced Digital Signal Processing: Theory and Applications," CRC Press, 1993.

[65] J. R. Vandekieft, "Computational Improvements to Linear Convolution with Multirate Filtering Methods," Master Thesis, University of Miami, USA, 1998.

[66] R.J. Marks II, "Introduction to Shannon Sampling and Interpolation Theory," Spinger-Verlag, 1991.

[67] J. H. Winters, "Equalization in Coherent Lightwave Systems Using a Fractionally Spaced Equalizer," Journal of Lightwave Technology, vol.8, no.10, pp.1487-1491, 1990.

[68] T. Duthel, C. R. S Fludger, D. van den Borne, C. Schulien, E.-D. Schmidt, T. Wuth, E. de Man, G. D. Khoe and H. de Waardt, "Impairment tolerance of 111Gbit/s POLMUX-RZ-DQPSK using a reduced complexity coherent receiver with a T-spaced equaliser," Proc. ECOC'07, September 16-20, 2007.

[69] A. Carena, V. Curri, P. Poggiolini, G. Bosco and F. Forghieri, "Impact of ADC Sampling Speed and Resolution on Uncompensated Long-Haul 111-Gb/s WDM PM-QPSK Systems," IEEE Photonics Technology Letters, vol.21, no.20, pp.1514-1516, 2009.

[70] M. F. Panhwar, M. El-Darawy, K. Puntsri and R. Noé, "Reduced Sampling Rate Frequency Domain CD Equalization for 112 Gb/s PDM-QPSK," Proc. OECC 2012, Paper 5B4-4, July 2-6, 2012.

[71] M. F. Panhwar, M. El-Darawy, K. Puntsri and R. Noé, "ADC Sampling Rate Requirements for the Frequency-Domain CD Equalization," Workshop der ITG-Fachgruppe 5.3.1 2012, July 5-6, 2012.

[72] K. Ishihara, R. Kudo, T. Kobayashi, A. Sano, Y. Takatori, T. Nakagawa and Y. Miyamoto, "Frequency-domain equalization for coherent optical transmission systems," Proc. OFC/NFOEC'11, paper OWW4, March 6-10, 2011.

[73] M. S. Faruk and K. Kikuchi, "Frequency-domain adaptive equalization in digital coherent receivers," Conference on Lasers and Electro-Optics (CLEO), May 1-6, 2011.

[74] M. Kuschnerov, F.N. Hauske, K. Piyawanno, B. Spinnler, A. Napoli and B. Lankl, "Adaptive chromatic dispersion equalization for non-dispersion managed coherent systems," Proc. OFC/NFOEC'09, paper OMT1, March 22-26, 2009.

[75] M. Kuschnerov, F. N. Hauske, K. Piyawanno, B. Spinnler, M. S. Alfiad, A. Napoli and B. Lankl, "DSP for Coherent Single-Carrier Receivers," Journal of Lightwave Technology, vol.27, no.16, pp.3614-3622, 2009.

[76] F. N. Hauske, M. Kuschnerov, B. Spinnler, B. Lankl, "Optical Performance Monitoring in Digital Coherent Receivers," Journal of Lightwave Technology, vol. 27, no. 16, pp.3623-3631, 2009.

[77] V. Ribeiro, S. Ranzini, J. Oliveira, V. Nascimento, E. Magalhães and E. Rosa, "Accurate Blind Chromatic Dispersion Estimation in Long-haul 112Gbit/s PM-QPSK WDM Coherent Systems," Proc. SPPCom'12, paper SpTh2B.3, June 19-21, 2012.

[78] F. N. Hauske, C. Xie, Z. Zhang, C. Li, L. Li and Q. Xiong, "Frequency domain chromatic dispersion estimation," Proc. OFC/NFOEC'10, paper JThA11, March 21-25, 2010.

[79] F. N. Hauske, Z. Zhang, C. Li, C. Xie, and Q. Xiong, "Precise, Robust and Least Complexity CD estimation," Proc. OFC/NFOEC'11, paper JWA32, March 6-10, 2011.

[80] R. A. Soriano, F. N. Hauske, N. Guerrero Gonzalez, Z. Zhang, Y. Ye and I. T. Monroy, "Chromatic Dispersion Estimation in Digital Coherent Receivers," Journal of Lightwave Technology, vol. 29, no. 11, pp. 1627-1637, 2011.

[81] D. Wang, C. Lu, A. P. T. Lau and S. He, "Adaptive Chromatic Dispersion Compensation for Coherent Communication Systems Using Delay-Tap Sampling Technique," IEEE Photonics Technology Letters, vol. 23, no. 14, pp. 1016-1018, 2011.

[82] Q. Sui, A. P. T. Lau, and C. Lu., "Fast and robust chromatic dispersion estimation using auto-correlation of signal power waveform for DSP based-coherent systems," Proc. OFC/NFOEC'12, paper OW4G, March 4-8, 2012.

[83] C. Malouin, P. Thomas, B. Zhang, J. O'Neil and T. Schmidt, "Natural Expression of the Best-Match Search Godard Clock-Tone Algorithm for Blind Chromatic Dispersion Estimation in Digital Coherent Receivers," Proc. SPPCom'12, paper SpTh2B.4, June 19-21, 2012.

[84] J. C. M. Diniz, S. M. Ranzini, V. B. Ribeiro, E. C. Magalhaes, E. S. Rosa, V. E. S. Parahyba, L. V. Franz, E. E. Ferreira and J. C. R. F. Oliveira, "Hardware-

Efficient Chromatic Dispersion Estimator based on Parallel Gardner Timing Error Detector," Proc. OFC/NFOEC'13 ,paper OTh3C March 17-21, 2013.

[85] M. F. Panhwar, C. Wördehoff, K. Puntsri, A. Al-Bermani, U. Rückert and R. Noé, "Adaptive Search Based Efficient Non-Data Aided FD CD Estimation for FDE," Proc. ITG-Fachtagung Photonische Netze 2013, May 6-7, 2013.

[86] M. F. Panhwar, C. Wördehoff, K. Puntsri, U. Rückert and R. Noé, "Reduced Oversampling Rate for Adaptive Search Based Blind FD CD Estimation," Proc. OECC 2013, paper ThR3-4, June 30-July 4, 2013.

[87] D. N. Godard, "Passband Timing Recovery in an All-Digital Modem Receiver," IEEE Transactions on Communications, vol. 26, no. 5, pp. 517-523, 1978.

[88] G. Foschini and C. Poole, "Statistical theory of polarization dispersion in single mode fibers," Journal of Lightwave Technology, vol. 9, no. 11, pp. 1439-1456, 1991.

[89] L. E. Nelson, H. Kogelnik and P. J. Winzer, "Polarization mode dispersion and its impact on high bit-rate, fiber-optic communication systems," Conference on Lasers and Electro-Optics (CLEO), May 16-21, 2004.

[90] B. W. Hakki, "Polarization mode dispersion compensation by phase diversity detection," IEEE Photonics Technology Letters, vol. 9, no. 1, pp. 121-123, 1997.

[91] H. Bulow, "Limitation of Optical First-Order PMD Compensation," Proc. OFC'99, paper WE1, February 21-26, 1999.

[92] H. Bulow, "Analysis of system outage induced by second order PMD in the presence of chromatic dispersion," Proc. ECOC'98, paper WdC5, September 20-24, 1998.

[93] F. Buchali and H. Bulow, "Adaptive PMD compensation by electrical and optical techniques," Journal of Lightwave Technology, vol.22, no.4, pp.1116-1126, 2004.

[94] J. Benesty and P. Duhamel, “Fast constant modulus adaptive algorithm,” IEE Proceedings on Radar and Signal Processing, vol. 138, no. 4, pp. 379-387, 1991.

[95] S. J. Savory, V. Mikhailov, R. I. Killey and P. Bayvel, “Digital Coherent Receivers for Uncompensated 42.8Gbit/s Transmission over High PMD Fibre,” Proc. ECOC’07, September 16-20, 2007.

[96] L. Liu; Z. Tao, W. Yan, S. Oda, T. Hoshida, and J. C. Rasmussen, “Initial tap setup of constant modulus algorithm for polarization de-multiplexing in optical coherent receivers,” Proc. OFC’09, March 22-26, 2009.

[97] N. Kaneda and A. Leven, “Coherent Polarization-Division-Multiplexed QPSK Receiver With Fractionally Spaced CMA for PMD Compensation,” IEEE Photonics Technology Letters, vol.21, no.4, pp.203-205, 2009.

[98] T. F. Portela, D. V. Souto, V. N. Rozental, H. B. Ferreira, D. A. A. Mello and H. Griesser, “Analysis of signal processing techniques for optical 112 Gb/s DP-QPSK receivers with experimental data,” Journal of Microwaves, Optoelectronics and Electromagnetic Applications, vol.10, no. 1, pp 155-164, 2011.

[99] W. Xue, X. Yang and Z. Zhang, “A variable step size blind equalization algorithm for QAM signals,” Proc. ICMMT’ 2010, pp. 1801-1804, May 8-11, 2010.

[100] S. Chen, “Low complexity concurrent constant modulus algorithm and soft decision directed scheme for blind equalisation,” IEE Proceedings on Vision, Image and Signal Processing, vol. 150, no. 5, pp. 312-320, 2003.

[101] K. Kikuchi, “Polarization-demultiplexing algorithm in the digital coherent receiver,” Proc. IEEE/LEOS Summer Topical Meetings’2008, pp. 101-102, July 21-23, 2008.

[102] D. N. Godard, “Self-Recovering Equalization and Carrier Tracking in Two-Dimensional Data Communication Systems,” IEEE Transactions on Communications, vol. 28, no. 11, pp. 1867-1875, 1980.

[103] J. Treichler and B. Agee, “A new approach to multipath correction of constant modulus signals,” IEEE Transactions on Acoustics, Speech and Signal Processing, vol. 31, no. 2, pp. 459-472, 1983.

[104] R. Noé, T. Pfau, M. El-Darawy and S. Hoffmann, “Electronic Polarization Control Algorithms for Coherent Optical Transmission,” IEEE Journal of Selected Topics in Quantum Electronics, vol. 16, no. 5, pp. 1193-1200, 2010.

[105] S. C. Douglas, “Analysis and implementation of the max-NLMS adaptive filter,” Proc. Twenty-Ninth Asilomar Conference on Signals, Systems and Computers’1995, vol.1, pp. 659-663, 1995.

[106] S. C. Douglas, “Adaptive filters employing partial updates,” IEEE Transactions on Circuits and Systems II: Analog and Digital Signal Processing, vol. 44, no. 3, pp. 209-216, 1997.

[107] M. F. Panhwar, D. Sandel, C. Wördehoff and R. Noé, “PU-CMA-QAM based MIMO Equalization for Digital PMD Compensation in PDM-16-QAM Receivers,” Proc. ITG-Fachtagung Photonische Netze’2014, May 5-6, 2014.

[108] M. F. Panhwar, D. Sandel, C. Wördehoff, K. Puntsri, S. Hussin and R. Noé, “PU-CMA-QAM based MIMO Equalization in the DSP Enabled PDM-16-QAM Receivers,” Proc. OECC-ACOFT 2014, 6-10 July 2014, Melbourne, Australia.

[109] B. Widrow, J. McCool, and M. Ball, “The complex LMS algorithm,” Proc. of the IEEE, vol. 63, no. 4, pp. 719-720, 1975.

[110] L. R. Litwin Jr., M. D. Zoltowski, T. J. Endres and S. N. Hulyalkar, “Blended CMA: smooth, adaptive transfer from CMA to DD-LMS,” Proc. IEEE WCNC’1999, vol. 2, pp.797-800, 1999.

[111] Y. Mori, and K. Kikuchi, “Carrier-phase-insensitive operation of FIR Alters adapted by the decision-directed LMS algorithm in digital coherent optical receivers,” Proc. OECC’2011, July 4-8, 2011.

[112] L. Tao, Y. Wang, Y. Gao, A. P. T. Lau, N. Chi and C. Lu, "40 Gb/s CAP32 System With DD-LMS Equalizer for Short Reach Optical Transmissions," IEEE Photonics Technology Letters, vol. 25, no. 23, pp. 2346-2349, 2013.

[113] D. L. Jones, S. Appadwedula, M. Berry, M. Haun, D. Moussa and D. Sachs, "Adaptive filtering: LMS algorithm," The Connexions Project Version 2.14, http://creativecommons.org/licenses/by/1.0, 2009.

Appendix A: List of Notations and Abbreviations

List of Notations

$\otimes$	Convolution operation
*	Complex conjugate operation
$\alpha(\omega)$	Fiber loss (attenuation)
$\beta(\omega)$	Mode-propagation constant
β_0	Phase delay per unit length
β_1	Group delay per unit length
β_2	Group velocity dispersion
$\Delta\beta_1$	Difference between the propagation constants the two orthogonal axes
B	Symbol rate
$\langle BER \rangle$	Expected BER for the simulation model
c	Velocity of light
CD_{FFT}	Initial FFT mapping based CD estimate
CD_{CT}	Optimized and precise estimated CD value
CD_l	Applied compensator CD

D	Chromatic dispersion parameter
D_p	Polarization mode dispersion parameter
D_X	MIMO equalizer error in the X polarization
D_Y	MIMO equalizer error in the Y polarization
$e_X(k)$	Received signal in X polarization
$e_Y(k)$	Received signal in Y polarization
$e_{Xi}(k)$	Input signal to MIMO equalizer in X polarization
$e_{Yi}(k)$	Input signal to MIMO equalizer in Y polarization
$e_{Xo}(k)$	Output signal of the MIMO equalizer in X polarization
$e_{Yo}(k)$	Output signal of the MIMO equalizer in Y polarization
$\hat{e}_{Xo}(k)$	Output signal after carrier and data recovery in X polarization
$\hat{e}_{Yo}(k)$	Output signal after carrier and data recovery in Y polarization
$e_{F,X}(k)$	Equalized signal in X polarization
$e_{F,Y}(k)$	Equalized signal in Y polarization
$E_F[n]$	Equalized discrete-frequency signal
$E_X[n]$	Received discrete-frequency signal in X polarization
$E_Y[n]$	Received discrete-frequency signal in Y polarization
$\Delta f T_S$	Laser sum-linewidth-times-symbol-duration product
$h(k)$	Discrete time impulse response

$H(\omega)$	Fiber transfer function
$H'(\omega)$	Inverse fiber transfer function
$H'[n]$	Inverse discrete fiber transfer function
J_{CMA}	Constant modulus algorithm cost function
$J_{CMA-QAM}$	Constant modulus algorithm cost function for QAM
J_{CT}	Clock-tone based cost function
J_{DD-LMS}	Decision directed least mean square cost function
J_{FFT}	FFT mapping based cost function
k	Discrete time index
SS_p	Subset indices in PU algorithm
K	Carrier phase estimator filter length.
λ	Carrier wavelength
l_c	Correlation length
L	Length of the fiber
μ_g	MIMO equalizer update gain
n	Discrete-frequency index
N	FFT length
N'	Index of the clock-tone component
N_b	Number of bits used in the simulation

N_e	Number of bit errors in the recovered data
N_T	MIMO equalizer length
N_P	Partial update length
P	Number of subsets or parts of the impulse response
P_j	Power levels of the QAM signal
R_S	ADC sampling frequency
σ_T	Mean differential group delay
Δs	Stepsize of the CD scan range
ΔT	Instantaneous time difference between the fast and slow axes
T_S	Symbol duration
ω_0	Center frequency

List of Abbreviations

ADC	Analog-to-digital convertor
ASIC	Application-specific integrated circuit
BER	Bit error rate
CD	Chromatic dispersion
CIX-DE	German Commercial Internet Exchange
CMA	Constant modulus algorithm
CT	Clock-tone
DCF	Dispersion compensating fiber
DFT	Discrete Fourier transform
DGD	Differential group delay
DD	Decision directed
DSP	Digital signal processing
DSPU	Digital signal processing unit
EDFA	Erbium doped fiber amplifier
FBG	Fiber Bragg grating
FD	Frequency domain
FDE	Frequency domain equalization
FEC	Forward error correction
FFT	Fast Fourier transform
FIR	Finite impulse response

FPGA	Field-programmable gate array
FSE	Fractionally spaced equalizer
GI	Guard interval
GVD	Group velocity dispersion
I	Inphase
IBI	Inter block interference
IFFT	Inverse fast Fourier transform
IIR	Infinite impulse response
ISI	Inter-symbol interference
LMS	Least mean square
LO	Local oscillator
LPF	Low-pass filter
MAN	Metropolitan area network
MATLAB	Matrix laboratory
MIMO	Multiple-input multiple-output
NRZ	Non-return-to-zero
NT	Normalized threshold
OBPF	Optical bandpass filter
OFDM	Orthogonal frequency division multiplexing
OSNR	Optical signal-to-noise ratio
PBC	Polarization beam combiner
PBS	Polarization beam splitter
PD	Photo-detector
PDF	Probability density function

PDM	Polarization-division multiplex
PMD	Polarization mode dispersion
PRBS	Pseudo-random binary sequence
PSD	Power spectral density
PU	Partial update
Q	Quadrature
QAM	Quadrature amplitude modulation
QPSK	Quadrature phase shift keying
QPSKP	Quadrature phase shift keying partitioning
RMS	Root mean square
RTO	Real-time sampling oscilloscope
RX	Receiver
RZ	Return-to-zero
SDM	Space division multiplexing
SSMF	Standard single-mode optical fiber
TD	Time domain
TX	Transmitter
V&V	Viterbi and Viterbi
WDM	Wavelength division multiplexing

Appendix B: List of Figures

Appendix C: List of Publications

- R. Noé, **M. F. Panhwar**, C. Wördehoff and D. Sandel, "Realtime Digital Signal Processing in Coherent Optical PDM-QPSK and PDM-16-QAM Transmission," Proc. EUSIPCO 2014 (Invited Paper), 1.-5. September 2014, Lisbon, Portugal.

- S. Hussin, R. Noé and **M. F. Panhwar**, "Improvement of RF-Pilot Phase Noise Compensation for CO-OFDM Transmission Systems via Common Phase Error Equalizer," Proc. OECC-ACOFT 2014, Paper WEPS2-53, 6.-10. July 2014, Melbourne, Australia.

- **M. F. Panhwar**, D. Sandel, C. Wördehoff, K. Puntsri, S. Hussin, R. Noé, "PU-CMA-QAM based MIMO Equalization in the DSP Enabled PDM-16-QAM Receivers," Proc. OECC-ACOFT 2014, Paper TH11B-3, 6.-10. July 2014, Melbourne, Australia.

- B. Koch, R. Noé, V. Mirvoda, D. Sandel and **M. F. Panhwar**, "Simple Polarization-Dependent Loss Measurement Based on Polarization Scrambling," Proc. OECC-ACOFT 2014, Paper TU3D-3, 6.-10. July 2014, Melbourne, Australia.

- B. Koch, R. Noé, V. Mirvoda, D. Sandel **and M. F. Panhwar**, "40 dB Crosstalk Suppression in High-Precision Endless Polarization Control," Proc. OECC-ACOFT 2014, Paper WE8D-5, 6.-10. July 2014, Melbourne, Australia.

- S. Hussin, R. Noé and **M. F. Panhwar**, "Fiber Nonlinearity Tolerance of Partial Pilot Filling in CO-OFDM Transmission Systems," Proc. OECC-ACOFT 2014, Paper WEPS2-52, 6.-10. July 2014, Melbourne, Australia.

- B. Koch, R. Noé, V. Mirvoda, D. Sandel and **M. F. Panhwar**, "APD-Based Interference Detectors Yield 7-dB Dynamic Range of 70-krad/s PDM-DPSK

Endless Polarization Demultiplexer," Proc. OECC-ACOFT 2014, Paper WE8D-4, 6.-10. July 2014, Melbourne, Australia.

- **M. F. Panhwar**, D. Sandel, C. Wördehoff, S. Hussin and R. Noé, "PU-CMA-QAM based MIMO Equalization for Digital PMD Compensation in PDM-16-QAM Receivers," Proc. ITG-Fachtagung Photonische Netze 2014, 5.-6. May 2014, Leipzig, Germany.

- S. Hussin, K. Puntsri, **M. F. Panhwar** and R. Noé, "Partial Pilot Filling for Phase Noise Compensation in Coherent Optical OFDM Systems," Proc. OECC 2013, Paper TuPR-17, 30. June-4. July 2013, Kyoto, Japan.

- **M. F. Panhwar**, C. Wördehoff, K. Puntsri, U. Rückert and R. Noé, "Reduced Oversampling Rate for Adaptive Search Based Blind FD CD Estimation," Proc. OECC 2013, Paper ThR3-4, 30. June-4. July 2013, Kyoto, Japan.

- S. Hussin, K. Puntsri, D. Sandel, **M. F. Panhwar** and R. Noé, "Efficiency Enhancement of CO-OFDM Systems Using Different Pulse Shapes," Proc. OECC 2013, Paper TuR4-4, 30. June-4. July 2013, Kyoto, Japan.

- K. Puntsri , O. Jan, A. Al-Bermani, D. Sandel, C. Wördehoff, S. Hussin, **M. F. Panhwar**, U. Rückert and R. Noé, "Pilot-aided CD and PN Compensation Simultaneously in CO-OFDM Systems," Proc. OECC 2013, Paper TuR4-7, 30. June-4. July 2013, Kyoto, Japan.

- K. Puntsri, O. Jan, A. Al-Bermani, C. Wördehoff, D. Sandel, **M. F. Panhwar**, S. Hussin and R. Noé, U. Rückert, "ISI Tolerance of Cyclic Prefix Free Coherent Optical OFDM Communication System," Proc. ITG-Fachtagung Photonische Netze 2013, 6.-7. May 2013, Leipzig, Germany.

- **M. F. Panhwar**, C. Wördehoff, K. Puntsri, A. Al-Bermani, U. Rückert and R. Noé, "Adaptive Search Based Efficient Non-Data Aided FD CD Estimation for FDE," Proc. ITG-Fachtagung Photonische Netze 2013, 6.-7. May 2013, Leipzig, Germany.

- A. Al-Bermani, C. Wördehoff , O. Jan, K. Puntsri, **M. F. Panhwar**, U. Rückert and R. Noé, "The Influence of Laser Phase noise on Carrier Phase Estimation of a Real-Time 16-QAM Transmission with FPGA Based Coherent Receiver," Proc. ITG-Fachtagung Photonische Netze 2013, 6.-7. May 2013, Leipzig, Germany.

- K. Puntsri, O. Jan, A. Al-Bermani, C. Wördehoff, D. Sandel, S. Hussin, **M. F. Panhwar**, R. Noé and U. Rückert, "An Ultralow Complexity Algorithm for Frame Synchronization and IQ Alignment in CO-OFDM Systems," OFC/NFOEC 2013, Paper JTh2A.43, March 17-21, 2013, Anaheim, USA.

- K. Puntsri, V. Mirvoda, S. Hussin, O. Jan, A. Al-Bermani, **M. F. Panhwar** and R. Noé, "A Low Complexity and High Accuracy Frame Synchronization for Optical OFDM and PolMux-Optical OFDM," IEEE IPC 2012, 23.-27. Sept. 2012, San Francisco, California, USA.

- K. Puntrsri, V. Mirvoda, S. Hussin, O. Jan, Al-Bermani, **M. F. Panhwar** and R. Noé, "A Low Complexity and High Accuracy Frame Synchronization for PolMux-Optical OFDM," Workshop der ITG-Fachgruppe 5.3.1 2012, 5.-6. July 2012, Nürnberg, Germany.

- **M. F. Panhwar**, M. El-Darawy, K. Puntsri and R. Noé, "ADC Sampling Rate Requirements for the Frequency-Domain CD Equalization," Workshop der ITG-Fachgruppe 5.3.1 2012, 5.-6. July 2012, Nürnberg, Germany.

- K. Puntrsri, D. Sandel, S. Hussin, O. Jan, A. Al-Bermani, **M. F. Panhwar** and R. Noé, "A Novel Method for IQ Imbalance Compensation in CO-OFDM Systems," Proc. OECC 2012, Paper 4B3-1, 2.-6. July 2012, Busan, South Korea.

- **M. F. Panhwar**, M. El-Darawy, K. Puntsri and R. Noé, "Reduced Sampling Rate Frequency Domain CD Equalization for 112 Gb/s PDM-QPSK," Proc. OECC 2012, Paper 5B4-4, 2.-6. July 2012, Busan, South Korea.